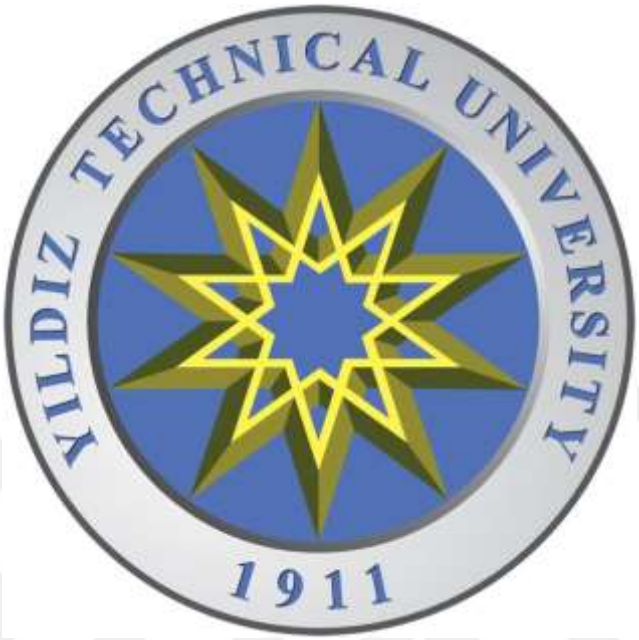


GRADUATE SCHOOL OF NATURAL AND APPLIED SCIENCES

THESIS TEMPLATE

NOVEMBER, 2016

REPUBLIC OF TURKEY
YILDIZ TECHNICAL UNIVERSITY
GRADUATE SCHOOL OF NATURAL AND APPLIED SCIENCES

A STUDY OF THE RELATION OF PIEZOELECTRIC PROPERTIES AND NANO STRUCTURES THROUGH METHODS IN COMPUTATIONAL PHYSICS

BERNA AKGENÇ

Ph.D. THESIS
DEPARTMENT OF PHYSICS
PROGRAM OF PHYSICS

ADVISER
PROF. DR. ÇETİN TAŞSEVEN

İSTANBUL, 2016

REPUBLIC OF TURKEY

YILDIZ TECHNICAL UNIVERSITY

GRADUATE SCHOOL OF NATURAL AND APPLIED SCIENCES

A STUDY OF THE RELATION OF PIEZOELECTRIC PROPERTIES AND NANO STRUCTURES THROUGH METHODS IN COMPUTATIONAL PHYSICS

A thesis submitted by Berna AKGENÇ in partial fulfillment of the requirements for the degree of **DOCTORATE OF PHSILOSOPHY** is approved by the committee on 28.11.2016 in Department of Physics, Program of Physics.

Thesis Adviser

Prof. Dr. Çetin Taşseven

Yıldız Technical University

Co- Adviser

Prof. Dr. Tahır ÇAĞIN

Texas A&M University

Approved By the Examining Committee

Prof. Dr. Çetin TAŞSEVEN

Yıldız Technical University _____

Prof. Dr. İdris GÜMÜŞ

Maltepe University _____

Prof. Dr. Metin SUBAŞI

Yıldız Technical University _____

Prof. Dr. Murat ÖZER

Yıldız Technical University _____

Assoc. Prof. Dr. Şahin UYAVER

Turkish - German University _____

This study was supported by the International Institute of Materials for Energy Conversion (IIMEC) at Texas A&M University with NSF International Materials Institute (DMR 0844082), the Council of Higher Education of Turkey (YOK) and the Scientific and Technological Research Council of Turkey (TUBITAK).

ACKNOWLEDGEMENTS

Five years have been an amazing journey for me, many people have been contributed to my academic progress and this thesis. It would not have been possible without their help.

First and foremost, I would like to sincerely thank to my adviser, Prof. Dr. ÇETİN TAŞSEVEN. First for giving me the oppurtunity to conduct this study and then teach me how to independently think and solve problems.

I would like to offer my special thanks to Prof. Dr. TAHIR ÇAĞIN, who works at Texas A&M University. It has been an honor to work with him. His strong work ethic and creative thinking encourages his students.

Finally, I would like to extend my highest gratitude to my father ERDOĞAN AKGENÇ who has always been with me.

November, 2016

BERNA AKGENÇ

TABLE OF CONTENTS

Page

LIST OF SYMBOLS vii

LIST OF ABBREVIATIONS viii

LIST OF FIGURES ix

LIST OF TABLES xi

ABSTRACT xiii

ÖZET xv

CHAPTER 1

INTRODUCTION 1

1.1 Literature Review 1
1.2 Objective of Thesis 3
1.3 Hypothesis 4
1.4 Material Science and Piezoelectric Materials 8
1.5 Outline of the Present Work 12

CHAPTER 2

THEORY AND METHODOLOGY 14

2.1 Theory 15
2.1.1 Introduction 15
2.1.2 Many-Body Problems (Born – Oppenheimer Approximation) 18
2.1.3 Density Functional Theory 19
2.1.4 Exchange – Correlation Functions 23
2.1.5 Local Density Approximation 23
2.1.6 Generalized Gradient Approximation – Perdew Burke Ernzerhof 24
2.1.7 The Basic Flow Chart of DFT 25
2.2 Theory of Mechanical Properties 26
2.2.1 General Mathematical Defination 26
2.2.2 Stress and Strain 26
2.2.3 Elastic Compliance and Stiffness Constants 29
2.2.4 Voigt Notation 31

2.3 Theory of Piezoelectric Properties 33
2.3.1 Theoretical Background 33
2.3.2 The Piezoelectric Effect 34
2.3.3 Direct and Converse Piezoelectric Constants 34
2.3.4 Number of Independent Piezoelectric Coefficients 37
2.3.5 Piezoelectricity of ABO_3 type Perovskite Structures 39
2.3.6 $BaTiO_3$ 39
2.3.7 $SrTiO_3$ 40
2.3.8 $PbTiO_3$ 41
2.3.9 The Modes of Piezoelectric Coefficients 42

CHAPTER 3

MECHANICAL PROPERTIES OF ABO_3 PEROVSKITES AND THEIR ALLOYS .. 43

3.1 Introduction 43
3.2 Methodology 44
3.2.1 Construction of Alloys 44
3.2.2 Mechanical Properties of $BaTiO_3$ polymorphs 46
3.3 Results and Discussion 46
3.3.1 Pre-requirements for VASP 46
3.3.2 Position files of $BaTiO_3$ polymorphs 47
3.3.3 Structural Properties of ABO_3 Perovskite Structures 48
3.3.4 Elastic Properties of $BaTiO_3$ Polymorphs 49
3.3.5 Mixing Energies and Mechanical Stability of Alloying 60
3.4 Conclusion 62

CHAPTER 4

PIEZOELECTRIC PROPERTIES OF ABO_3 PEROVSKITE AND THEIR ALLOYS 63

4.1 Introduction 63
4.2 Methodology 64
4.3 Results and Discussion 64
4.3.1 Ground State Properties 64
4.3.2 Electrical Polarization 69
4.3.3 Calculation of Piezoelectric Coefficients 70
4.3.4 Calculation of Born Effective Charges 74
4.3.5 Calculation of Dielectric and Piezoelectric Constants 76
4.4 Conclusion 78

CHAPTER 5

CONCLUSION AND FUTURE WORKS 80

REFERENCES 82

APPENDIX -A

SUPPLEMENTARY MATERIALS 89

CURRICULUM VITAE 103

LIST OF SYMBOLS

T	Goldschmidt's Tolerance Factor
r_A	İonic Radii Of The A-Site Atom
r_B	İonic Radii Of The B-Site Atom
r_O	İonic Radii Of The Oxygen Atom
H	Hamiltonian
N	Electrons
K	Nucleus
Ψ	Electron Wave Function
$\rho(r)$	Electron Density
$V_{ion}(r)$	Ionic Potential
$V_H(r)$	Hartree Potential
$V_{XC}(r)$	Exchange-Correlation Potential
σ_{ij}	Strain
ε_{kl}	Stress
F	Force
C_{ijkl}	Elastic Stiffness Coefficients
S_{ijkl}	Elastic Compliance Coefficients
ϵ	Strain Matrix
I	İdentity Matrix
V_0	Volume Of Unstrained Lattice
a	Lattice Constant
B_0	Bulk Modulus
E_0	Total Energy
B_0'	First Derivative Of Bulk Modulus
e_{ijk}	Direct Piezoelectric Coefficient
d_{ijk}	Converse Piezoelectric Coefficient
P_i	Polarization
E_i	Elecric Field
$Z^*_{i\alpha\beta}$	Born Effective Charge
U	Internal Energy
G	Gibbs Free Energy
T	Temperature
S	Entropy
$Z^*_{i\alpha\beta}$	Born Effective Charge

LIST OF ABBREVIATIONS

BEC	Born Effective Charge
BO	Born – Oppenheimer
BZT	Barium Zirconate Titanate
DFPT	Density Functional Perturbation Theory
DFT	Density Functional Theory
GGA	Generalized-Gradient Approximation
LDA	Local Density Approximation
PBE	Perdew-Burke-Ernzerhof
PBT	Lead Barium Titanate
PW91	Perdew – Wang Function
PZT	Lead Zirconate Titanate
SBT	Strontium Barium Titanate
SPT	Strontium Lead Titanate
SZT	Strontium Zirconate Titanate
TAMU	Texas A&M University
VASP	Vienna Ab-initio Simulation Package
VESTA	Visualization for Electronic and Structural Analysis
YTU	Yildiz Technical University

LIST OF FIGURES

Page

Figure 1.1 The 32 crystal classes 5
Figure 1.2 Prototype perovskite of $BaTiO_3$ (Cubic, Pm3m) 6
Figure 1.3 Piezoelectric material before, during and after polarization 6
Figure 1.4 Direct piezoelectric effect 7
Figure 1.5 Indirect piezoelectric effect 7
Figure 1.6 Unit cell of ABO_3 type perovskite structure in both the (a) cubic Pm-3m structure and (b) tetragonal P4mm structure 9
Figure 2.1 All calculated exchange – correlation potentials versus elastic constants and lattice parameter changing 16
Figure 2.2 All calculated energy cut-off versus elastic constants and lattice parameter changing 16
Figure 2.3 All calculated k-mesh points versus elastic constants and lattice parameter changing 17
Figure 2.4 Typical methods in computational materials science in terms of size and time 20
Figure 2.5 Visualization of the Hohenberg-Kohn Theorem 22
Figure 2.6 The schematic of local and semilocal density approximation by LDA and GGA [94] 24
Figure 2.7 The Flow cart of the iteration steps of DFT 25
Figure 2.8 Systematic description of (a) an unreformed lattice and (b) a deformed lattice 27
Figure 2.9 Diagram for stress components on the surfaces of and cubic cell 27
Figure 2.10 The elastic behavior of cubic crystal 31
Figure 2.11 Part of Heckmann diagram 34
Figure 2.12 Schematic showing the (a) direct and (b) converse piezoelectric effect 35
Figure 2.13 Form of the d_{ijk} matrix for tetragonal from and 4mm class 39
Figure 2.14 Displacement of atoms in tetragonal phase of $BaTiO_3$ 40
Figure 2.15 Displacement of atoms in tetragonal phase of $SrTiO_3$ 41
Figure 2.16 Schematic of modes of piezoelectricity that depends on the crystal orientation 42
Figure 3.1 All possible arrangements for 2x2x2 supercell used in different concentration 45
Figure 3.2 40 atoms in $Pb_8Zr_xTi_{8-x}O_{24}$ cell with (a) 0.125:0.875and (b) 0.25:0.75 stoichiometric ratio 46
Figure 3.3 Changes in strain energy as a function of strain for cubic $BaTiO_3$ 51
Figure 3.4 Changes in strain energy as a function of strain for tetragonal $BaTiO_3$ 52
Figure 3.6 Cohesive energies as a function of concentration in SPT, PBT, SBT,PZT, BZT and SZT. 55

Figure 3.7 Total energies as a function of primitive cell volume for 2x2x2 cubic structures 56
Figure 3.8 The variation of elastic constants as a function of concentration in PZT, BZT and SZT 58
Figure 3.9 Convex hull diagram for A-type perovskite cubic alloy (a) $Pb_{(1-x)}Ba_xTiO_3$ (b) $Sr_{(1-x)}Ba_xTiO_3$ (c) $Sr_{(1-x)}Pb_xTiO_3$ 61
Figure 3.10 Convex hull diagram for B-type perovskite cubic alloy (a) $BaZr_{(1-x)}Ti_xO_3$ (b) $PbZr_{(1-x)}Ti_xO_3$ (c) $SrZr_{(1-x)}Ti_xO_3$ 61
Figure 4.1 Total energy per formula unit versus volume for eight different stoichiometric ratio doping atom that is Pb on $BaTiO_3$ 66
Figure 4.2 The variation of lattice constants as function of concentration and dependence on symmetry inequivalent configurations in PBT, SBT and SPT 68
Figure 4.3 The variation of lattice constants as function of concentration and dependence on symmetry inequivalent configurations in PZT, SZT and BZT 69
Figure 4.4 d_{33} direct piezoelectric constants for $Pb_xBa_{(1-x)}TiO_3$ (a) , $Sr_xBa_{(1-x)}TiO_3$ (b) and $Sr_xPb_{(1-x)}TiO_3$ (c) with the tetragonal P4mm structure 71
Figure 4.5 c/a ratio for different concentration of tetragonal phase $Pb_xBa_{(1-x)}TiO_3$ ... 72
Figure 4.6 Dielectric constants of $Pb_{(1-x)}Ba_xTiO_3$ according to Ba concentration..... 77

LIST OF TABLES

Page

Table 1.1 Bravais Lattice Types 4
Table 1.2 Tolerance factor t, validity ranges and corresponding perovskite structures 9
Table 2.1 Numbers of elastic constants for the crystal structures 29
Table 3.1 Crystal structure of $BaTiO_3$ polymorphs and their space group 47
Table 3.1 Crystal structure of $BaTiO_3$ polymorphs and their space group (Cont.)..... 48
Table 3.2 The calculated structural properties for pure perovskites 49
Table 3.3 Applied strains ε_i and corresponding energy densities 51
Table 3.5 Calculated structural properties of PZT perovskites 54
Table 3.6 The calculated elastic constants for pure perovskites 57
Table 3.7 The calculated elastic constants (Cij in GPa) for PZT 59
Table 4.1 The calculated structural properties for $Pb_xBa_{(1-x)}TiO_3$ 67
Table 4.2 Comparative Born effective charges for different ABO_3 perovskites 75
Table 4.3 Calculated piezoelectric coefficients for $BaZr_{(1-x)}Ti_xO_3$ cubic form 78
Table A.1 The calculated elastic constants of SPT 89
Table A.2 The calculated elastic constants of PBT 90
Table A.3 The calculated elastic constants of SBT 90
Table A.4 The calculated elastic constants of PZT 91
Table A.5 The calculated elastic constants of BZT 91
Table A.6 The calculated elastic constants of SZT 92
Table A.7 The calculated structural properties of SPT 92
Table A.8 The calculated structural properties of PBT 93
Table A.9 The calculated structural properties of SBT 93
Table A.10 The calculated structural properties of BZT 94
Table A.11 The calculated structural properties of SZT 94
Table A.12 The calculated dielectric constants of SPT 95
Table A.13 The calculated dielectric constants of SPT 95
Table A.14 The calculated dielectric constants of SBT 96
Table A.15 The calculated dielectric constants of BZT 96
Table A.16 The calculated dielectric constants of SZT 97
Table A.17 The calculated dielectric constants of PZT 97
Table A.18 The calculated direct piezoelectric constants of PBT 98
Table A.19 The calculated converse piezoelectric constants of PBT 99
Table A.20 The calculated direct piezoelectric constants of SBT 99
Table A.21 The calculated converse piezoelectric constants of SBT 100
Table A.22 The calculated direct piezoelectric constants of SPT 100
Table A.23 The calculated converse piezoelectric constants of SPT 100

Table A.24 The calculated direct piezoelectric constants of PZT 101
Table A.25 The calculated converse piezoelectric constants of PZT 101
Table A.26 The calculated direct piezoelectric constants of BZT..... 101
Table A.27 The calculated converse piezoelectric constants of BZT..... 102
Table A.28 The calculated direct piezoelectric constants of SZT 102
Table A.29 The calculated converse piezoelectric constants of SZT 102

ABSTRACT

A STUDY OF THE RELATION OF PIEZOELECTRIC PROPERTIES AND NANO STRUCTURES THROUGH METHODS IN COMPUTATIONAL PHYSICS

Berna AKGENÇ

Department of Physics

Ph.D. Thesis

Adviser: Prof. Dr. Çetin TAŞSEVEN

Co-adviser: Prof. Dr. Tahir ÇAĞIN

The increasing demand for power has made us look for alternative forms of renewable energy with oil resources going down. Among the various types of alternative energy, piezoelectricity has been gaining popularity over the past few years.

In this study, the generalized-gradient approximation (GGA) has been implanted on density functional theory (DFT) and density functional perturbation theory (DFPT) to obtain the ground state structural, elastic properties and dielectric, piezoelectric properties of various ABO_3 type ceramics and their $\{A_xA'_{(1-x)}\}BO_3$ and $A\{B_xB'_{(1-x)}\}O_3$ alloys, respectively. To represent alloy perovskites, we employ supercells with species A, A'=Ba, Sr, Pb; B, B'=Ti, Zr. The effects of composition and atomic configuration/order on lattice structure, thermodynamics, elastic constants and dielectric properties are evaluated.

In calculations, we have used linear response and homogeneous field methods and we have also provided an assessment of the performance of these approaches in determination of aforementioned properties. The results of the A/B site complex perovskite calculation show that the alloy perovskites can be mixed mechanically and thermodynamically.

As the first aim of the thesis, we have observed dielectric and piezoelectric properties for the cubic form of alloy perovskites. Even though the cubic forms of alloy perovskites don't have any piezoelectric properties, since the crystallographic site is occupied by different type of atoms, the inversion symmetry breaks down and the structures develop

small tetragonality due to which a piezoelectric behavior is expected. We have obtained nonzero piezoelectric coefficients coefficient for $BaZr_{(1-x)}Ti_xO_3$, the maximum magnitude of which was $0.554 \times 10^{-15} C/N$. The perovskites alloys are more likely to be piezoelectric candidates in the near future, opening a door to find and design new non-centrosymmetric perovskites. We hope that piezoelectric perovskite alloys whose piezoelectric coefficient are in the feasible range of $\backsim 10^{-12} C/N$ or larger.

The second aim of the thesis deals with the elastic and piezoelectric properties of tetragonal type ABO_3 alloy perovskite structures that are considered tetragonal at zero hydrostatic pressure. We have calculated the piezoelektric properties of ABO_3 type perovsites and their effect of A-sites and B-sites on piezoelectricity. We have obtained results twice or three times higher than the nominal value of piezoelectric coefficients.

The main objective of the thesis is to give a comprehensive study of the piezoelectic phenomeon and to design previously unknown and tremendous piezoelectric coefficient ABO_3 type perovskite structures.

Key words: First-principle calculations, perovskites, elastic constants, $BaTiO_3$ crystals

ÖZET

HESAPLAMALI FİZİK YÖNTEMLERİ İLE PİEZOELEKTRİK ÖZELLİK VE NANOYAPI İLİŞKİLERİNİN İRDELENMESİ

Berna AKGENÇ

Fizik Anabilim Dalı

Doktora Tezi

Tez Danışmanı: Prof. Dr. Çetin TAŞSEVEN

Eş Danışman: Prof. Dr. Tahir ÇAĞIN

Yakıt kaynaklarının giderek azalması ile birlikte enerji gereksinimin artması alternatif yenilenebilir enerji kaynakları arayışına sebep olmuştur. Bu alternatif enerji türlerinden piezoelektrik son yıllarda popülerlik kazanmıştır.

Bu çalışmada, genelleştirilmiş gradyent yaklaşımı, yoğunluk fonksiyonel teorisi ve yoğunluk fonksiyonel pertürbasyon teorisi içerisinde kullanılmıştır. Bu teoriler sayesinde sırası ile ABO_3 ve onların $\{A_xA'_{(1-x)}\}BO_3$ and $A\{B_xB'_{(1-x)}\}O_3$ tipindeki alaşımların temel durum yapı ve elastik özellikleri ile dielektrik ve piezoelektrik özellikleri elde edilmiştir. Alaşım perovskitini temsil etmek için, A, A'=Ba, Sr, Pb; B, B'=Ti, Zr türleri kullanılarak süper hücre elde edilmiştir. Örgü yapısı, termodinamik, elastik sabitler ve dielektrik özellikler üzerindeki kompozisyon ve atomik konfigürasyon/düzen etkileri değerlendirilmiştir.

Hesaplamalarda ise, lineer tepki ve homojen alan yöntemleri kullanılmış olup; söz konusu özelliklerin belirlenmesine yönelik bu yaklaşımların performans değerlendirmesi sağlanmıştır. A/B konumlarindaki kompleks perovskitlerin hesaplama sonuçları alaşım perovskitlerinin mekaniksel ve termodinamik olarak karışabileceğini göstermiştir.

Tezin ilk hedefi olarak, alaşım perovskitlerinin kübik formunda dielektrik ve piezoelektrik özellikler gözlemlenmiştir. Alaşım perovskitlerinin kübik formlarının herhangi bir piezoelektrik özellik göstermemesine rağmen, kristolografik konum farklı türdeki atomlar tarafından işgal edilmiş olduğu için ter simetri bozulur ve yapılar küçük tetragonalite geliştirir. Bu sayede piezoelektrik davranışın ortaya çıkması beklenir. $BaZr_{(1-x)}Ti_xO_3$ için sıfır olmayan piezoelektrik katsayısı $0.554 \times 10^{-15} C/N$ büyüklüğünde elde edilmiştir. Alaşım perovskitlerinin yakın gelecekte piezoelektrik

malzeme adayı olması muhtemeldir. Bu sayede, yeni merkezi simetriye sahip olmayan perovskitlerin bulunması ve tasarlanmasına olanak sağlanacaktır. Piezoelektrik katsayısı $\backsim 10^{-12}\mathrm{C/N}$ ya da daha büyük olan piezolektrik alaşım perovskitlerinin elde edilmesi umulmaktadır.

Tezin ikinci hedefi sıfır hidrostatik basınç altında tetragonal formda olan ABO_3 alaşım perovskit yapılarının elastik ve piezoelektrik özellikleri ile ilgilidir. ABO_3 tipi perovskitlerin piezoelektrik özellikleri ve bunların A- konumu ve B- konumlarının piezoelektriklik üzerine etkileri hesaplanmıştır. Elde edilen sonuçlar piezoelektrik katsayılarının normal değerinin iki ila üç katı büyüklükte olduğunu göstermiştir.

Bu tezin asıl hedefi, piezoelektrik olgusu üzerine kapsamlı bir çalışma yapmak ve daha önceden bilinmeyen çok büyük piezoelektrik katsayılı ABO_3 tipi perovskit yapılarını tasarlamaktır.

Anahtar Kelimeler: İlk – prensipler hesaplamaları, perovskitelar, elastik sabitleri, $BaTiO_3$ kristalleri

CHAPTER 1

INTRODUCTION

1.1 Literature Review

The increasing demand for power has made us look for alternative forms of renewable energy with oil resources going down. Among the various types of alternative energy, piezoelectricity has been gaining popularity over the past few years. Piezoelectric materials are widely used in advanced technological interest applications. Due to their large dielectric constants, they are used in capacitors. In attempt to reduce vibration, piezoelectric fibers have been embedded in computer chips. Since ferroelectric materials also show piezoelectric and pyroelectric properties, they are used in transducer applications. A deformation on piezoelectric material changes between the positive and negative charge at the crystal structure. Similarly, under electric charge piezoelectric materials are affected by a deformation. For this reason, they can be used both as sensors and actuators. The continued development of piezoelectric materials has huge marketing area in daily life such as electronic and opto-electronic devices, resonators for clocks, atomic force microscopes, inkjet printers, and stress sensors for aircrafts, power applications and energy harvesting devices. These applications all employ piezoelectric effects in three-dimensional crystals.

Piezoelectric materials can convert mechanical energy to electrical energy and vice versa. The root of the word “piezo” means, “pressure” in Greek; the original meaning of the word ‘piezoelectricity’ is pressure-electricity. The piezoelectricity was discovered by the Jacques and Pierre Curie brothers in 1880 [1]. They showed that when a mechanical stress was applied on crystals such as tourmaline, topaz, quartz, Rochelle salt and cane sugar, electrical charges appeared. The charge was proportional to the stress. In other words, the polarization of the material change in response to an applied strain is called “direct

piezoelectricity". A year later, Gabriel Lippmann discovered the "converse piezoelectricity" [2]. This important property was mathematically deduced from the fundamental thermodynamics principle [3-4]. Converse piezoelectricity basically can be explained as the material's exhibiting a geometric strain/deformation proportional to an applied electric field [5].

The next few decades its the discovery, piezoelectricity remained in the laboratory level. The first serious applications were made during World War I with piezoelectric ultrasonic transducers. This initial use of practical piezoelectric applications generated the new area for the piezoelectric devices. During the World War II, Japanese and Russian research groups worked on improved capacitor materials that exhibited dielectric constants up to 100 times higher than common crystals. They are called ferroelectric, which are new class of man-made materials.

Besides the discovery of piezoelectricity, many theoretical researchers studied how to define crystallographic principle of the piezoelectric effect. For any crystal to be a piezoelectric material, it should not have a center of inversion symmetry. In 1910, Voight published the first textbook on physical crystallography, in which he shows the description of the piezoelectric effect [6]. With the help of the textbook, the crystallographic principle of the piezoelectric effect even in complex crystallographic crystal structures was clearly understood. Voight termed piezoelectricity as "tensor" which contributed to the development of the theory of piezoelectricity so much.

We performed alloy form of perovskite structure in a high-throughput computational search. The possible alloy form of perovkite crystals are also screened for thermodynamic stability. Our prior screening a set of 6 different pure perovskites such as $BaTiO_3$, $SrTiO_3$, $PbTiO_3$, $BaZrO_3$, $SrZrO_3$ and $PbZrO_3$ to use as alloy form. Screened alloy forms are assigned as promising candidate for future experiments. We used the Vienna Ab-initio Simulation Package (VASP) for theoretical calculations. The program is based on Density Functional Theory (DFT) exchange-correlation energy evaluated by generalized-gradient approximation (GGA) using the Perdew-Burke-Ernzerhof (PBE) function.

In the past decade, fast oxygen conducting materials are deeply outlined in the design of future fast-ion conductors. Before the modeling of oxygen perovskites, it also should be studied their mechanical, dielectric and piezoelectric properties.

After that, piezoelectric crystals were intensively studied because of their symmetry-dependent properties at the piezoelectric and ferroelectric industry. According to today's Innovative Research and Products Inc. report [7], the global marketing of piezoelectric actuators and motors were projected to reach $12.3 billion in 2014. ABO_3 type perovskite oxides attracted comprehensive attention in the early 1950's because of its excellent performance in commercial applications.

ABO_3 formula is the simplest case of perovsite family. Compounds of $A^{+2}\,B^{+4}\,O_3$ type perovsites have been performed the basis of ionic radii of the constituent ions. The Coulomb repulsions between B cation and oxygens have a criticial important for moving of B cation displacement. Hines et al. describe the perfect perovsite is to consider the corner cation linked BO_6 octahedra. This octahedral tilting is related to the sizes of A and B cations.

1.2 Objective of Thesis

Perovskite type crystals have attracted much attention due to their outstanding physical properties such as pyroelectricity, ferroelectricity, dielectricity, and piezoelectricity [8-15]. Since the discovery of piezoelectricity, much investigation has been performed and reported on literature that covers the piezoelectric effect of the pure form of perovskite crsytals both experimentally and theoretically. The discovery of barium titanate ($BaTiO_3$) in the 1940s prompted intense research in the area of piezoelectric oxides. After a series of studies, lead zirconate titanate (PZT), and lead titanate became the most attractive materials to use for piezoelectricity in the 1970s and 1980s. Afterward, there were many efforts to design new oxide piezoceramics. There are more than 10 million known compounds that have non-centrosymmetric structures, and the search to find the most efficient and highest piezoelectric constants has been the focus of much research.

More than 2,000 scientific papers that concern perovskite materials are published every year. They particularly focus on the preparation, structure explanation, and applications of these materials. The challenges of ceramic science have been identified by the International Congress on Ceramics workshop in 2012 [16]. The challenges are listed as two types: understanding the events in ceramic microstructures and controlling the properties of oxide electronics.

Because the perovskite oxide (general stoichiometric formula of ABO_3) type crystals are ceramics, it is necessary to investigate their elastic properties to understand the physical

phenomena and to design a better device performance. Based on the mechanical properties of the crystal, the piezoelectric response can also be easily affected by elastic deformation.

1.3 Hypothesis

The properties of some materials may depend closely on their crystal structure. Some of the materials show different properties under external conditions. A very common and effective example is carbon and diamond. In a diamond, which is made out of highly organized carbon atoms, the carbon atoms are arranged tetrahedrally exhibiting extraordinary hardness, strength, and durability.

Each crystal is defined by their positive and negative ions that occupy lattice sites of the crystal structure. The unit cell, the simplest repeating unit in a crystal, characterizes the crystalline material. The unit cell's geometry can be completely described by the set of three edge lengths (a, b and c) and three interaxial angles (α, β and γ). Based on the geometrical symmetry, there are 14 different crystal types, which are called Bravais lattices.

Table 1.1 Bravais Lattice Types

Crystal System	Axials Lengths	Angles	Bravais Lattices
Cubic	$a = b = c$	$\alpha = \beta = \gamma = 90°$	P, I, F
Tetragonal	$a = b \neq c$	$\alpha = \beta = \gamma = 90°$	P, I
Orthorhombic	$a \neq b \neq c$	$\alpha = \beta = \gamma = 90°$	P, I, C, F
Monoclinic	$a \neq b \neq c$	$\alpha = \beta = 90° \neq \gamma$	P
Triclinic	$a \neq b \neq c$	$\alpha \neq \beta \neq \gamma = 90°$	P
Trigonal	$a = b = c$	$\alpha = \beta = \gamma < 120° , \neq 90°$	P, C
Hexagonal	$a = b \neq c$	$\alpha = \beta = 90°, \gamma = 120°$	P

The 14 Bravais lattices can be categorized into seven crystal systems (cubic, tetragonal, orthorhombic, trigonal, hexagonal, monoclinic and triclinic); the cubic systems contain

P, I, C, and F type characteristic that are referred to as cubic, body-center cubic, base-center cubic, and face-center cubic, respectively, as shown in Table 1.1.

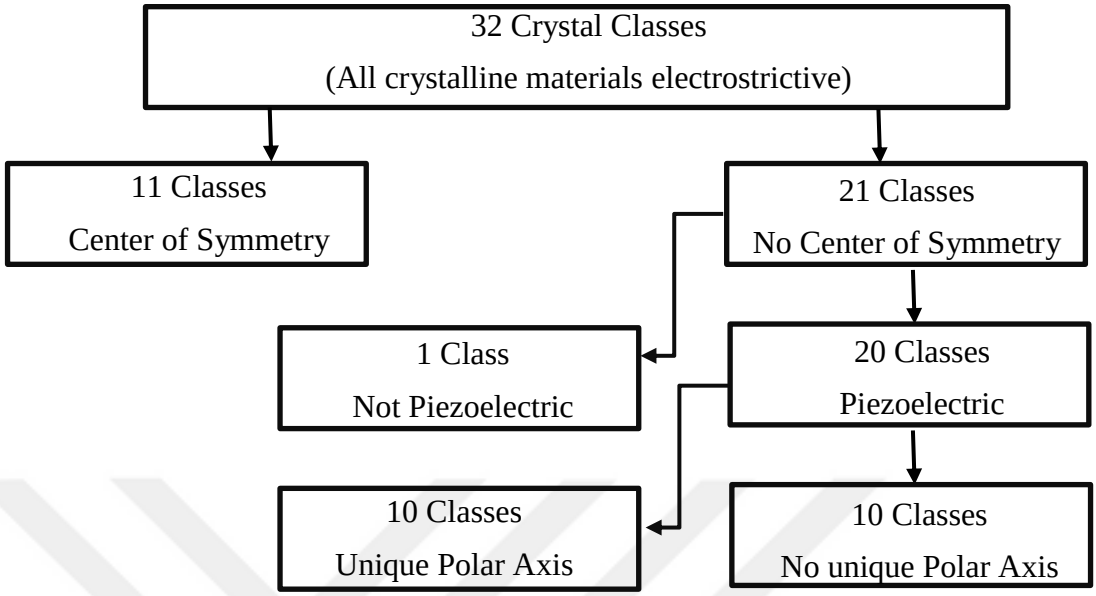


Figure 1.1 The 32 crystal classes

Even though the deformation is minor under external forces such as mechanical stresses, applied electric fields or temperature changes, all materials are usually altered in some way. According to the structure of the material, a minor change may result in varying electric polarization. Hence, it can exhibit ferroelectric, piezoelectric or pyroelectric effects. It can be imaged that all materials consist of a type of crystalline structure. The specific symmetry of a unit cell determines whether or not the crystal exhibits piezoelectric, pyroelectric, or ferroelectric effects. 11 point crystal groups are unable to produce piezoelectric effects with one exception, being Class 29. This class does not have a center of symmetry but has other symmetry elements that combine to exhibit the piezoelectric property. Figure 1.1 shows the 32 crystal classes. 20 out of 32 crystal classes exhibit the piezoelectric effect, and they are always associated with non-centrosymmetric crystals. Non- centrosymmetric crystals that are lacking a center of inversion can exhibit a variety of technologically important physical properties such as piezoelectricity, ferroelectricity, and pyroelectricity [17]. In a typical non-centrosymmetric crystal structure such as perovskite oxides, the A-type cation is located in the unit cell's corners, and the B-type cation resides in the middle of the unit cell, while the anion, commonly oxygen is located in the center of the face edges. A-type can be a monovalent, divalent, or trivalent metal, and B-type can be a pentavelant, tetravalent, or trivalent element. The perovskite prototype with an ABO_3 structure and a Pm3m space group (#225) is a

structure in which the A-site atoms are in a Wyckoff position 1b, (½, ½, ½) and the B-site atoms in position 1a (0,0,0), and the oxygen atoms in positions 3d (½, 0, 0), (0, ½, 0), and (0, 0, ½). All special positions are shown in Figure 1.2. The figure was created using VESTA.

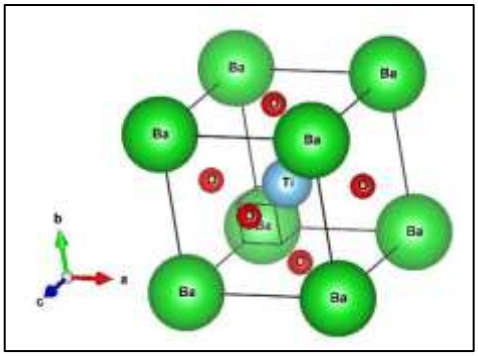


Figure 1.2 Prototype perovskite of $BaTiO_3$ (Cubic, Pm3m)

The ABO_3 type perovskite crystals have been widely used in industry for decades due to their excellent mechanical, optical, and piezoelectric properties. They can be used as high-dielectric constant capacitors, ferroelectric thin film memory devices, sensors, actuators, piezoelectric sonars, and switches. These properties make them desired items in the fields of physics, chemistry, material science and engineering.

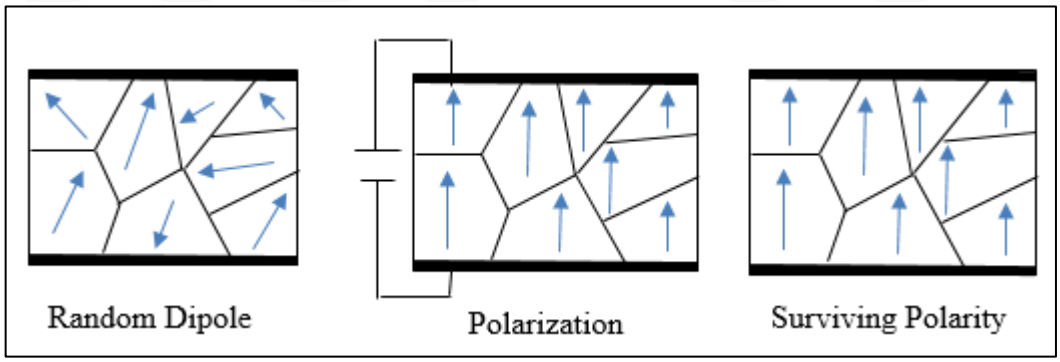


Figure 1.3 Piezoelectric material before, during and after polarization

Figure 1.3 shows the simplest model of the piezoelectric effect. It explains the resulting polarity of an electric field applied on the material. Neighboring areas are separated by boundaries called domain walls. Before applying an electric field or some external stress to the material, domains are regions with the same polarization direction. The spontaneous polarization at each domain shows different directions in which negative and positive charges are cancelled. A reorientation of the spontaneous polarization occurs because of the applied the electric field. Most of the reorientation is retained after the

electric field is longer applied. However, domain walls revert back to their original position [18].

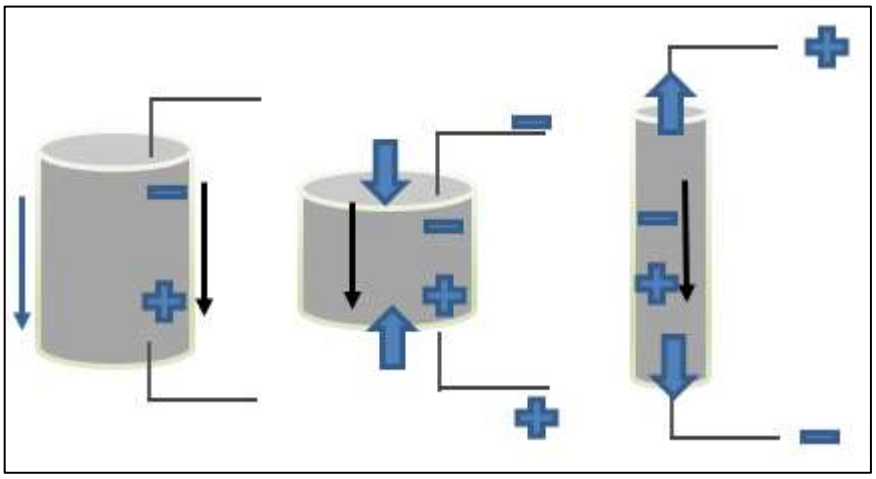


Figure 1.4 Direct piezoelectric effect

Basically, pressure generates charge on the surface of the piezoelectric material. The direct piezoelectric effect, which converts mechanical energy into electrical energy, is also called the generator or sensor effect. Figure 1.4 shows that the applied stresses on piezoelectric materials induce electric polarization. If the material is compressed, then a voltage of a certain polarity will appear between the electrodes. If the material is extended, a voltage of the opposite polarity will appear.

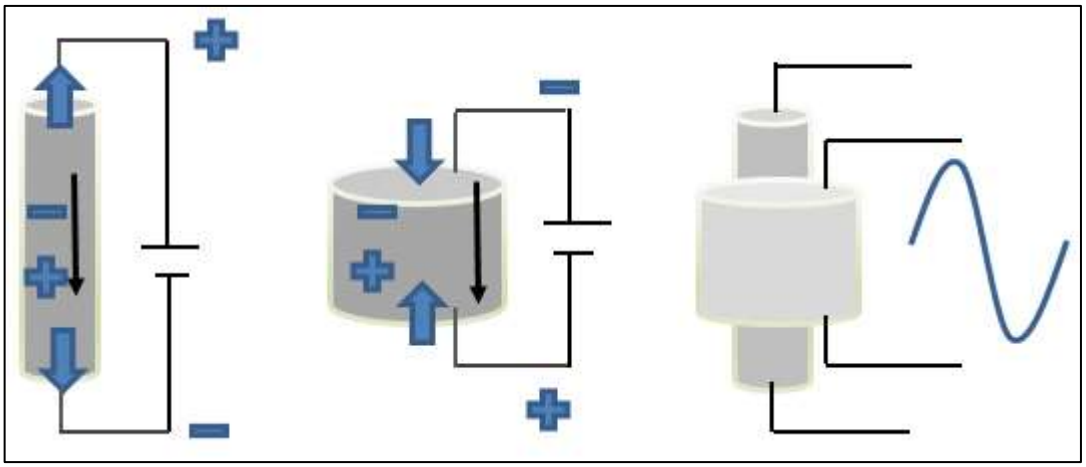


Figure 1.5 Indirect piezoelectric effect

Conversely, the reverse of the piezoelectric effect is applied, is called the converse piezoelectric effect where an applied electric field causes a mechanical deformation in the crsytal. Figure 1.5 shows that the material will expand under a particular voltage

polarity and will compress when a voltage of the opposite polarity is applied. Finally, if an AC signal is applied, the material will vibrate at the same frequency.

1.4 Material Science and Piezoelectric Materials

First, it is important to understand the molecular structure of perovskite materials because of their piezoelectric qualities. The atoms of these crystals are held together by ionic bonds. The structure of ionic crystals is a result of the electrostatic attraction. The crystal that has a net non-zero charge in each unit cell is a typical non-centrosymmetric crystal structure. Piezoelectric materials have an asymmetric atomic arrangement. This asymmetry leads to the formation of electric dipole moments. Special geometries make it possible for a dipole moment to be induced through the application of mechanical stress. The three main factors in the production of piezoelectricity are the size effect, the Jahn-Teller effect, and changing the composition from the ideal ABO_3 [19].

ABO_3 type ceramics are great technological materials and the best studied family of oxides because of their industrial and commercial applications such as high-dielectric constant capacitors, ferroelectric thin film memory devices, sensors, actuators, piezoelectric sonars and switches. The ceramics that are characterized with having a perovskite structure are some of the most thoroughly studied piezoelectric crystals. Technically, perovskite structure is defined by the oxides of ABO_3, where A and B symbolize different cations, and O represents oxygen. The A-site of the ABO_3 perovskite structure is positioned at the corner of the unit cell, B- site is set at the body center of the unit cell, and both are coordinated by the six oxide ions forming an octahedron while the oxygen atoms are located at the face centers of the unit cell. The asymmetric location of the B-site on the ABO_3 type perovskite crystals in the unit cell develops an electrical polarity, consequently transforming the unit cell to contain electric dipole moments. A mechanical stress that is applied to the crystal shifts the position of the B-site ion of the ABO_3 type perovskite structure, thus changing the polarization strength of the crystal. This is the source of the direct piezoelectric effect. When the crystal is subjected to an electric field, it also results in a relative shift in the position of the B-site ion of the ABO_3 type perovskite structure, leading to the distortion of the unit cell and making it more or less tetragonal. This is the source of the converse piezoelectric effect.

The piezoelectric behavior is formed by the lack of inversion symmetry. The off-center atomic displacement in the crystal along the z-axis allows for the occurrence of

ferroelectricity. As seen in Figure 1.6, this ferroelectricity is consequence of the presence of a switchable spontaneous electric polarization which appears in $BaTiO_3$, $PbTiO_3$, $BaZrO_3$, etc. [20]. The off-center atomic displacement lies along the z-axis in the crystal.

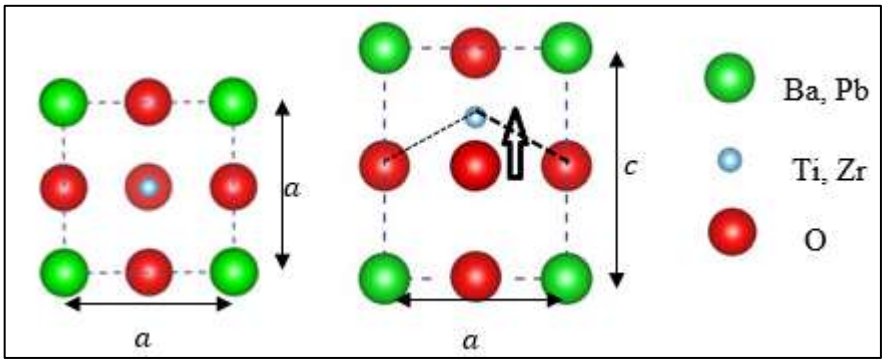


Figure 1.6 Unit cell of ABO_3 type perovskite structure in both the (a) cubic Pm-3m structure and (b) tetragonal P4mm structure

Goldschmidt et al. invented a basic way to express the compounds of the perovskite family [21]. Using an ionic radii model, Goldschmidt investigated the perovskite materials and developed a semi-empirical relationship known as Goldschmidt's tolerance factor expressed as

$$t = \frac{r_A + r_O}{\sqrt{2}(r_B + r_O)} \tag{1.1}$$

where r_A, r_B, and r_O are the ionic radii of the A-site, B-site, and oxygen atoms, respectively. The possible validity ranges and its corresponding perovskite structures are shown in Table 1.2.

Table 1.2 Tolerance factor t, validity ranges and corresponding perovskite structures

t value	Effect	Possible structures
$t > 1$	A-site cations are too large to fit into their interstitials	Hexagonal perovskite
$t \sim 0.9 - 1.0$	Ideal conditions	Cubic perovskites
$t \sim 0.71 - 0.9$	A-site cations are too small to fit into their interstitials	Orthorhombic perovskite Rhombohedral perovskite

Table 1.2 Tolerance factor t, validity ranges and corresponding perovskite structures (Cont.)

$t < 0.7$	A-site and B-site cations are same size	Closed package structure

Changing the composition from the ideal ABO_3 perovskite family of compounds can be explained by the valence of the B-site atoms. It occurs in either an oxidizing or a reducing environment. The Jahn- Teller effect could be responsible for the distortion of the structure in some perovskites [22]. The odd number of electrons in the orbital results in an elongation of the octahedron. Any oxygen vacancy problems and the Jahn –Teller effect have not been calculated in this thesis.

This part of the chapter provides the literature search areas that are related to piezoelectricity. It all started with two brothers: Pierre and Jacques Curie. Curie brothers published an article that showed the promising experimental results on piezoelectric materials. Since this discovery of piezoelectricity over a century ago, piezoelectric materials were widely used in technological, industrial, and commercial applications as smart materials. Paul Langevin invented the first industrial application of piezoelectric single crystals around 1917 [23]. Cohen and Krakauer have investigated the first theoretical investigations of $BaTiO_3$ and $PbTiO_3$. They have proved that the Ti - O hybridization is responsible for ferroelectric instability. And they also have discussed the nature of ferroelectric phase transition including effects of electrical boundary conditions [24]. Further still, Vanderbilt and Smith have developed a systematic study of eight various perovskites via the ultrasoft-pseudopotential method and the local density approximation (LDA) [25]. Cora and Catlow have examined the electronic structure of a wide range of perovskites using the ab-initio Hartree- Fock method [26]. The elastic constant C_{ij} also plays a significant role in calculating the piezoelectric constants of the crystal from the first principle calculations. The areas of interest here are the “density functional theory (DFT)” and “piezoelectric materials”. The literature part of the thesis is concluded numerous articles. A couple outstanding essays on the first principle calculations and on piezoelectric materials that have been published in the past decade are listed below:

The DFT study of $ATiO_3$ compounds, where A represents the atoms Ca, Sr, Ba, Ra, Cd, Mg, Ge, Sn, and Pb, have revealed that the geometrical size and the configuration of the

outer electron shell of the A-type atoms are responsible for determining the off-center position of the A-type atoms. Gonzalez-Garcia et al. have investigated the effect of the substituent concentration on structural parameters, band gap energy, mixing enthalpy, and the phase diagram of $In_{1-x}B_xP$ semiconductor alloys. It has been found that the lattice parameters of the $In_{1-x}B_xP$ alloys decrease with B-concentration. The shows a negative deviation from Vegard's law, while the bulk modulus increases with composition x, thus showing a large deviation from the linear concentration dependence [27]. Theoretical analysis has been carried out in $In_xAl_{1-x}N$ alloys on the applicability of Vegard's linear rule and deviations from its linearity with regard to composition, piezoelectric polarization, surface orientation and degree of strain [28]. It has been found that $Bi(Zn_{1/2}Ti_{1/2})O_3$ and the PZT solid solution display extremely large cation displacements and tetragonality. The A- site displacement directions vary more than B- site displacement directions due to the influence of the B-cation agreement on cation displacement that is stronger in the A- site [29]. J. Bennett et al. have investigated ground state structural properties of $Sn(Al_{1/2}Nb_{1/2})O_3$ (SAN) solid solution and demonstrated that these alloys can be synthesized due to their favorable thermodynamics properties, and that they possess enhanced ferroelectric and piezoelectric properties [30]. S. Halilov et al. have investigated the main instabilities in $CdTiO_3$ and $Cd_{0.5}Pb_{0.5}TiO_3$ to show the piezoelectric potential of this perovskite alloy that may provide much larger energy density than the traditional composition [31]. Though some reports have mainly focused on B-site alloying, A-site alloying is investigated here in addition to B-site alloying. The alloys that were constructed are $\{A_xA'_{1-x}\}BO_3$ and $A\{B_xB'_{1-x}\}O_3$ for which x is varied from 0 to 1 with species A, A'=Ba, Sr, Pb; B, B'=Ti, Zr. A. Erba et al. have computed the piezoelectric tensor of ferroelectric $SrTiO_3$ at low temperatures by $ab\ initio$ theoretical simulations. They found that there is a large effect to the piezoelectric response because of the large zero-point motion of Ti atoms [32]. M. de Jong et al. have presented a large database of calculated intrinsic piezoelectric constants for use in design and development of piezoelectric materials and devices [33]. On the other hand, many researches have been focused on piezoelectricity in two-dimensional materials that exhibit stronger piezoelectric coefficients [34]. J. Shi and et al. have calculated the polarization and d_{33} in the contributions of the A-site and B-site atoms of the tetragonal structures of $PbTiO_3$, $BaTiO_3$, and $KNbO_3$. In $PbTiO_3$, Pb and Ti make comparable contributions to the total d_{33}, but in $BaTiO_3$, the contribution of Ba increases rapidly with an increase in the $c-$axis [35]. A. Mahmoud et al. have adopted a computational

approach that represents four different levels of approximations by comparing computed and experimental structural and vibrational properties of polymorphs of $BaTiO_3$. PBE approximation has found the most reliable way to accurately describe dielectric and photo elastic properties [36]. Among the famous piezoelectric systems, $PbZr_{(1-x)}Ti_xO_3$ (PZT) is the most studied perovskite. S. Kim et al. have found that of all the structures, PZT (Zr/Ti =52/48) with a tetragonal ($P4mm$) phase shows the lowest formation energy to remain stable and has the highest piezoelectric coefficient using DFT. Because the perovskite structure piezoelectric coefficient is the highest value, the ABO_3 type piezoelectric coefficients have been calculated [37]. Many researchers have computationally investigated all the mixing ratios that are possible in a 40-atom supercell involving any combination of two perovskites. The same method was also used for all alloy forms.

1.5 Outline of the Present Work

The aim of this thesis is to investigate the effects of alloying (concentration and structural/chemical anisotropy) on the thermodynamic, structural, mechanical, and electromechanical properties for broad concentration ranges at zero hydrostatic pressure rather than providing comprehensive data for pure ABO_3 compounds for various existing polymorphs. We focused to design new, previously unknown high performance ABO_3 type perovskite structures.

We have constructed $\{A_xA'_{1-x}\}BO_3$ and $A\{B_xB'_{1-x}\}O_3$ alloys for which x is varied from 0 to 1 with species A, A′=Ba, Sr, Pb ; B, B′=Ti, Zr. The effects of A-atom site and B-atom site identifying properties of those alloys such as structural properties, elastic constants, dielectric constants, Born effective charges and piezoelectric constants are shown.

First, the methods used in calculation of perovskite properties as well as the computational details of this study are described. Chapter 2 deals with the general framework of DFT using the projector augmented wave method. Owing to there being an abundant of reviews, articles, and books about DFT in literature, only the basic concept of DFT and its practical applications will be the focus.

We present the comprehensive study of computational details and theoretical background of mechanical properties and its calculation methods with elastic and compliance constants in the mathematical perspective in Chapter 3 and Chapter 4. The chosen compounds are $BaTiO_3$, $SrTiO_3$, $PbTiO_3$, $BaZrO_3$, $SrZrO_3$, and $PbZrO_3$ because of their

scientific and technological importance. The results regarding structural, mechanical, and elastic properties of ABO_3 type perovskites are included and discuss the A- site and B-site effect on the piezoelectric coefficient in Chapter 3. The thermodynamic stability of perovskite alloys is also investigated. The dielectric, Born-effective charges, the piezoelectric properties as direct and converse piezoelectric constants in the mathematical perspective, and their results and discussion are given in Chapter 4.

This is followed by the summary of the main results and conclusions in Chapter 5. The Vienna *ab initio* simulation package (VASP) program that used for first-principle calculations in details is also introduced. The technical details for each system such as kinetic energy cut-off for plane waves and k-point mesh considered valence electrons are outlined in Appendix 1.

CHAPTER 2

THEORY AND METHODOLOGY

Computation is now an indispensable partner in scientific fields. Computational science allows one to build new models that make predictions of what happened in the laboratory. Doing a particular experiment can be too expensive or too dangerous in the laboratory. Computational science reduces and eliminates dangers which are expected cause environmental pollution while modeling and simulating the physical world. Meanwhile with the growth of computation power, theoretical tools have highlighted computational material science as its own field. Computational material science tends to avoid cost and time-consuming materials and, at the same time, help build new materials for the use in harsh operating conditions for current and future technology applications. Especially in today's high DFT calculations, there being an alternative to experiments allows for the ability to scan through many materials for required properties. Elastic constants and associated mechanical properties, i.e. bulk modulus, shear modulus, Young's modulus, and Poisson's ratio of a large number of complex ceramic crystals with different crystal symmetries have been calculated by means of the DFT [17]. The main challenge in estimating elastic constants from the first principles not only requires an accurate method to calculate the total energy but also requires a decrease in the computation that is involved.

The DFT and density functional perturbation theory (DFPT), along with different types of approximation that has comprehensive detail, will be introduced in the second part of this chapter. Vienna *ab initio* simulation package, better known as VASP, performs DFT at *ab initio* quantum- mechanical molecular dynamics simulations using pseudo potentials or the projector- augmented wave method and a plane wave basis set. This chapter provides basic information of first-principle calculations to provide a general perspective and the application of the VASP program [38].

2.1 Theory

2.1.1 Introduction

Basically, forces and full stress tensors can be calculated with VASP and used to relax atoms into their instantaneous ground state. DFT is presented, which is used to model electron- electron interactions, together with the approximation needed to perform first-principle calculations. This is not to say that these calculations are trivial, they are certainly critical for getting reliable calculations [37]. The most important input files in the program such as INCAR, POTCAR, POSCAR, and K-POINTS are used to begin calculations with VASP.

The POSCAR file defines crystal structure. The file contains the lattice geometry and ion positions. The POTCAR file contains the pseudopotential for each atomic species used in the calculation. Besides the pseudopotential, the file also gives the mass, valence electrons, and the energy of the reference configuration. There are five different types of pseudopotentials in VASP program. The KPOINTS file contains the k-point coordinates and weights or the mesh size for creating the k-point grid. The most critical file is the INCAR file that determines ‘what to do and how to do it’. The file contains a relatively large number of parameters.

It is known that in any accurate first-principle simulations, it is necessary to test the accuracy of exchange- correlation potential forms, sufficient k-point meshes, and energy cut-offs [35]. Before the calculations, the most suitable exchange-correlation potential among LDA, GGA, and PBE were found. All potentials at convenient energy cut off and k-point meshes were calculated. It is known that GGA gives overestimated values while LDA gives underestimated values. PBE exchange- correlation potentials were used in all cases. At the same time, there is a good database called Materials Project (2) developed by MIT to compare the selected values [36]. It is shown that when the system under study becomes large and complex, computational cost increases exponentially.

Figure 2.1, Figure 2.2, and Figure 2.3 show some benchmark calculations for testing the convergence of the exchange-correlation potentials, energy cut-off versus elastic constants, and k-mesh points versus elastic constants, respectively. The test case $BaTiO_3$ in cubic form of perovskite structure is considered here.

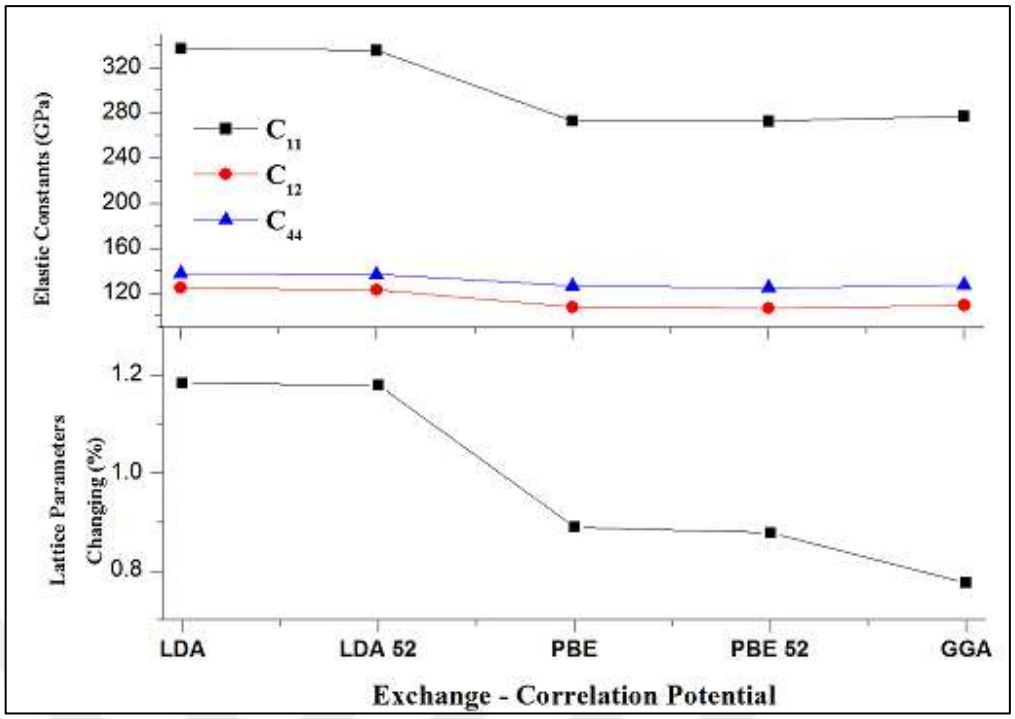


Figure 2.1 All calculated exchange – correlation potentials versus elastic constants and lattice parameter changing

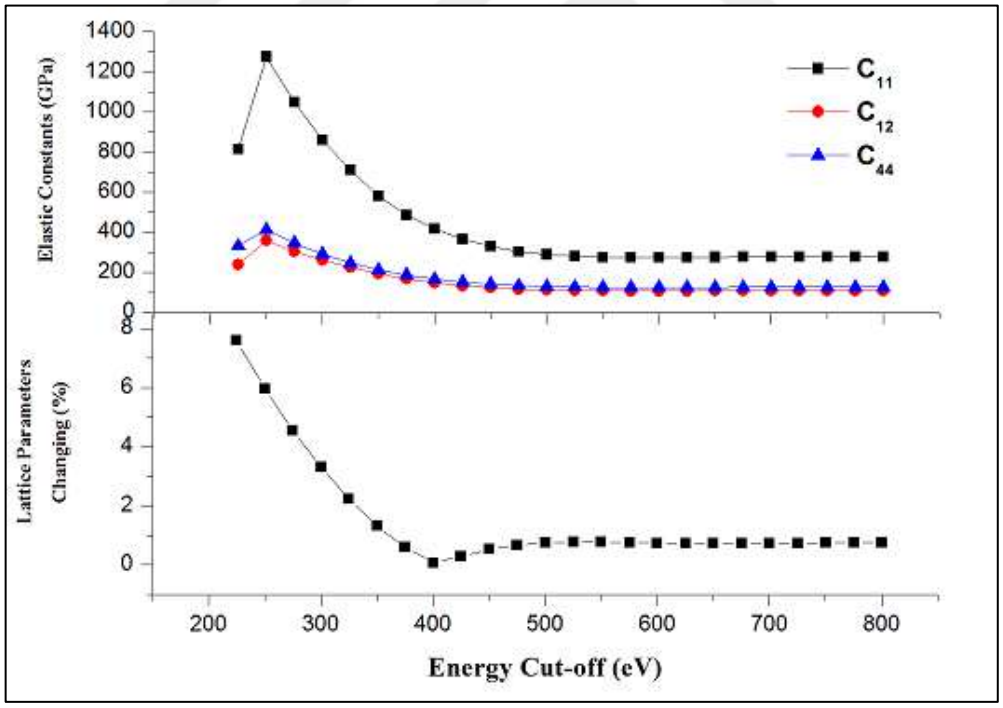


Figure 2.2 All calculated energy cut-off versus elastic constants and lattice parameter changing

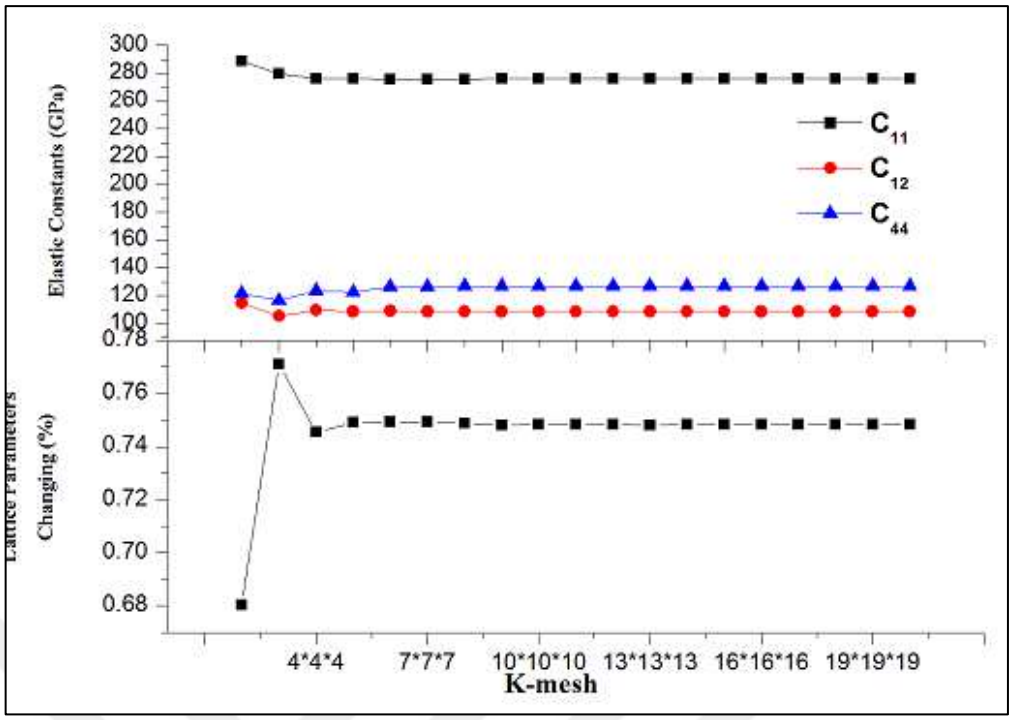


Figure 2.3 All calculated k-mesh points versus elastic constants and lattice parameter changing

After the determination of the k-points and energy cut-off parameters, it is introduce how to guess the lattice parameter and the other physical properties based on the information available in the upcoming chapter.

The relaxed-ion and clamped-ion elastic stiffness tensors are obtained using the finite difference method, while the relaxed-ion and clamped-ion piezoelectric tensors are obtained using DFPT. MATLAB is used to calculate elastic compliance tensors from elastic stiffness tensors. The kinetic energy cut-off of the electronic wave function and the k-point mesh have been optimized for total energy convergence for the studied structures and are set to 600 eV and $8\ x\ 8\ x\ 8$ Monkhorst- Pack grid for the Brillouin zone integration respectively. However, to improve the accuracy further, the elastic constants calculations were performed using the same energy cut off value with a $4\ x\ 4\ x\ 4$ k-point mesh, which provided the needed convergence.

It is necessary to define the atom types selected and what their valence electrons were, giving Ba, Sr, Pb for A-sites and Ti and Zr for B-sites. Ba atoms $5s^2 5p^6 6s^2$, Sr atoms $4s^2 4p^6 5s^2$, Pb atoms $5d^{10} 6s^2 6p^2$, Zr atoms $4s^2 4p^6 4d^2 5s^2$, Ti atoms $3p^6 3d^3 4s^1$, and O atoms $2s^2 2p^4$are considered as valence states in the construction of the pseudopotentials. Calculations were performed with the following common parameters: convergence criterion for an energy of $10^{-5} eV$, the convergence criterion for the maximal

force between the atoms at 0.005 eV/Å in the geometrical relaxation process, and maximum ionic steps of 100 for all cases in order to make sure the calculations are standard.

2.1.2 Many-Body Problems (Born – Oppenheimer Approximation)

Many-body problems related to physical problems that contain microscopic systems made of a large number of interacting particles. In order to obtain the most realistic system, all interactions need to be taken into account as much as possible such as electron-electron and, electron-ion interactions in solids [39]. It requires the use of the Hamiltonians model. DFT is an elegant method to finding solutions to the fundamental equation that describes the quantum behavior of atoms and molecules by mapping it to a much more easily solved, non-interacting problem [40]. When the system is investigated in the quantum-chemistry level, it should be noted that the atomic nucleus are is 1,800 times heavier than the electrons, meaning that, the electrons have more moving capability than their corresponding nucleus. As a result, the problem should be split into two pieces with the *Born – Oppenheimer (BO) Approximation*. The approximation assumes that the motion of nucleus and the electrons in a molecule can be separated.

For an interacting particle in the presence of a potential the time-independent Schrodinger equation can be written as:

$$H\Psi = E\Psi \tag{2.1}$$

where H is the Hamiltonian function of the system, which includes five different parameters. N and K demonstrate interesting solids and molecules comprising of numerous electrons and nuclei, respectively. Thus, the Hamiltonian function can be expressed as

$$H = -\sum_{i=1}^{N}\frac{1}{2}\nabla_i^2 + -\sum_{k=1}^{K}\frac{1}{2M_k}\nabla_k^2 + \frac{1}{2}\sum_{i,j=1,i\neq j}^{N}\frac{1}{|\vec{r_i}-\vec{r_j}|} + \frac{1}{2}\sum_{k,k`=1,k\neq k`}^{K}\frac{Z_k Z_{k`}}{|\vec{R_k}-\vec{R_{k`}}|} - \sum_{i=1}^{N}\sum_{k=1}^{K}\frac{Z_k}{|\vec{r_i}-\vec{R_k}|} \tag{2.2}$$

In this expression the first two terms account for the kinetic energy of the electrons and the nuclei, and the third and fourth terms express the electron-electron and nucleus-nucleus Coulomb repulsions, while the last term represents an electron-nucleus attraction potential. The Hamiltonian equation cannot be solved for each electron wave function

associated with the other electrons. Some approximations are needed to solve these many-body problems.

Solving the Schrodinger equation is the fundamental problem of quantum mechanics. Exact solutions of the Schrodinger equations for many- particle systems are not analytically possible even though some solutions can be found for a few very simple systems such as the helium or lithium Schrodinger equations. The DFT allows the N-electron wave function $\Psi(x_1, x_2, \dots, x_n)$ and its associated Schrodinger equation to be replaced by an electron density $\rho(r)$ that is in a much easier form to handle. On the other hand, the many-body electron problem switches to the alternative fabrication independent- particle problem. In this case, the electron density $\rho(r)$ is N times the summation of the square of the wave function over the entire electronic space given as

$$\rho(r) = \sum_i |\psi_i(r)|^2 \tag{2.3}$$

2.1.3 Density Functional Theory

Taking a look of "the history of DFT," the basic idea of the electron density $\rho(r)$ at each point r determines the ground-state properties of an atomic or molecular system, which goes back to the early work of Thomas, Fermi, and Dirac in the late 1930s on the free electron gas. This model is the first attempt to describe many-body electrons on the basis of electron charge density instead of electron wave functions [37]. In the original Hohenberg- Kohn paper, this theorem is proven for densities with non-degenerate ground states. It is assumed that there exists two different potentials, that yield the same density.

The understanding and controlling of many particle systems have been an important goal in many fields within the physical sciences and engineering disciplines during this century. The aim of this chapter is not only to provide the DFT in details but also to deal with the foundation of the modern DFT in a practical context used in this thesis. For the past 50 years, the DFT has become the most popular method for diverse material modeling problems in computational physics, chemistry, materials science, and multiple branches of engineering [38]. Its popularity stems from its beautifully basic conceptual framework and computational elegance. DFT can be considered the most attractive method among all other quantum-chemical methods since it achieves an even higher efficiency for enormous systems and the relatively low computational cost. DFT has become more competitively accurate and needs less computational demand than the other standard methods such as the Hartree-Fock method, Hückel method, self-consistent field

(SCF) method in quantum-chemistry and solid-sate physics software such as ABINIT, CASTEP, SIESTA,GAUSSIAN, VASP; thereby it enables unique advantages.

The general perspective of the materials at the atomic level within Born-Oppenheimer approximation is described here. The basics of DFT and its related exchange- correlation approximations are likewise introduced.

DFT calculations consist of quantum mechanics modeling with first- principle calculations. As shown in Figure 2.4, all five methods are described in terms of system size and simulation time with basic formulas. The quantum mechanics methods consider nuclei and electrons as the basic particles and describe events in the subatomic world. Molecular Dynamics (MD) describe the system by using Newton's equations of motion. MD considers atoms as the basic particles, and it disregards nuclei and electrons. Hundred billion atoms can be simulated by MD in order to generate the interacting potential. The Monte Carlo (MC) method is a statistical technique that includes random walks for sampling and the Boltzman factor to solve problems. Meso-scale methods calculate algebraic, differential and integral equations by a computer-based numerical technique [94].

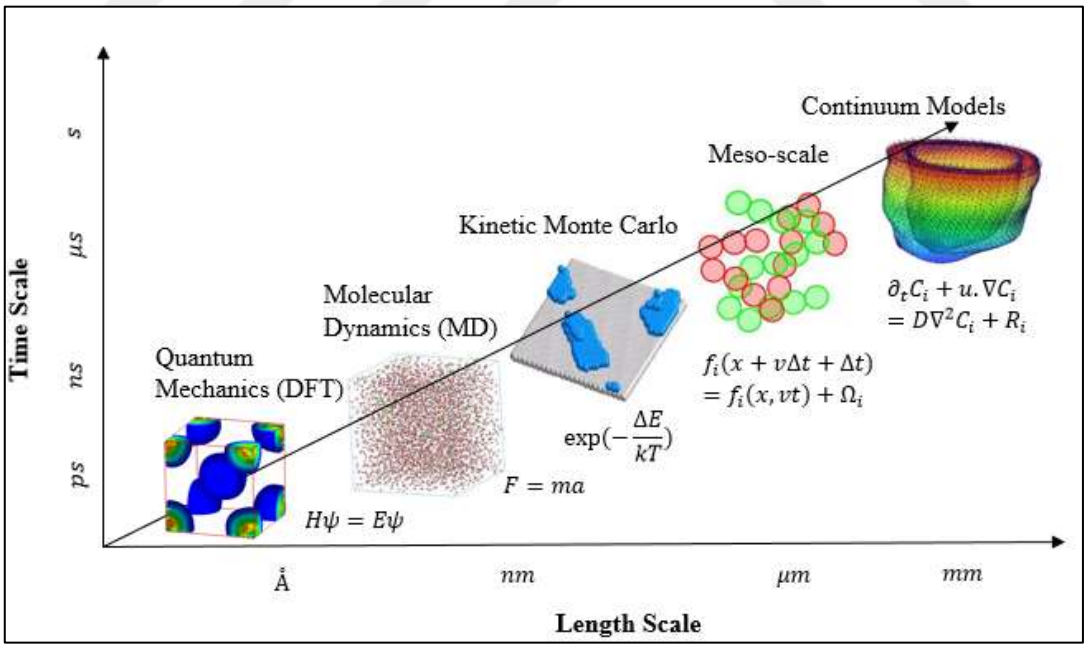


Figure 2.4 Typical methods in computational materials science in terms of size and time

The local density approximation was introduced by Kohn and Sham in 1965 and has been the most successful approximation until early 90s. LDA approximation is widely used in

solid-state simulations even though it has typical errors of about 1% of the atomic positions and lattice constants and error or 5% on phonon frequencies with respect to experimental data. The biggest error is shown in the electronic band gap estimation. LDA systematically gives underestimated results when the values are compared to the experiments it actually stems from using *local* density. Even at the exchange and correlation level, the function should be *non-local*, that is, it should depend on r and r' simultaneously. Developing the *non-local* exchange-correlation function is a much more difficult task. Recently, substantial effort has been put toward to produce an exchange-correlation function that is depend not only on density $\rho(r)$ but also on its gradients. That alternative approximation is called *Generalized Gradient Approximations (GGA)*, which works better for finite systems as molecules, surfaces, etc. Both approximations show values that are closer to experimental values if the calculations are performed under initial experimental parameters. Because there are many ways to describe the gradient of electron density in the GGA function, a large number of GGA function can be studied. The most widely used function are the Perdew -Burke -Ernzerhof (PBE) and Perdew-Wang functions (PW91). Each of these functions are functional with the GGA function, and all calculations are carried out within GGA -PBE approximation in this study. The GGA -PBE approximation was choosen because of its high accuracy compared to the other approximations.

Highly accurate DFT modeling is necessary for understanding the basis of various properties used in high advanced technology and also in order to design and explore new materials. DFT calculations can be used as vital tools to understand complex solid bulk systems because of their methodological improvements and faster computational speeds. First- principle calculations are intensively used to specify ground state properties of metals, semiconductors, and insulators [41].

The Thomas – Fermi (TF) method has described atoms as uniformally distributed electrons around nuclei in zero-temperature. It provides the simplification of the many-body problem. The TF approach replaces the problem of calculating an N-electron wavefunction problem by calculating the electron density [100]. The major error in the TF approach streams from approximating the kinetic energy as density function. Because of the kinetic energy is equal to the absolute value of the total energy in the Coulombic systems, the errors that occurred are huge.

DFT relies on two fundamental mathematical theorems, which is demonstrated by Hohenberg and Kohn and a deviation of a set of equations by Kohn and Sham [42].

1. The ground state energy from Schrodinger's equation is a unique function of electron density.

2. The electron density that minimizes the energy of the overall function is the true electron density corresponding to the full solution of the Schrodinger equation.

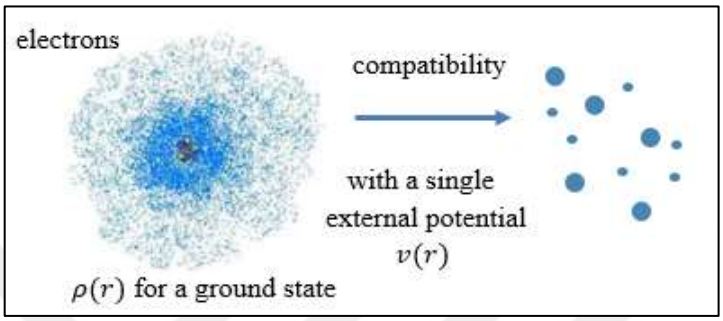


Figure 2.5 Visualization of the Hohenberg-Kohn Theorem

Hohenberg and Kohn improve the DFT by replacing the many-body electrons problem by finding certain approximations for electron charge density as seen in Figure 2.5 and then solving the single-electron equations [43]. The determination of electron density is independent of the total number of electrons. To get the set of wave functions $\psi_i(r)$ that minimize the total energy function, the Kohn- Sham equations are used and given as:

$$\left[\frac{-\hbar^2}{2m}\nabla^2 + V_{ion}(r) + V_H(r) + V_{XC}(r)\right]\psi_i(r) = \varepsilon_i\psi_i(r) \tag{2.4}$$

Here, $\psi_i(r)$ is the wave function of the electron state i, ε_i is the Kohn- Sham eigenvalue of the state $\psi_i(r)$, and r is the electron coordinates. This equation is similar to Equation (2.4) without the summation and its subscripts.

On the left side of the equation, there are three potentials: $V_{ion}(r), V_H(r)$, and $V_{XC}(r)$. $V_{ion}(r)$ covers the interaction between an electron and the collection of atomic nuclei. $V_H(r)$ is called the Hartree potential, whereas $V_{XC}(r)$ is the exchange-correlation potential.

The Hartree and exchange-correlation potentials are defined as the functional derivative of the Hartree and exchange-correlation energy with respect to the electron density distribution as described below in Equation (2.5) and Equation (2.6).

$$V_H = \frac{\delta E_H[n]}{\delta n(r)} \tag{2.5}$$

and

$$V_{XC} = \frac{\delta E_H[n]}{\delta n(r)} \tag{2.6}$$

The equations can be solved self-consistently by replacing the many-electron problems, which are an equivalent set of self-consistent one-electron equations. On the other hand, the exchange- correlation potential V_{XC} that contains all the electron interactions going beyond the classical Coulomb interaction has to be approximated [44].

2.1.4 Exchange – Correlation Functions

The Kohn- Sham method can determine the exact ground state of a system of many- body electrons if the exchange- correlation between electrons is known. However, the specification of the exchange-correlation term is hard and approximations are performed to estimate this term. The other struggle is capturing all the many- body effects. Solving for the many- body electron concept has not been answered analytically thus far. Because there are many problems that remain in this active research area, researchers are looking for some kind of approximations.

2.1.5 Local Density Approximation

Local Density Approximation (LDA)'s idea is build from the knowledge of the exchange-correlation energy per particle of the uniform electron gas. The simplest and easiest to implement is the density functional approximation called *Local Density Approximation (LDA).* LDA, in which the exchange and correlation energy per electron is assumed to only bed dependent on the *local* density at this point, is supposed to be the same as the homogeneous electron gas with the density:

$$V_{XC}[n(r)] = \frac{\delta E^{XC}[n(r)]}{\delta n(r)} \tag{2.7}$$

The exchange part of the homogeneous electron gas can be obtained from Hartree-Fock technique given as

$$E^{XC}[n(r)] = -\frac{3}{4\pi}(3\pi^2 n)^{1/3} \tag{2.8}$$

The exchange-correlation energy at each point in the system is the same as that of an uniform electron gas of the same density. The density is given by

$$E_{xc}^{LDA} = \int \rho(r) E_{xc}(\rho) dr \tag{2.9}$$

where $E_{xc}(\rho)$ is the exchange-correlation energy per particle of an uniform electron gas of density ρ.

2.1.6 Generalized Gradient Approximation – Perdew Burke Ernzerhof (GGA-PBE)

PBE belongs to the class of generalized- gradient approximation (GGA) functions for the exchange- correlation energy E_{XC}. One of them is called PBE, which was proposed Perdew, Burke, and Ernzerhof. GGA functions include gradient correction without introducing experimentally fitted parameters. GGA functions are local in a mathematical sense such as at the point ($\vec{r}$), density $\rho(\vec{r})$, its gradient $\nabla\rho(\vec{r})$, and possibly parameters. This function is considered "non-local" as its motivation comes from the gradients, which is the first steps toward accounting for the inhomogeneity of the real density. Because both the density and the gradient of density are considered, it gives more accurate approximations for some of the physical phenomena at each point in space. Figure 2.6 shows how the schematic of local and semi-local density approximations by LDA and GGA work. Therefore, GGA returns to

$$E_{xc}^{GGA}[\rho(r)] = \int \rho(r)\, \varepsilon_{xc}^{GGA}[\rho(r), \nabla\rho(r)]dr \tag{2.10}$$

PBE presents a simplified and improved GGA version with no empirical elements. It also includes second-order gradients for the enhancement factors.

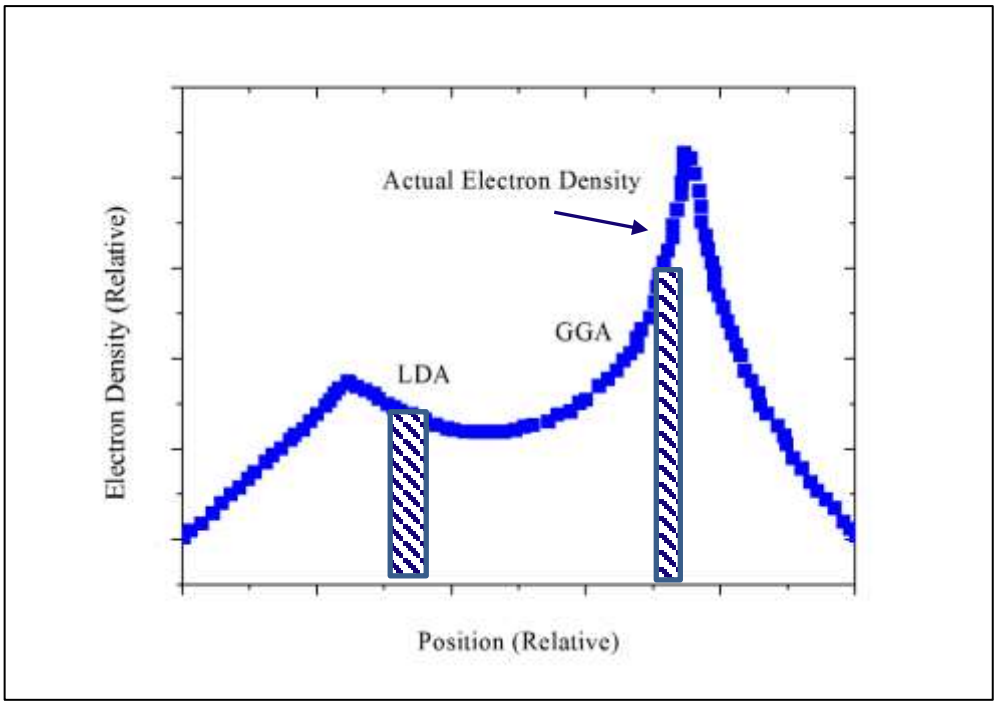


Figure 2.6 The schematic of local and semilocal density approximation by LDA and GGA [94]

2.1.7 The Basic Flow Chart of DFT

So far, DFT has been presented as a theoretically exact framework. A systematic flow cart of a self-consistent loop of the density functional method is presented in Figure 2.7.

First, an initial guess for the electron density is assumed, the effective potential is calculated, and the Kohn- Sham equations are solved in order to evaluate $\rho(r)$ and E_{tot}. The process is continued with the last $\rho(r)$ value replacing the initial guess of electron density. Once criterion is satisfied, various output quantities such as forces, eigenvalues, etc., are computed. When self-consistency is achieved for this loop, the electron part of the system is solved.

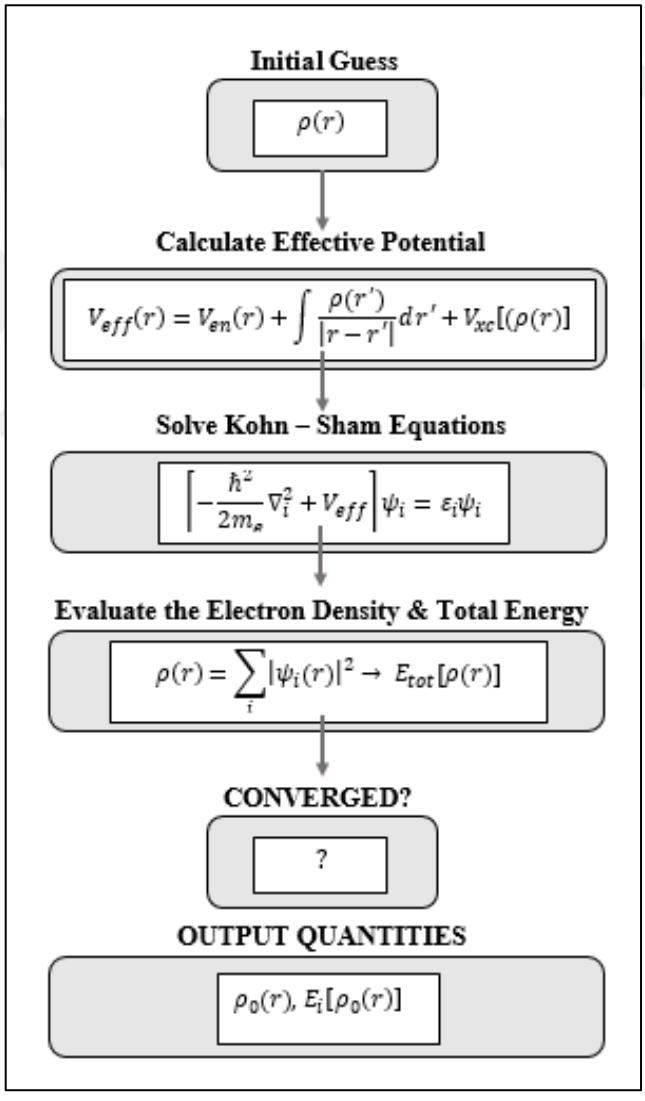


Figure 2.7 The Flow cart of the iteration steps of DFT

The energy of the configuration can be determined with respect to the atomic coordinates. It corresponds to the constant point of the function from the exact form. Quasi-Newton

methods or the conjugate gradient method are used to solve the iterative methods [45]. The quasi-Newton method is used to find either the minimum or local maximum of the functions. The obtained minimum energy value corresponds to the stable configurations. Detailed information on how we the alloys are constructed is in Chapter 3.

2.2 Theory of Mechanical Properties

2.2.1 General Mathematical Defination

In this chapter, theories of the physical properties of ABO_3 type perovskite structures and their mechanical characteristic calculations such as stress and strain, elastic compliance, and elastic stiffness constants are covered. For calculating the piezoelectric properties from a theoretical approach, the elastic properties are obtained first. For this reason, the mechanical properties and their calculation methods are detailed in this chapter, and then the piezoelectric properties and their calculation methods are explained in the upcoming chapter.

The mechanical behavior of materials is the subject of physics, engineering, and material science. Meanwhile, mechanical engineers directly measure stress, strain, hardness, forces, inelasticity, and elasticity, but material scientists calculate how materials deform or break as a function of applied load, time, temperature and other conditions. Beyond the physical reason for the mechanical behavior, it can be quite different depending on the type of the material. The elastic properties of a material are key component in describing its mechanical properties. In engineering terminology, adjectives such as elastic, ductile, and tough have very specific meanings [47]. These terms will be the qualitative description of these materials. Elastic properties is related to the piezoelectric properties. The description of piezoelectricity is directly related to the strain. Before calculating piezoelectricity, the understanding of the mechanical properties and their methods of calculations is important.

2.2.2 Stress and Strain

Elastic properties of the solid material are described by the relation of stress and strain. All solid materials respond to the application of moderate stress by changing their form, or size, or both. This change is considered strain or deformation. Strain in crystals is created by deformation and is described as relative lattice displacement. Figure 2.8 shows

the example of a 2D lattice model under strain. The nature of strain depends on the manner in which the stress is applied.

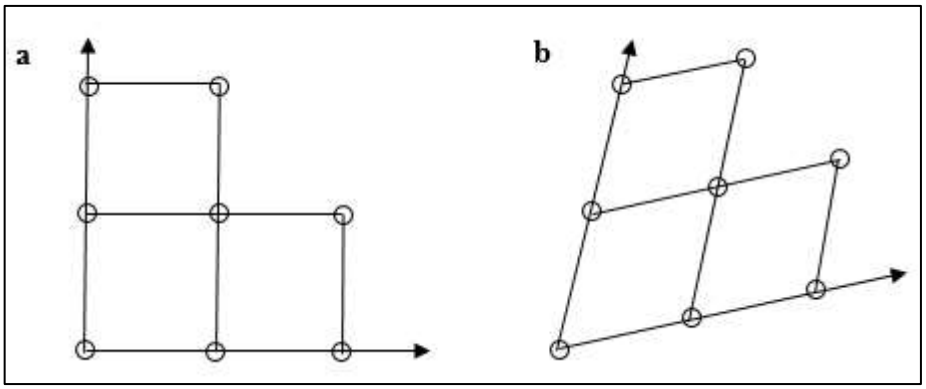


Figure 2.8 Systematic description of (a) an unreformed lattice and (b) a deformed lattice

Basically, stress measures the deforming force per unit area of the object**,** whereas strain measures the relative change in length caused by a deforming force**.** In other words, a solid resists deformations, therefore deformations will generate forces. Stress has nine components and is a second-rank tensor. A description of stress is given in Figure 2.9. Stress can be applied equally on all sides of a body, which is called pressure, or in a single direction called uniaxial stress [46]. A stress that can bend or twist a body is known as shear stress. Because strain can be expressed as a percentage change in length, in volume, or in shape it is commonly expressed as a percent without any metric units attached.

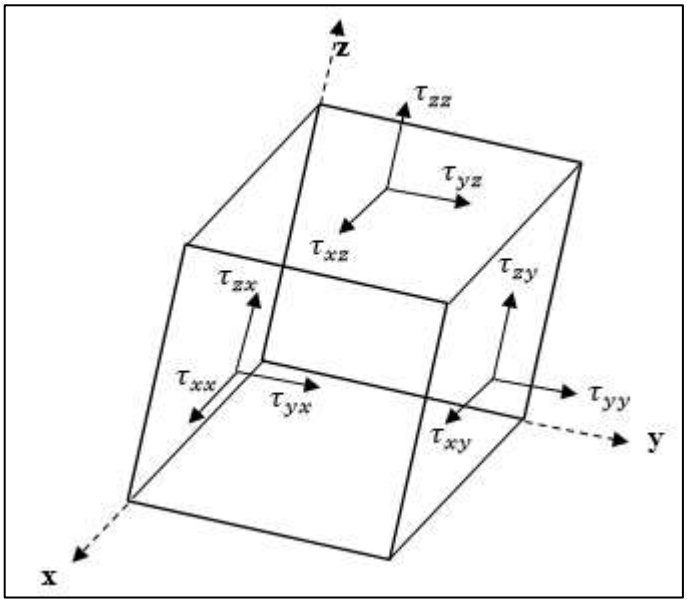


Figure 2.9 Diagram for stress components on the surfaces of and cubic cell

Stress and strain were clearly defined because they are necessary to understanding the elastic and piezoelectric properties of a continuous solid in the thermodynamic equilibrium. The stress (σ_{ij}), mathematically defined as the force per unit area measured in Pascals (Pa) is a second-rank tensor that is represented by a symmetrical tensor. The strain (ε_{kl}) defines a relative deformation of a body caused by stress. According to its definition, the stress is defined as an extension per unit length and also is a symmetrical second-rank tensor, but it is dimensionless.

The modern theory of elasticity is defined by Hooke's law. Hooke's law is defined as a strain on a solid material that is proportional to the stress.

$$F = k\,x, \tag{2.11}$$

where k is a positive real number and a characteristic of the spring, F is the magnitude of force, and x is the amount of displacement. The tensorial definition of Hooke's law is

$$\sigma_{ij} = S_{ijkl}\,\varepsilon_{kl} \tag{2.12}$$

S_{ijkl} defines the elastic compliance coefficients of the material and fourth rank tensor that 81 and 16 components for three-dimensional and two-dimensional problems, respectively. In the inverse relationship

$$\varepsilon_{ij} = C_{ijkl}\,\sigma_{kl} \tag{2.13}$$

defines the elastic stiffness coefficients C_{ijkl} and is the fourth-rank tensor. The elastic stiffness coefficients have the following minor symmetries that result from the symmetry of the stress and strain tensors:

$$\sigma_{ij} = \sigma_{j\iota} \rightarrow C_{jikl} = C_{ijkl} \tag{2.14}$$

From Hooke's law we have reduced the number to $81 = 3x3x3x3 \rightarrow 54 = 6x3x3$

In a similar way, we can use the symmetry of the strain tensor

$$\varepsilon_{ij} = \varepsilon_{j\iota} \rightarrow C_{jikl} = C_{ijkl} \tag{2.15}$$

In the end, all numbers of the material constants are reduced to $36 = 6x6$.

When considering Equation 2.15, this is further reduced to 21. The most general structure, the is triclinic lattice point group, has 21 material constants. The elastic stiffness coefficient can be written as

$$\begin{bmatrix}\sigma_{11}\\ \sigma_{22}\\ \sigma_{33}\\ \sigma_{23}\\ \sigma_{13}\\ \sigma_{12}\end{bmatrix} = \begin{bmatrix} C_{1111} & C_{1122} & C_{1133} & C_{1123} & C_{1113} & C_{1112} \\ & C_{2222} & C_{2233} & C_{2223} & C_{2213} & C_{2212} \\ & & C_{3333} & C_{3323} & C_{3313} & C_{3312} \\ & & & C_{2323} & C_{2313} & C_{2312} \\ & & & & C_{1313} & C_{1312} \\ & & & & & C_{1212} \end{bmatrix} \begin{bmatrix}\varepsilon_{11}\\ \varepsilon_{22}\\ \varepsilon_{33}\\ \varepsilon_{23}\\ \varepsilon_{13}\\ \varepsilon_{12}\end{bmatrix} \tag{2.16}$$

Obviously, the elastic compliance coefficients and the elastic stiffness coefficients are the coordinates of a tensor that is inverse of the stiffness tensor:

$$C_{ijkl}{}^{-1} = S_{ijkl} \tag{2.17}$$

This equation directly show that the elastic compliance coefficients S_{ijkl} obey the same symmetry relations as the elastic stiffness coefficients.

Due to the symmetry of the stress and strain, there are a maximum of 36 independent components of elastic compliance and stiffness coefficients where their number can be reduced according to the symmetry of the material. Table 2.1 shows the number of elastic constants for the different types of crystal structures [3].

Table 2.1 Numbers of elastic constants for the crystal structures

Lattice (Point Group)	Numbers of Elastic constants
Triclinic	21
Monoclinic	13
Orthorhombic	9
Tetragonal (4,-4,4/m)	7
Tetragonal (422,4mm, -42/m, 4/mmm)	6
Hexagonal and Rhombohedral (3, -3)	7
Hexagonal and Rhombohedral (32, 3m, -32/m)	6
Hexagonal (6, -6, 6/m, 622, 6mm,-62m, 6/mmm)	5
Cubic	3

2.2.3 Elastic Compliance and Stiffness Constants

Elasticity is the property of a solid material where it returns to its original shape and size after the forces that deformed it have been removed. Due to the elastic properties, this can be used to describe the mechanical behaviors of different materials, which have been

widely studied both theoretically and experimentally for various materials. Mechanical properties are used to describe particular parameters of the material when external forces are applied. The elastic tensors are the sum of two main contributions: electronic "clamped-ion" contributions and the ionic "relaxed-ion":

$$C_{ijkl} = \frac{d\sigma_{ij}}{d\varepsilon_{kl}} = \frac{\partial\sigma_{ij}}{\partial\varepsilon_{kl}} + \sum_k \frac{\partial\sigma_{ij}}{\partial u_{k,i}} \frac{\partial u_{k,i}}{\partial\varepsilon_{kl}} = C_{ijkl}^{el} + C_{ijkl}^{ion} \quad (2.18)$$

The first term of the equation refers the frozen (clamped-ion) ion elastic tensor, the second term of the equation covers contributions from force-response internal stress and displacement response internal strain tensors. Clamped-ion elastic tensor is generally not physically relevant quantities.

In accordance with the finite strain continuum elasticity theory the elastic constants are calculated by means of Taylor expansion of the total energy with a small strain force. The elastic stiffness constants have been obtained by straining the equilibrium lattice at fixed volumes, using volume-conserving strains and then computing the free energy as a function of strain. It can be stated as a matrix form (R) the distortion of the lattice (R') is expressed by multiplying R with a symmetric distortion matrix which is written as:

$$R' = (I + \epsilon)R \quad (2.19)$$

where I is the $3x3$ identity matrix, ϵ is a matrix containing the strain components and R' is the displacement of strained system, respectively.

$$\epsilon = \begin{pmatrix} \epsilon_{11} & \epsilon_{12} & \epsilon_{13} \\ \epsilon_{12} & \epsilon_{22} & \epsilon_{23} \\ \epsilon_{13} & \epsilon_{23} & \epsilon_{33} \end{pmatrix} \quad (2.20)$$

The energy of the strained system can be expressed by a Taylor series expansion as a Lagrange elastic strain:

$$E(V, \varepsilon) = E(V_0, 0) + V_0 \sum_{i=1}^{6} \sigma_i \varepsilon_i + \frac{1}{2!} V_0 \sum_{i,j=1}^{6} C_{ij} \varepsilon_i \varepsilon_j + \frac{1}{3!} V_0 \sum_{i,j,k=1}^{6} C_{ijk} \varepsilon_i \varepsilon_j \varepsilon_k \quad (2.21)$$

where ε and σ are the strain and stress tensors, respectively. V_0 is the volume of unstrained lattice, $E(V_0, 0)$ is the corresponding total energy, and C_{ij} are the second order elastic constants. C_{ijk} and C_{ijkl} represent third and fourth-order elastic constants, respectively. The elastic constants are identified as being proportional to the coefficient of the quadratic term in δ (in the polynomial fit to the total energy as a function of the strain parameter). For an arbitrary crystal there are at most 21 independent C_{ij} can be seen in Table 3.1.

Symmetry arguments reduce this number to three for the most uniform crystal type, which is cubic.

2.2.4 Voigt Notation

Voigt notation [6] is a way to define the symmetric tensor by reducing its order. It enables 81 components with fourth-order stiffness tensors to be simplified to 21 independent components. Nye notation [3] has been used up to this point in the thesis. Equation (2.22) uses Voigt notation for the triclinic structure, the most general crystal structure. Voigt notation replaces 11, 22, 33, 23, 31 and 12 with 1, 2, 3, 4, 5, and 6, respectively.

tensor notation	11	22	33	23,32	31,13	12,21
matrix notation	1	2	3	4	5	6

Equation (2.15) can be written as the following using Voigt notation:

$$\begin{bmatrix}\sigma_1\\ \sigma_2\\ \sigma_3\\ \sigma_4\\ \sigma_5\\ \sigma_6\end{bmatrix} = \begin{bmatrix} C_{11} & C_{12} & C_{13} & C_{14} & C_{15} & C_{16} \\ & C_{22} & C_{23} & C_{24} & C_{25} & C_{26} \\ & & C_{33} & C_{34} & C_{34} & C_{36} \\ & & & C_{44} & C_{44} & C_{46} \\ & & & & C_{55} & C_{56} \\ & & & & & C_{66} \end{bmatrix} \begin{bmatrix}\varepsilon_1\\ \varepsilon_2\\ \varepsilon_3\\ \varepsilon_4\\ \varepsilon_5\\ \varepsilon_6\end{bmatrix} \tag{2.22}$$

To understand this better, the elastic behavior and Voigt notation of a cubic crystal are described by three independent elastic constants, namely isotropic-volumetric strain C_{11} in Figure 2.10(a), tetragonal-strain C_{12} in Figure 2.10(b), and pure-shear strain C_{44} in Figure 2.10(c).

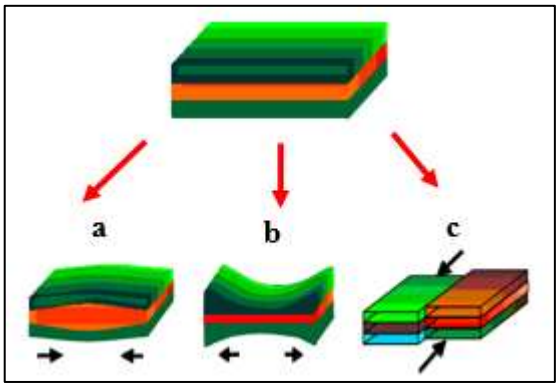


Figure 2.10 The elastic behavior of cubic crystal

In order to obtain these three elastic coefficients, appropriate strain tensors that will solve for these three elastic constants were chosen. Isotropic-volumetric C1 (a), tetragonal-strain C2 (b), and pure-shear strains C3 (c) are given below respectively.

$$C1 = \begin{pmatrix} \delta & 0 & 0 \\ 0 & \delta & 0 \\ 0 & 0 & \delta \end{pmatrix} \tag{2.23}$$

$$C2 = \begin{pmatrix} \delta & 0 & 0 \\ 0 & -\delta & 0 \\ 0 & 0 & \frac{\delta^2}{1-\delta^2} \end{pmatrix} \tag{2.24}$$

$$C3 = \begin{pmatrix} \frac{\delta^2}{1-\delta^2} & 0 & 0 \\ 0 & 0 & 0 \\ 0 & 0 & \delta \end{pmatrix} \tag{2.25}$$

The number of elastic constants describe the elastic response of a crystal depends on its symmetry. While cubic crystals can be identify just three elastic coefficients C_{11}, C_{12} and C_{44}, the tetragonal crsytals required- six independent elastic coefficient because of their lower symmetry propeties. As an example, Equation (2.26) shows the elastic stiffness coefficients for the tetragonal structure 422, 4mm, -42/m, 4/mmm space groups.

$$C = \begin{pmatrix} C_{11} & C_{12} & C_{13} & 0 & 0 & 0 \\ C_{12} & C_{11} & C_{13} & 0 & 0 & 0 \\ C_{13} & C_{13} & C_{33} & 0 & 0 & 0 \\ 0 & 0 & 0 & C_{44} & 0 & 0 \\ 0 & 0 & 0 & 0 & C_{44} & 0 \\ 0 & 0 & 0 & 0 & 0 & C_{66} \end{pmatrix} \tag{2.26}$$

The inverse of the elastic stiffness tensor is given as the elastic compliance tensor in Equation 2.17. The elastic compliance tensor is a $6x6$ matrix and the fourth-rank tensor S_{ijkl}. There is a relation between the elastic stiffness tensor and the elastic compliance tensor given as

$$S_{11} = \frac{C_{11}+C_{12}}{(C_{11}-C_{12})(C_{11}+2C_{12})} \tag{2.27}$$

$$S_{12} = \frac{-C_{12}}{(C_{11}-C_{12})(C_{11}+2C_{12})} \tag{2.28}$$

$$S_{44} = \frac{1}{C_{44}} \tag{2.29}$$

2.3 Theory of Piezoelectric Properties

"We have found a new method for the development of polar electricity, consisting in subjecting them to variations in pressure along their hemihedral axes."

Pierre and Jacques Curie

In this chapter of the thesis, the focus on the qualitative description of the piezoelectric effect. Basic information about piezoelectricity has already been given in the first chapter of the thesis. It was just a brief description, and it did not deeply explain the whole picture of piezoelectricity. The purpose of this chapter is to extend the theoretical description of the piezoelectricity of matter to its elastic and dielectric components [60-65].

Because the main mechanical parameters of interest in piezoelectric materials are elastic compliance and elastic stiffness constants, these two constants are explained theoretically, and then the explanation continues with the direct and converse piezoelectric constants.

2.3.1 Theoretical Background

The direct piezoelectric polarization effect can be defined as the change of electric polarization according to the strain. If external mechanical stress is applied to the material, dielectric displacement will occur. This displacement is the evidence for internal electric polarization.

The phenomenological theory of piezoelectricity was done mainly by Waldemar Voight in 1890. He published the first comprehensive understanding of piezoelectricity and formulated the theory of thermodynamic potentials for piezoelectricity.

The mathematical description of piezoelectricity has two main parts. One part is the converse piezoelectric effect and relates to the strain on the electrical field. The other is the direct piezoelectric effect and relates to stress-displacement. Both of these are depicted in Figure 2.11. The Heckmann diagram shows the relationship between the electrical and the mechanical properties of solids [66-68].

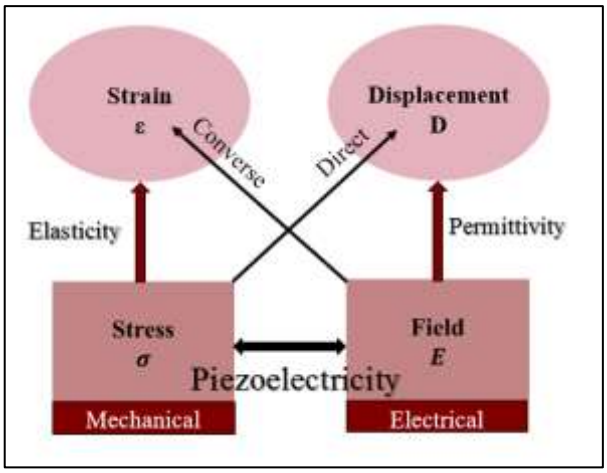


Figure 2.11 Part of Heckmann diagram

As the piezoelectric coefficients can be calculated with the DFT using the Berry-phase approach, the modern polarization method can also be used to evaluate the piezoelectric coefficients.

2.3.2 The Piezoelectric Effect

Piezoelectricity is a linear interaction between converting mechanical and electrical energy in the non-centro symmetric crystals or similar structures. Basically, the piezoelectric effect comes from the change of polarization upon a mechanical deformation. The reason for this polarization is an alteration between positively and negatively charged ion positions in the lattice.

2.3.3 Direct and Converse Piezoelectric Constants

The piezoelectric tensor is a third-rank tensor that represents the relationship between stress and the applied electrical field in the mathematical description. These piezoelectric materials have the ability to convert electrical energy to mechanical energy or vice versa. These two piezoelectric coefficients are defined as the direct (e_{ijk}) piezoelectric coefficient measured in C/m^2 and the converse (d_{ijk}) piezoelectric coefficient measured in C/N.

$$e_{ijk} = \left(\frac{\partial P_i}{\partial \varepsilon_{jk}}\right)_{E,T} = -\left(\frac{\partial \sigma_{jk}}{\partial E_i}\right)_{\varepsilon,T} \tag{2.30}$$

$$d_{ijk} = \left(\frac{\partial P_i}{\partial \sigma_{jk}}\right)_{E,T} = \left(\frac{\partial \varepsilon_{jk}}{\partial E_i}\right)_{\sigma,T} \tag{2.31}$$

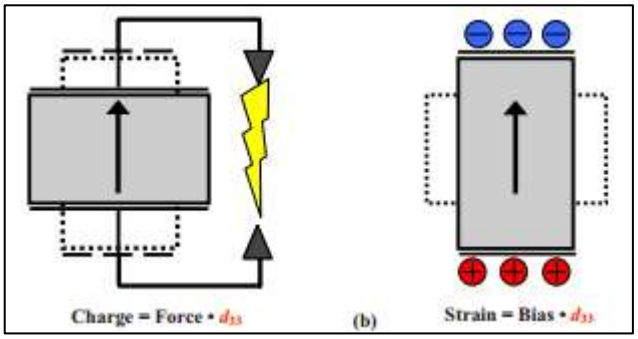


Figure 2.12 Schematic showing the (a) direct and (b) converse piezoelectric effect

For simplicity, some authors in literature use the Voigt notation, which is $e_{ijk} = e_{in}$, when $n = 1,2,3$ and $2e_{ijk} = e_{in}$, when $n = 4,5,6$. The piezoelectric tensors are the sum of the ionic "relaxed-ion" and electronic "clamped-ion" contributions where $e_{in} = e_{in}^{ionic} + e_{in}^{electronic}$ is evaluated because of relative displacements of differently charged sublattice (relaxed-ion) and vanishing internal strain (clamped-ion) [69].

The piezoelectric coefficient e can be calculated within the DFT using the Berry - phase approach or DFPT with the VASP program. The Berry-phase approach was suggested by Bernardini, Fiorentini, and Vanderbilt in 1984. Because the polarization is closely related to the Berry-phase approach, this approach needs to be described first. In the 1990s, a new theoretical approach involving formal quantities such as the Berry-phase quantity was realized and is known by its more familiar term "modern theory of polarization." The method focuses on how the polarization occurs in the material when strain is applied.

The total polarization P is given by

$$P = P^{eq} + \delta P \tag{2.32}$$

In this equation, P^{eq} is the polarization of the equilibrium structure, and δP refers to the piezoelectric polarization. The part is given as

$$\delta P_i = \sum_j e_{ij} \varepsilon_j \tag{2.33}$$

where e_{ij} is the direct piezoelectric coefficient, and ε_j is the strain component.

The stress is specified by a second-rank tensor with nine components, while the polarization is specified by only three components as

$$P_1 = d_{111}\sigma_{11} + d_{112}\sigma_{12} + d_{113}\sigma_{13} + \sigma_{21} + d_{122}\sigma_{22} + d_{123}\sigma_{23} + +d_{131}\sigma_{31} + d_{132}\sigma_{32} + d_{133}\sigma_{33} \quad (2.34)$$

where the d's are the converse piezoelectric coefficients leaving two more polarization componentsP_2 and P_3. The total polarization can be formulated as

$$P_i = d_{ijk}\sigma_{jk} \quad (2.35)$$

At the same time, polarization can be formulated by

$$\delta P_i = \sum_j d_{ij}\sigma_j \quad (2.36)$$

The stresses and strains of the material inside a continuous elastic material are connected by a linear relationship that is mathematically similar to Hooke's spring law.

$$\frac{\sum_j d_{ij}\sigma_j}{\varepsilon_j} = \frac{\sum_j e_{ij}\varepsilon_j}{\varepsilon_j} \quad (2.37)$$

$$e_{ij} = \sum_k d_{ik}C_{kj} \quad (2.38)$$

When the symmetric properties of the tetragonal ABO_3 perovskite structure are taken in consideration, only three different piezoelectric coefficients are found being e_{33}, e_{31}, and e_{15}. The tetragonal form of ABO_3 perovskite structures has at standard growth in z-direction. Any kind of distortion of the structure will be in this direction. Therefore, the δP_3 part of the polarization needs to be described.

$$\delta P_3 = e_{33}\varepsilon_3 + e_{31}(\varepsilon_1 + \varepsilon_2) \quad (2.39)$$

where ε_3 is the strain in the z-direction, while ε_1 and ε_2 are the in-plane strain. The strain components can be changed with

$$\varepsilon_3 = \frac{c-c_0}{c_0} \quad (2.40)$$

And ε_1 and ε_2 are assumed to be isotropic.

$$\varepsilon_1 = \varepsilon_2 = \frac{a-a_0}{a_0} \quad (2.41)$$

The piezoelectric coefficients can be calculated using the following relations

$$e_{33} = c_0 \frac{\partial P_3}{\partial c} + \frac{4ec_0}{\sqrt{3}a_0^2} Z^* \frac{du}{dc} \tag{2.42}$$

and

$$e_{31} = \frac{a_0}{2} \frac{\partial P_3}{\partial a} + \frac{2e}{\sqrt{3}a_0} Z^* \frac{du}{da} \tag{2.43}$$

These first terms of the equations are consist of the "clamped-ion" contribution of the piezoelectric coefficients that represent the effect of strain on the electron structure. The second terms of the equations are the "relaxed-ion" contribution of the piezoelectric coefficients. They are related to the effects of internal strain caused by polarization. To calculate the piezoelectric coefficients, the structure needs to be distorted according to its standard growth direction.

Because polarization is not a bulk property, the calculation of polarization is not straight forward. It implies that it is dependent on the shape of the sample. The converse piezoelectric coefficient d_{ij} can be directly obtained from experimentation, but the direct piezoelectric coefficient e_{ij} can only be obtained theoretically. In this thesis, these theoretical calculations are covered. In order to compare with the literature in various experimental areas, converting e_{ij} to d_{ij} is useful. The relation between the direct piezoelectric coefficient and converse piezoelectric coefficient for tetragonal structure is given by

$$d_{31} = \frac{C_{33}e_{31} - C_{13}e_{33}}{(C_{11}+C_{12})C_{33} - 2C_{13}^2} \tag{2.44}$$

$$d_{33} = \frac{(C_{11}+C_{12})e_{33} - C_{13}e_{31}}{(C_{11}+C_{12})C_{33} - 2C_{13}^2} \tag{2.45}$$

$$d_{15} = \frac{e_{15}}{2C_{55}} \tag{2.46}$$

Studying these three coefficients C_{33}, e_{33}, and d_{33} is the good starting point to find other piezoelectric alloys. The differences in these alloys can be easily found at a lower computational cost.

On the contrary, the piezoelectric e_{ij} cannot be directly obtained experimentally, but d_{ij} can. Therefore, it is useful to convert e_{ij} to d_{ij}.

2.3.4 Number of Independent Piezoelectric Coefficients

The number of a third-rank tensor has $3^3 = 27$ independent components. The three layers

of piezoelectric coefficients are:

$$\begin{matrix} d_{111} & d_{112} & d_{113} \\ \boldsymbol{d_{121}} & d_{122} & d_{123} \\ \boldsymbol{d_{131}} & \boldsymbol{d_{132}} & d_{133} \end{matrix} \quad 1.\,layer \tag{2.47}$$

$$\begin{matrix} d_{211} & d_{212} & d_{213} \\ \boldsymbol{d_{221}} & d_{222} & d_{223} \\ \boldsymbol{d_{231}} & \boldsymbol{d_{232}} & d_{233} \end{matrix} \quad 2.\,layer \tag{2.48}$$

$$\begin{matrix} d_{311} & d_{312} & d_{313} \\ \boldsymbol{d_{321}} & d_{322} & d_{323} \\ \boldsymbol{d_{331}} & \boldsymbol{d_{332}} & d_{333} \end{matrix} \quad 3.\,layer \tag{2.49}$$

The bolded components in Equation 2.47, 2.48 and 2.49 are eliminated by symmetry leaving 18 independent d_{ijk}. The matrix notation of all equations is shown in full tensor notation. For simplicity, the number of suffixes is reduced as much as possible. It is done with the new symbols as shown below.

$$\begin{matrix} d_{11} & \frac{1}{2}d_{16} & \frac{1}{2}d_{15} \\ 0 & d_{12} & \frac{1}{2}d_{14} \\ 0 & 0 & d_{13} \end{matrix} \quad 1.\,layer \tag{2.50}$$

$$\begin{matrix} d_{21} & \frac{1}{2}d_{26} & \frac{1}{2}d_{25} \\ 0 & d_{22} & \frac{1}{2}d_{24} \\ 0 & 0 & d_{23} \end{matrix} \quad 2.\,layer \tag{2.51}$$

$$\begin{matrix} d_{31} & \frac{1}{2}d_{36} & \frac{1}{2}d_{35} \\ 0 & d_{32} & \frac{1}{2}d_{34} \\ 0 & 0 & d_{33} \end{matrix} \quad 3.\,layer \tag{2.52}$$

Tensor notation is replaced by the matrix notation according to Voight notation as 11, 22, 33, 23, 31, and 12 are replaced with 1, 2, 3, 4, 5 and 6, respectively. The array of d_{ij} can be written with

$$\begin{matrix} d_{11} & d_{12} & d_{13} & d_{14} & d_{15} & d_{16} \\ d_{21} & d_{22} & d_{23} & d_{24} & d_{25} & d_{26} \\ d_{31} & d_{32} & d_{33} & d_{34} & d_{35} & d_{36} \end{matrix} \tag{2.53}$$

The number of independent piezoelectric coefficients depends on the level of symmetry of the crystal structure. In this thesis, the tetragonal form of ceramic oxides, namely perovskite materials, is of particular interest. For the tetragonal structure (Class $4mm$),

the piezoelectric matrix notation can be written in terms of three independent piezoelectric coefficients.

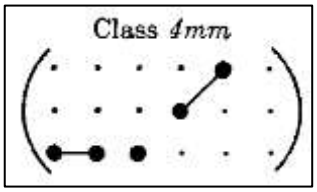


Figure 2.13 Form of the d_{ijk} matrix for tetragonal from and 4mm class

2.3.5 Piezoelectricity of ABO_3 type Perovskite Structures

The reason for piezoelectricity in all kinds of pure piezoelectric materials and their corresponding alloy forms, which are not widely studied as tetragonal forms, is explained next.

A wide range of ABO_3 type perovskite structures adopts a cubic perovskite structure. It crystallizes into the cubic unit cell with five atoms, in which the A-atom is at the corner of the cube, the B-atom is at the center, and the oxygen atoms are located at the center of the faces. Usually, the cation displacement from the oxygen cage center causes a deviation from the cubic symmetry that is related to the properties of substituted A and B atoms. The cubic form of perovskite structures does not show any piezoelectric effects because of the high level of symmetry [70-75].

The A-site of the ABO_3 type perovskite structure is usually occupied by a rare earth or alkali earth metal cation, whereas the B-site is occupied by a transition metal cation. New types of material have been modeled to replace these occupied spaces of the A-site and B-site with two different chemical species. According to the literature, different choices of A-site and B-site atoms can dramatically vary the structure and the properties.

Now, the reason for piezoelectricity of in ABO_3 type perovskite structures is laid out.

2.3.6 $BaTiO_3$

$BaTiO_3$ is the most widely used ferroelectric material since its discovery in 1941 during World War II. At first, reports showed that $BaTiO_3$ was based on doping studies of TiO_2 and BaO. Right after the discovery of $BaTiO_3$, ceramic materials have been widely used in capacitors and in various types of transducing technology.

The basic structure of barium titanate is where the titanium (Ti) atom occupies the octahedrally coordinated site, and the barium (Ba) atom occupies the twelve coordinated sites in a high temperature $Pm3m$ cubic symmetry. The tetragonal phase shifts the oxygen and titanium atoms to produce a spontaneous polarization. The origin of the ferroelectric property comes from a displacement of the Ti atoms in the z-direction. The polarization direction of $BaTiO_3$ has three different directions which are [001], [011], and [111].

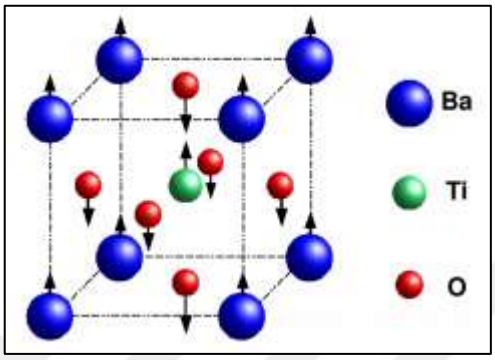


Figure 2.14 Displacement of atoms in tetragonal phase of $BaTiO_3$

Barium titanate (BaTiO3) is a potential lead-free source of piezoelectric crystals for low temperature and room temperature applications.

2.3.7 $SrTiO_3$

SrTiO3 is used as an insulator that has a perovskite and paraelectric structure at room temperature. The Ti^{+4} atom is six fold and is coordinated by O^{-2}, whereas each Sr^{+2}ion is surrounded by four TiO_6 octahedra. Sr^{+2} and O^{-2} ions exhibit the ionic bonding character. Within the TiO_6 octahedra, a hybridization of the $O-2p$ states and the $Ti-3d$ states lead to pronounced covalent bonding. $SrTiO_3$ has a unique structure because of mixed ionic-covalent bonding properties.

The reason for piezoelectricity is based on octahedral tilting of the oxygen atoms. Octahedral tilting is classified by its different possible combinations. This classification is reported by Glazer according to octahedral tilting around the each axis. Basically, this classification is in-plane and out-of-plane. In-plane is where each oxygen octahedral rotates in the same direction along one axis. Out-of-plane is where each oxygen octahedral rotates in the opposite direction along one axis.

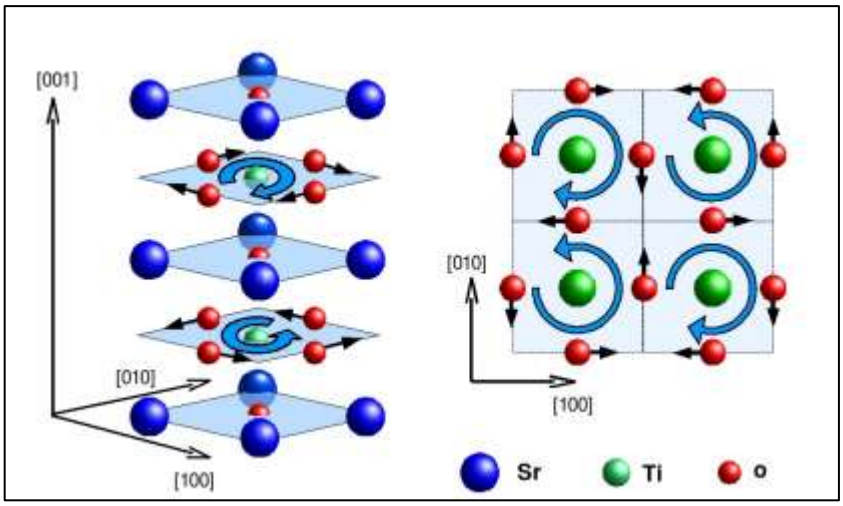


Figure 2.15 Displacement of atoms in tetragonal phase of $SrTiO_3$

2.3.8 $PbTiO_3$

Lead titanate ($PbTiO_3$) can be a great ceramic as it is a stable piezoelectric material for high temperature and high frequency applications. Because of high Curie temperature, high pyroelectric coefficients, low dielectric constants, and high spontaneous polarization, it can be considered to be one of the most important members of the perovskite family. Tetragonality of the unit cell, c/a is the highest among the other perovskite structure.

However, beacuse Pb-based materials have high piezoelectric coefficients, they affect the environment and human health. Lead-free piezoelectric materials have recently gained attention due to their environmentally safe property. $PbTiO_3$ has also been extensively used in a range of piezoelectric applications, the best known being $PbZr_{(x)}Ti_{(1-x)}O_3$. PZT is a ferroelectric and piezoelectric material with very high longitudinal piezoelectric coefficients (d_{33}). Due to the technological developments in science over the last century, a more rational design for various materials has become possible. Especially, computer simulations of materials that enable the design of new materials with desired properties. For that reason, ceramic oxides will be focus in the upcoming part of this chapter. Namely, they consist of perovskite materials that are of the tetragonal pure form such as $BaTiO_3$, $SrTiO_3$, $PbTiO_3$, $BaZrO_3$, $SrZrO_3$, and $PbZrO_3$, and also their tetragonal alloy form.

2.3.9 The Modes of Piezoelectric Coefficients

The tetragonal perovskite structures from the ceramic oxides family are polarized into three different polarization states. Longitudinal (d_{33}), transverse (d_{31}), and shear (d_{15}) piezoelectric coefficients are investigated. The piezoelectric coefficient d_{ij} is defined as the electric displacement induced by applied stress. When the stress and the electric displacement are in the poling direction, the coefficient is known as the longitudinal piezoelectric coefficient d_{33}. If the stress is applied along the length of the crystal and the electric displacement is induced in the thickness direction, then it is called the transverse piezoelectric coefficient d_{31}. The largest electromechanical coupling comes from the shear mode in the perovskite structure because of the easy rotation of the oxygen octahedron [76]. Figure 2.16 shows the schematic of piezoelectricity that depends on the different modes of crystal orientation.

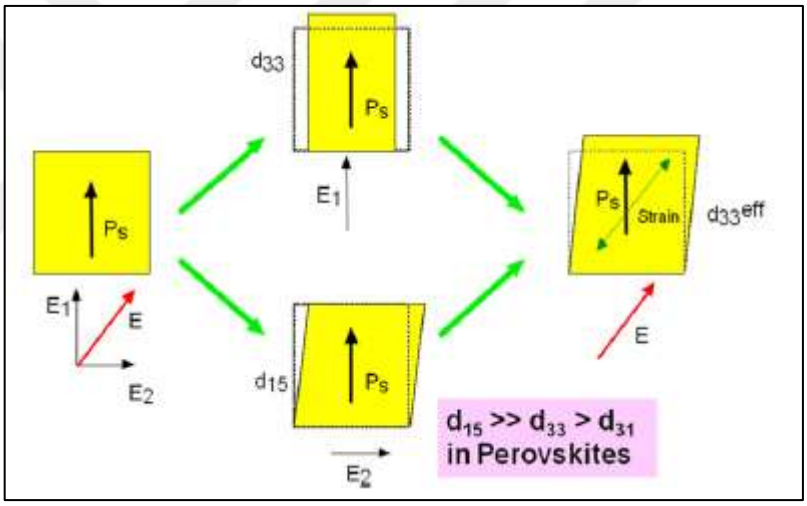


Figure 2.16 Schematic of modes of piezoelectricity that depends on the crystal orientation

CHAPTER 3

MECHANICAL PROPERTIES OF ABO_3 PEROVSKITES AND THEIR ALLOYS

3.1. Introduction

This chapter will cover first-principle calculations based on the DFT to reach the ground state structural and elastic properties of various ABO_3 type ceramics and their $\{A_xA'_{(1-x)}\}BO_3$ and $A\{B_xB'_{(1-x)}\}O_3$ alloys. To represent alloy perovskites, supercells were employed with species A, A′=Ba, Sr, Pb; B, B′=Ti, Zr. The effects of composition and atomic configuration/order on lattice structure, thermodynamics and elastic constants were evaluated. In calculations, the linear response method (LRT) as well as homogeneous field method were used and provided an assessment of the performance of these approaches to determine the aforementioned properties. ABO_3 type pure perovskite crystals have been studied intensively; however, the structural, elastic, dielectric, and piezoelectric properties of their alloys are still a subject of discussion [47-54]. The effects of composition and atomic configuration/order on lattice structure, thermodynamics and elastic constants were evaluated by LRT and homogenous field method. The aim of this chapter, while providing comprehensive data for pure ABO_3 compounds for various existing polymorphs, is also to investigate the effects of alloying (concentration and structural/chemical anisotropy) on thermodynamic, structural and mechanical properties for a broad concentration range. $\{A_xA'_{1-x}\}BO_3$ and $A\{B_xB'_{1-x}\}O_3$ alloys have been constructed for which x is varied from 0 to 1 with species A, A′=Ba, Sr, Pb; B, B′=Ti, Zr. The effects of the A-atom site and the B-atom site have shown the identifying properties of those alloys such as structural properties and elastic constants.

3.2. Methodology

3.2.1 Construction of Alloys

The prototype ABO_3 type perovskite structure has a space group of $Pm\bar{3}m$ (No: 225) with the ratio of $1:1:3$. The basic pure perovskite structure is modeled with five atoms in a unit cell, in which the A-site is occupied by an element, B-site by another element, and O-sites by oxygen. Ba, Sr, and Pb are considered for atoms in the A-sites, whereas Ti and Zr are considered for atoms in the B-sites. The crystal unit cell is not enough to simulate the alloy's properties. In practice, this can be modeled with a supercell of several unit cells. With a different type of atom occupying the structure, the supercell approach calculates structural and mechanical properties of the ABO_3 type perovskite structures. In order to carry out calculations using periodic boundary conditions, supercells are constructed with a different type of to achieve the desired concentration x to produce the alloy of interest. Since the larger system needs more computational resources, the simulation is kept as small as possible. A supercell with periodic boundary conditions is chosen that contain 40 atoms represented by $2x2x2$ perovskite units for the creation of $\{A_xA'_{(1-x)}\}BO_3$ and $A\{B_xB'_{(1-x)}\}O_3$ alloys in which the crystallographic site is occupied by different atoms. These alloys are studied throughout the $x = 1 - 0$ A-site and B-site concentration. This supercell is modeled at different values of $x = 0.875, 0.75, 0.625, 0.5, 0.375, 0.25, 0.125$. Chemical order problems were encountered during all calculations. The calculations do not only model a statistical occupation of crystallographic sites, but it also analyses the symmetry problem. The eight A and A′ atoms and the eight B and B′ atoms are situated on a simple cubic sublattice. $\{A_xA'_{(1-x)}\}BO_3$ and $A\{B_xB'_{(1-x)}\}O_3$ alloys can be classified as homovalent and heterovalent alloys from the chemical perspective. Homovalent alloys are defined as A-atoms and belong to same column on the periodic table, while heterovalent alloys belong to a different column on the periodic table [55].

To the best of scientific knowledge, there are no reports on structure-property relationships in A-site and B-site mixed perovskites for these compounds. All possible local chemical ordering of A and B-ions and their influence on the mixing energy were investigated by first- principles calculations based on the DFT. The number of crystallographic sites was altered from one to eight with different stoichiometric ratios [45]. The 0.125:0.875 stoichiometric ratio of A and A' in $\{A_xA'_{(1-x)}\}BO_3$ has a minimum

energy without any position limit due to the unchanging symmetry of the structure. The 0.25:0.75 ratio in the two crystallographic sites, which are occupied by different atoms, can break down the symmetry. It has been shown that minimum energy changed with different configurations when atoms were placed at the corners and surface positions due to a slight change in symmetry. All possible configurations for each stoichiometric ratio have been developed, and the symmetry equivalent ones were used as shown in Figure 3.1.

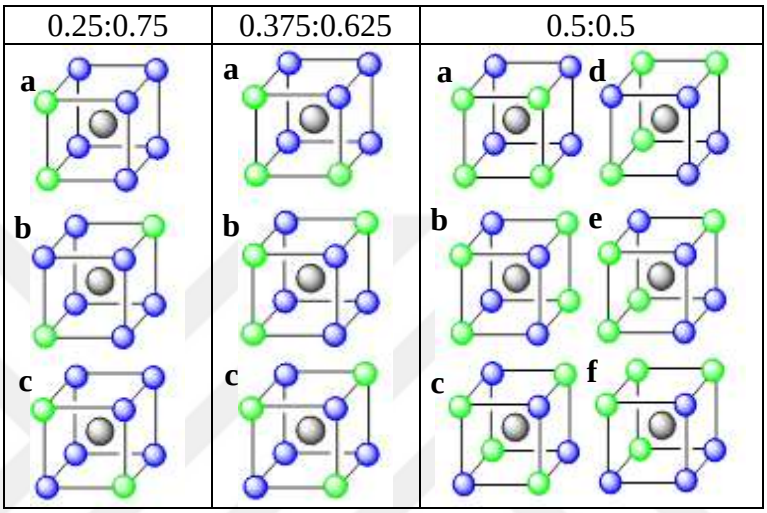


Figure 3.1 All possible arrangements for 2x2x2 supercell used in different concentration

The lattice parameters of the 40- atom super cells were established according to Vegard's law. According to Vegard's law, the lattice parameters of $PbZr_xTi_{1-x}O_3$ alloys can be calculated by the following formula:

$$a_{PbZr_xTi_{1-x}O_3} = x\, a_{PbZrO_3} + (1-x) a_{PbTiO_3} \tag{3.1}$$

where a_{PbZrO_3} and a_{PbTiO_3} are the lattice constants of $PbZrO_3$ and $PbTiO_3$ compounds in the equilibrium, respectively. Different types of cations replace another element on the same crystallographic site. The replacement of differing type cations can be composed for a chemical ordering that can disrupt the symmetry. In turn, the structure influences the energetic, mechanical, dielectric, also small piezoelectric properties. Preferred structural motifs are shown, reason for the preference is analyzed, and mixing energies of the alloys are investigated. Thus, it has been shown how to assess the alloy forms and are modeled at the optimum structure. The $0.125:0.875$ and $0.250:0.750$ stoichiometric ratios with three different configurations of Zr-Ti placement are shown in $2x2x2$ supercells as an example of $Pb_8Zr_xTi_{8-x}O_{24}$ in Figure 3.2. The black spheres in this figure

represent Pb atoms (A-site), the green spheres represent Zr atoms (B-site), the blue spheres represent Ti atoms (B′-site), and the red spheres represent O atoms. The crystal structure of alloys is visualized using the program VESTA .

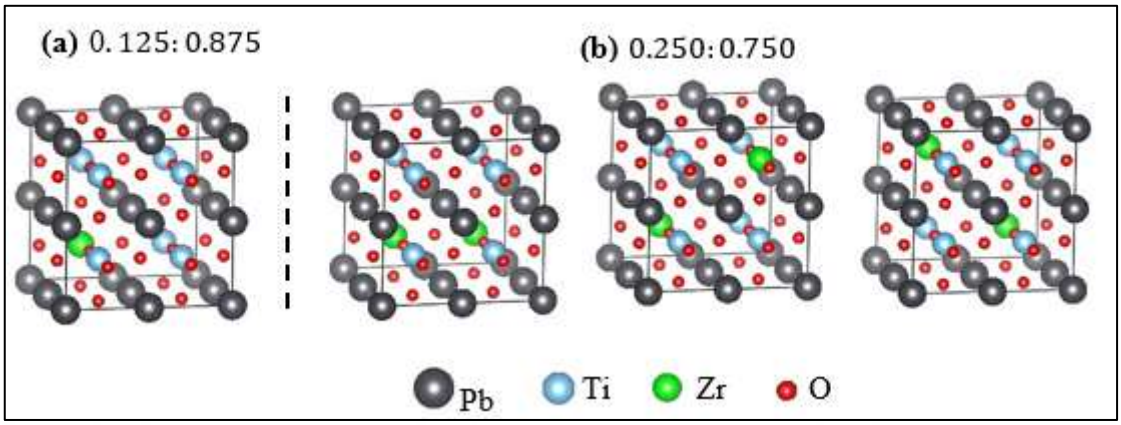


Figure 3.2 40 atoms in $Pb_8Zr_xTi_{8-x}O_{24}$ cell with (a) 0.125:0.875and (b) 0.25:0.75 stoichiometric ratio

3.2.2 Mechanical Properties of $BaTiO_3$ polymorphs

3.3 Results and Discussion

3.3.1 Pre-requirements

Before calculating mechanical properties, the following rules to determine elastic constants were obeyed.

For each strain type, these rules were applied:

- Determine the appropriate strain tensor which strain the primitive lattice vector for several strain values
- Use the DFT code to calculate the total energy of the system for each strained crystal structure
- Fit the strain versus energy data to the Birch-Murnaghan equation and exact the related elastic constants.

Before the elastic constants of the cubic and tetragonal $BaTiO_3$ can be entired, the crystal structure needs to be defined as cubic, tetragonal, orthorhombic or rhombohedra. As mentoined, the most important step is create the position file which is called POSCAR.

The geometrical optimization is the most criticial issue at beginning of first-principle calculations. It fundamentally depends on find to minimum energy at equilibrium. It is

known as the energy minimum principle that equilibrium state has the minimum energy at constant volume and entropy. Without any limitation, all crystals are repeated in the space accordance with periodic boundary conditions. The system that is given all atom positions in the crystal can be identify at ground-state properties. A series of iteration of desired electronic and ionic structures convergerce is continued to find to minimum energy of the system. Thus, the ground state properties are obtained the same way. Lattice parameters, internal parameters, and coordinates of atoms are taken from the experimental results. The crystal is relaxed for finf the position where it has minimum energy. The minimum volume (V_0) is found among increased and decreased volumes at energy-volume (E-V) or pressure-volume (P-V) graphs. The elastic constants are also calculated with the same way.

3.3.2 Position files of $BaTiO_3$ polymorphs

$BaTiO_3$ is a well known ferroelectric among ABO_3 type oxide ceramics. It has been recognized for a long time ago with several scientists. The first calculations are performed on $BaTiO_3$ and its polymorphs due to the results are already detailed in literature. $BaTiO_3$ can easily fabricated and shaped at low price and its piezoelectric constants are many times higher than natural materials, which are family of piezoceramic.

In general, perovskite materials have different structural phases at different temperatures. Perovskite crystals have a cubic structure at high temperatures. They undergo a ferroelectric transition at higher temperatures. When the temperature is lowered, these compounds can undergo different types of polar or non-polar structural phase transitions. For an example, $BaTiO_3$ at 183 K transforms the structure from rhombohedral to orthorhombic, and the polarization direction changes from [111] to [110]. Table 3.1 shows $BaTiO_3$ polymorphs crystal structures [55-58].

In the present work, the lattice parameters and their initial atom coordinates in the structure were taken from previous experimental studies.

Table 3.1 Crystal structure of $BaTiO_3$ polymorphs and their space group

Phase	Atom	Position
Cubic Pm-3m (221)	Ba	(0.0 , 0.0, 0.0)
	Ti	(0.5 , 0.5, 0.5)
	O_1	(0.5 , 0.5, 0.0)
	O_2	(0.5 , 0.0, 0.5)
	O_3	(0.0 , 0.5, 0.5)

Table 3.1 Crystal structure of $BaTiO_3$ polymorphs and their space group (Cont.)

Phase	Atom	Position
Tetragonal P4mm (99)	Ba	(0.0 , 0.0, 0.0)
	Ti	(0.5 , 0.5, 0.5+$\Delta_{T-z}Ti$)
	O_1	(0.5 , 0.5, 0.0+$\Delta_{T-z}O_I$)
	O_2	(0.5 , 0.0, 0.5+$\Delta_{T-z}O_{II}$)
	O_3	(0.0 , 0.5, 0.5+$\Delta_{T-z}O_{II}$))
Orthorhombic Amm2 (38)	Ba	(0.0 , 0.0, 0.0)
	Ba	(0.0 , 0.5, 0.5)
	Ti	(0.5 , 0.0, 0.5+$\Delta_{O-z}Ti$)
	Ti	(0.0 , 0.5, 0.0+$\Delta_{O-z}Ti$)
	O_1	(0.0 , 0.0, 0.5+$\Delta_{O-z}O_I$)
	O_1	(0.5 , 0.0, 0.0+$\Delta_{O-z}O_I$)
	O_2	(0.5, 0.25+$\Delta_{O-y}O_{II}$, 0.25+$\Delta_{O-z}O_{II}$)
	O_2	(0.5, 0.75+$\Delta_{O-y}O_{II}$, 0.75+$\Delta_{O-z}O_{II}$)
	O_2	(0.5, 0.75-$\Delta_{O-y}O_{II}$, 0.25+$\Delta_{O-z}O_{II}$)
	O_2	(0.5, 0.25-$\Delta_{O-y}O_{II}$, 0.75+$\Delta_{O-z}O_{II}$)
Rhombohedra R-3m (160)	Ba	(0.0 , 0.0, 0.0)
	Ti	(0.5+$\Delta_{R-z}Ti$, 0.5+$\Delta_{R-z}Ti$, 0.5+$\Delta_{R-z}Ti$)
	O	(0.5+$\Delta_{R-z}O_{II}$, , 0.5+$\Delta_{R-z}O_{II}$, , 0.0+$\Delta_{R-x}O_{II}$,)
	O	(0.5+$\Delta_{R-z}O_{II}$, , 0.0+$\Delta_{R-x}O_{II}$, , 0.5+$\Delta_{R-z}O_{II}$,)
	O	(0.0+$\Delta_{R-x}O_{II}$, , 0.5+$\Delta_{R-z}O_{II}$, , 0.5+$\Delta_{R-z}O_{II}$,)

3.3.3 Structural Properties of ABO_3 Perovskite Structures

The total calculated energy as a function of the primitive cell volume for ABO_3 is used to determine structural and mechanical properties of the pure system by a least-squares fit of the third-order Birch-Murnaghan equation given by

$$E(V) = E_0 + \frac{9V_0B_0}{16}\left\{\left[\left(\frac{V_0}{V}\right)^{2/3} - 1\right]^3 B_0' + \left[\left(\frac{V_0}{V}\right)^{2/3} - 1\right]^2 \left[6 - 4\left(\frac{V_0}{V}\right)^{2/3}\right]\right\} \quad (3.2)$$

where E_0 is the total energy, V_0 is the equilibrium volume, B_0 is the bulk modulus pressure and B_0' is the first derivative of the bulk modulus with respect to pressure at 0 GPa. All of these are treated as free parameters during the least- squares fitting. The equilibrium lattice parameter a_0 is determined as the parameter that minimizes the total energy [59]. To assess the accuracy of the DFT calculations, the cubic phase of eight perovskite crystals was selected and compared to the calculated lattice parameters and bulk modulus with the available experimental data. In Table 3.2, the parameters obtained after the fitting procedure, the experimental lattice parameters, and bulk modulus are presented. Table

3.2 shows the calculated equilibrium total energy (E_0 in eV), the lattice parameters (a in Å), the bulk modulus (B in GPa), and the pressure derivative of bulk modulus (B′) together with theoretical and available experimental values for pure perovskites together. The errors in the lattice parameters and bulk modulus are less than 2% and 6%, respectively.

Table 3.2 The calculated structural properties for pure perovskites

	Equation of State Parameters							
	E_o(ev)	a(Å)			B(GPa)			B′
			Expt.	Theory		Expt.	Theory	
$BaTiO_3$	-40.21	4.03	4.00[28]	4.00[48]	163	162[28]	172[48]	4.55
$PbTiO_3$	-38.01	3.96	3.97[82]	3.96[50]	176	144[53]	140[50]	4.51
$SrTiO_3$	-40.29	3.94	3.91[57]	3.95[50]	171	174[86]	170[50]	4.42
$BaZrO_3$	-41.67	4.25	4.19[76]	4.21[51]	149	-	157[51]	4.45
$PbZrO_3$	-39.11	4.20	4.13[85]		156			4.39
$SrZrO_3$	-41.23	4.19	4.10[86]	4.17[51]	152	-	160[51]	4.35

3.3.4 Elastic Properties of $BaTiO_3$ Polymorphs

The different methods expressed at the beginning of the chapter are the linear response and homogeneous field methods. LRT is a way of describing a real observable experiment. Basically, this describes what is going on inside the system in response to applied outside influences that are the electric and magnetic fields or the applied pressures and applied driving forces. A macroscopic quantum system in which localized disturbances are created by an applied external force in the neighborhood of some point r at the time t, where the response of the system is then measured at the point r' at the later time t' [97]. The homogeneous field method is the method to calculate the elastic fields inside a spherical inclusion of a radius a with radially varying elastic properties [98].

These two closely related approaches can be used to calculate the elastic constants from first-principle calculations. The first (Linear Response Method) is based on the analysis of the changes of the calculated stress values arising from the variation in the strain, and the second (Homogeneous Field Method) is related to the analysis of the total calculated energy of a crystal as a function of applied strain. In the calculation, these two methods to search for the elastic constants are used. VASP uses the linear response theory in the background in order to get the elastic constants. IBRION and ISIF were set to 3 and 6, respectively, which was simulated in the VASP and compared to the results with the former. IBRION is set to 6 in order to determine the Hessian matrix (matrix of the second

derivatives of the energy with respect to atomic positions) and vibrational frequencies of the system. Only the symmetry inequivalent displacement is taken into consideration. ISIF=3 allows the cell shape and cell volume to change, and it fully relaxes the ions in the solid at zero force and zero pressure. The elastic tensor is determined by performing six finite distortions of the lattice and deriving the elastic constants from the stress-strain relationship. In this way, the calculated elastic constants include both the contributions for distortions with rigid ions and the contributions from the ionic relaxation.

The calculations of the elastic properties of the cubic structure in Figure 3.3 were started, and the tetragonal form ABO_3 type perovskite structure is continued in Figure 3.4. According to the symmetry of the cubic crystal, it is completely described by three independent constants C_{11}, C_{12}, and C_{44} and they are obtained by the three strains (C1, C2, C3) given in Table 3.3. The tetragonal, orthorhombic, and rhombohedral crystals contain 6, 9, and 5 as elastic constants, respectively. In the thesis, the focus is on the cubic and tetragonal structures. To obtain the elastic constants of the cubic and tetragonal forms of $BaTiO_3$, the above strains were applied.

Figure 3.3 and Figure 3.4 are shown the changing in strain energy as a function of strain energy as a function of strain for cubic and tetragonal $BaTiO_3$, respectively. δ is strain parameter and $\delta = 0$ is referred the equilibrium volume V_0 at 0 GPa. The strain parameter is changed from 0.03 to -0.03 in 0.001 steps and the total energies are calculated at every single step. A linear equation is obtained and it is fitted the second-order equation.

Table 3.3 Applied strains ε_i and corresponding energy densities

Strain	Parameters	$E(V,\varepsilon) - E(V_0,0)/V_0$
C1	$\varepsilon_1 = \varepsilon_2 = \varepsilon_3 = \delta$	$3/2(C_{11} + 2C_{12})$
C2	$\varepsilon_1 = \delta, \varepsilon_2 = -\delta, \varepsilon_3 = \delta^2/1 - \delta^2$	$(C_{11} - C_{12})\delta^2$
C3	$\varepsilon_1 = \delta^2/1 - \delta^2, \varepsilon_6 = \delta$	$(2C_{44})\delta^2$
T1	$\varepsilon_3 = \delta^2/1 - \delta^2, \varepsilon_6 = 2\delta$	$(2C_{66})\delta^2$
T2	$\varepsilon_1 = \delta^2/1 - \delta^2, \varepsilon_4 = 2\delta$	$(2C_{44})\delta^2$
T3	$\varepsilon_1 = \delta, \varepsilon_2 = -\delta, \varepsilon_3 = \delta^2/1 - \delta^2$	$(C_{11} - C_{12)}\delta^2$
T4	$\varepsilon_3 = \delta$	$(C_{33}/2)\delta^2$
T5	$\varepsilon_1 = \delta, \varepsilon_2 = \delta, \varepsilon_2 = -\delta^2 - 2\delta/1 - \delta^2$	$(C_{11} + C_{12} + 2C_{33} - 4C_{13})\delta^2$
T6	$\varepsilon_1 = \varepsilon_2 = \varepsilon_3 = \delta$	$(C_{11} + C_{12} + 2C_{13} + 2C_{33}/2)\delta^2$

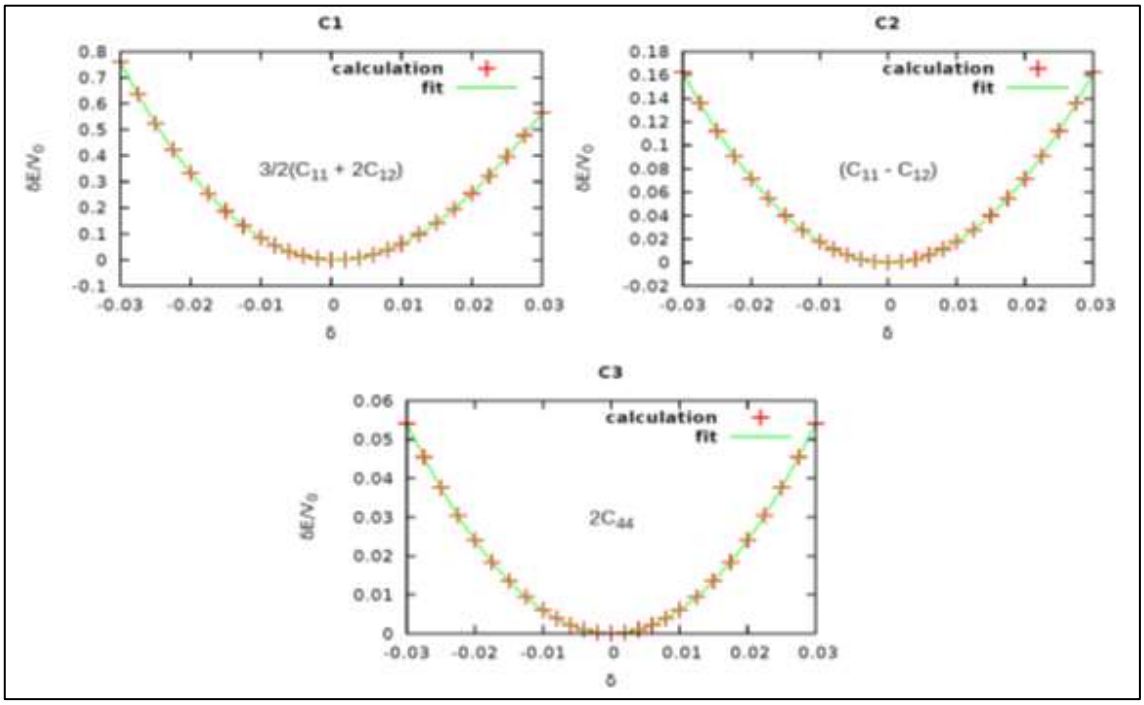


Figure 3.3 Changes in strain energy as a function of strain for cubic $BaTiO_3$

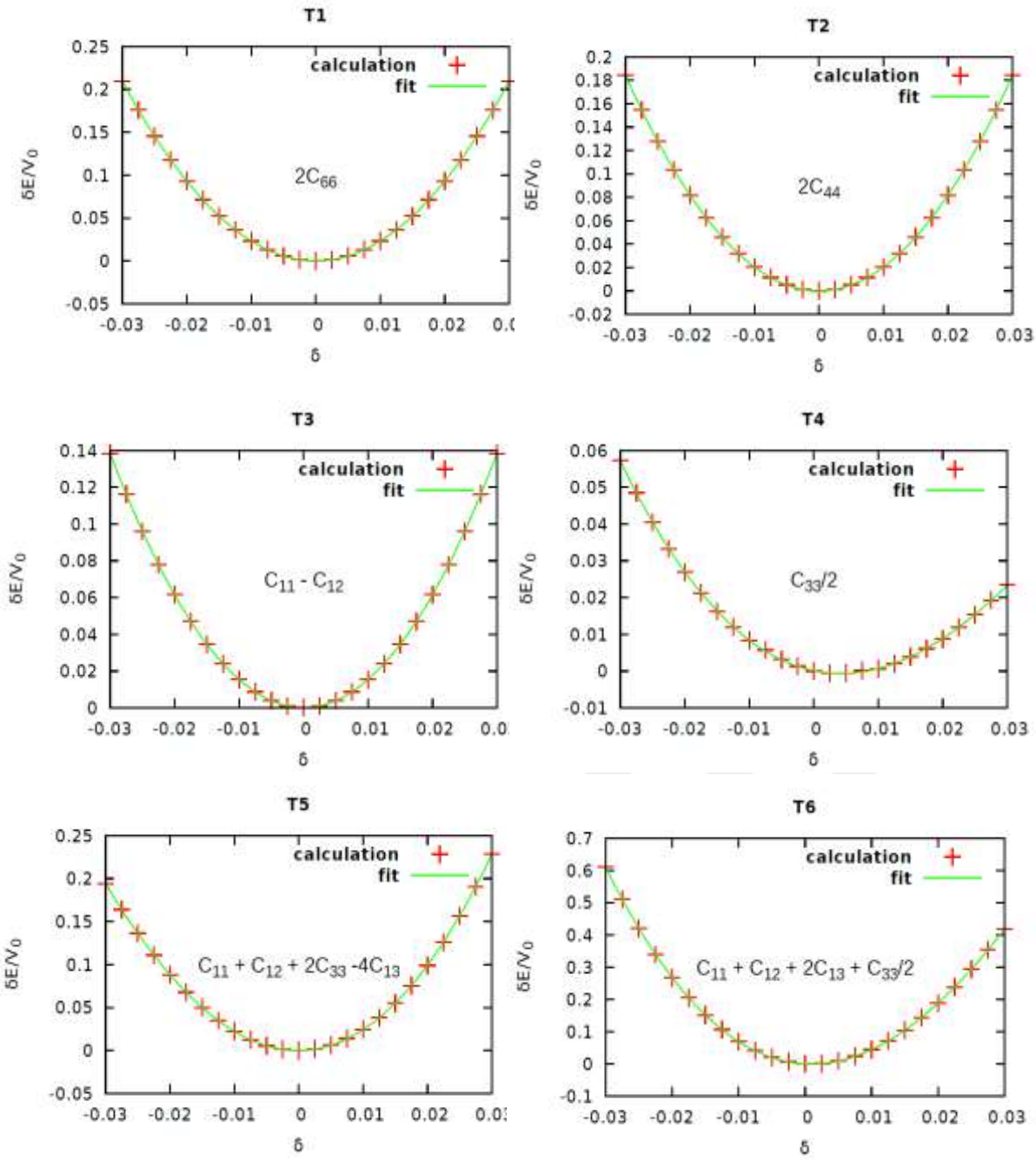


Figure 3.4 Changes in strain energy as a function of strain for tetragonal $BaTiO_3$

$BaTiO_3$ polymorphs ground state and elastic properties are calculated. At the same time, the phase transition of the $BaTiO_3$ polymorphs is shown in Figure 3.5. The volume versus total energy curve demonstrates the phase transition from cubic to tetragonal, tetragonal to orthorhombic, and orthorhombic to rhombohedral. Gibbs free energy can be used to determine the spontoneity of a process by a thermodynamic system at a constant temperature and pressure.

Gibbs free energy can be used to determine the spontoneity of a process by a thermodynamic system at a constant temperature and pressure.

$$G = E + PV - TS$$

Where E, P, V, T, and S are total energy, pressure, volume, temperature and entropy, respectively. DFT calculations are done at zero temperature for ground state. Thus, the Gibbs free energy turned to enthalpy equation. $G = H = E + PV$. The phase transitions on cubic, tetragonal, orthorhombic and rhombohedra are performed volume-total energy (V-E) graph.

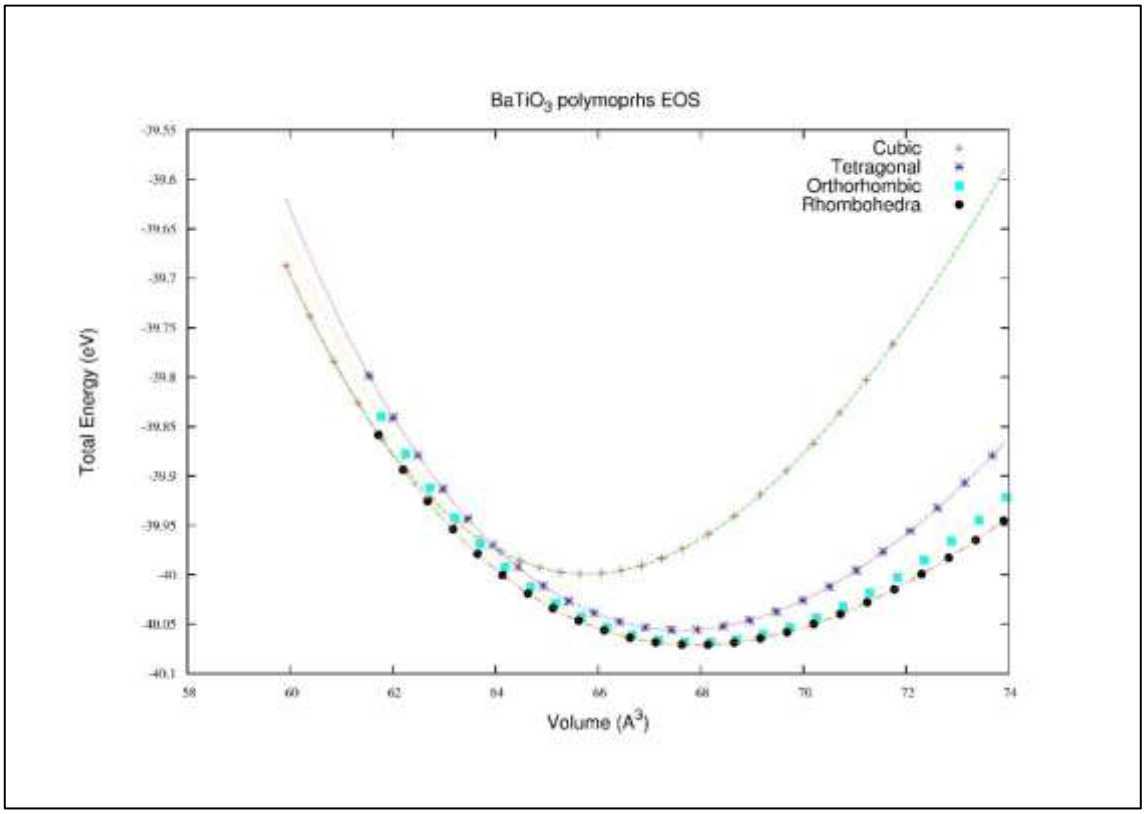


Figure 3.5 Equation of states of BaTiO3 polymorphs

Pristine ABO_3 perovskites have been studied extensively with DFT calculations in the literature. On the other hand, the effects of alloying on the mechanical and structural properties have not been fully researched. Total energy versus volume behavior of different types of $\{A_xA'_{(1-x)}\}BO_3$ and $A\{B_xB'_{(1-x)}\}O_3$ alloys are shown in Figure 3.6. Volume and energy are per single ABO_3 formula unit in all cases. The dashed line Figure 3.6 represents the fitted data to the Birch-Murnaghan equation of different states. For each alloy concentration, the purpose was to find the energetically favorable arrangement. Doped perovskites $\{A_xA'_{(1-x)}\}BO_3$ and $A\{B_xB'_{(1-x)}\}O_3$ have intermediate formation energy between those of the pure forms in accordance to the degree of doping. This behavior supports the idea that the difference between the groups depend on the oxidation states. The calculated equation of state parameters, which are the equilibrium lattice

constants, the equilibrium volume, bulk modulus, the pressure derivative of bulk modulus and cohesive energy for the $PbZrTiO_3$ (PZT) are shown in Table 4.4 as an example. Table 4.4 shows the calculated equilibrium lattice parameters (a in Å), bulk modulus (B in GPa), and the pressure derivative of the bulk modulus (B′) together with the theoretical and available experimental values for the PZT perovskites (a,b,c corresponds to different positions shown in Figure 2.7 at Chapter 2).

Table 3.5 Calculated structural properties of PZT perovskites

		V_0 (Å^3)	B(GPa)	B_0'	Lattice parameter(Å)	c/a
PZT	$Pb_8Zr_7Ti_1O_{24}$	72.60	157.81	4.47	4.170	1.0000
	$Pb_8Zr_6Ti_2O_{24}$[a]	71.22	158.13	4.51	a=c=4.136, b=4.157	1.0052
	$Pb_8Zr_6Ti_2O_{24}$[b]	71.01	160.53	4.45	4.139	1.0000
	$Pb_8Zr_6Ti_2O_{24}$[c]	71.04	159.25	4.53	a=b=4.140, c=4.138	1.0004
	$Pb_8Zr_5Ti_3O_{24}$[a]	69.76	159.25	4.59	a=b=4.122, c=4.099	1.0056
	$Pb_8Zr_5Ti_3O_{24}$[b]	69.54	161.01	4.58	a=c=4.103, b=4.125	1.0054
	$Pb_8Zr_5Ti_3O_{24}$[c]	69.40	162.46	4.50	4.108	1.0000
	$Pb_8Zr_4Ti_4O_{24}$[a]	68.40	160.37	4.61	a=b=4.104, c=4.054	1.0123
	$Pb_8Zr_4Ti_4O_{24}$[b]	67.96	165.34	4.47	a=c=4.063, b=4.112	1.0121
	$Pb_8Zr_4Ti_4O_{24}$[c]	67.67	165.02	4.48	4.073	1.0000
	$Pb_8Zr_4Ti_4O_{24}$[d]	68.19	161.17	4.66	a=c=4.083, b=4.084	1.0003
	$Pb_8Zr_4Ti_4O_{24}$[e]	68.00	163.42	4.53	b=c=4.088, a=4.063	1.0061
	$Pb_8Zr_4Ti_4O_{24}$[f]	68.22	161.65	4.60	4.084	1.0000
	$Pb_8Zr_3Ti_5O_{24}$[a]	66.75	163.58	4.63	a=b=4.064, c=4.037	1.0065
	$Pb_8Zr_3Ti_5O_{24}$[b]	66.52	165.02	4.66	a=c=4.041, b=4.068	1.0068
	$Pb_8Zr_3Ti_5O_{24}$[c]	66.37	167.26	4.54	4.047	1.0000
	$Pb_8Zr_2Ti_6O_{24}$[a]	65.20	167.43	4.60	a=c=4.013, b=4.042	1.0073
	$Pb_8Zr_2Ti_6O_{24}$[b]	64.96	170.63	4.49	4.018	1.0000
	$Pb_8Zr_2Ti_6O_{24}$[c]	65.00	168.06	4.65	a=b=4.019, c=4.020	1.0002
	$Pb_8Zr_1Ti_7O_{24}$	63.56	171.43	4.56	3.989	1.0000

As seen in Table 3.5, when the alloy structures are optimized, depending on where you put the second atoms, the cubic symmetry is broken. In the first one, the second atom shifted one unit cell in each direction on the face (110).

The c/a ratio may be the dominant factor in determining the total polarization. Because it is directly related to determining the total polarization, it is the most important strain effect. As seen in the Table 3.5, this leads to a structure that looks tetragonal; however, this is not exactly tetragonal but the angle between a and b cell vectors changes by 90°. This is neutral. Using the values of ISIF & IBRION for optimization, neutrality is expected. Since the deviation of the angles is so small, it can be considered pseudo-tetragonal. The deviation of angle is approximately $arc\tan(\frac{0.0021}{12.13})$. The results were generated for different concentrations of the various perovskite compounds. The other

alloy's cohesive energies are given in Figure 3.6. The rest of their structural properties have been tabulated in the Supplementary Material.

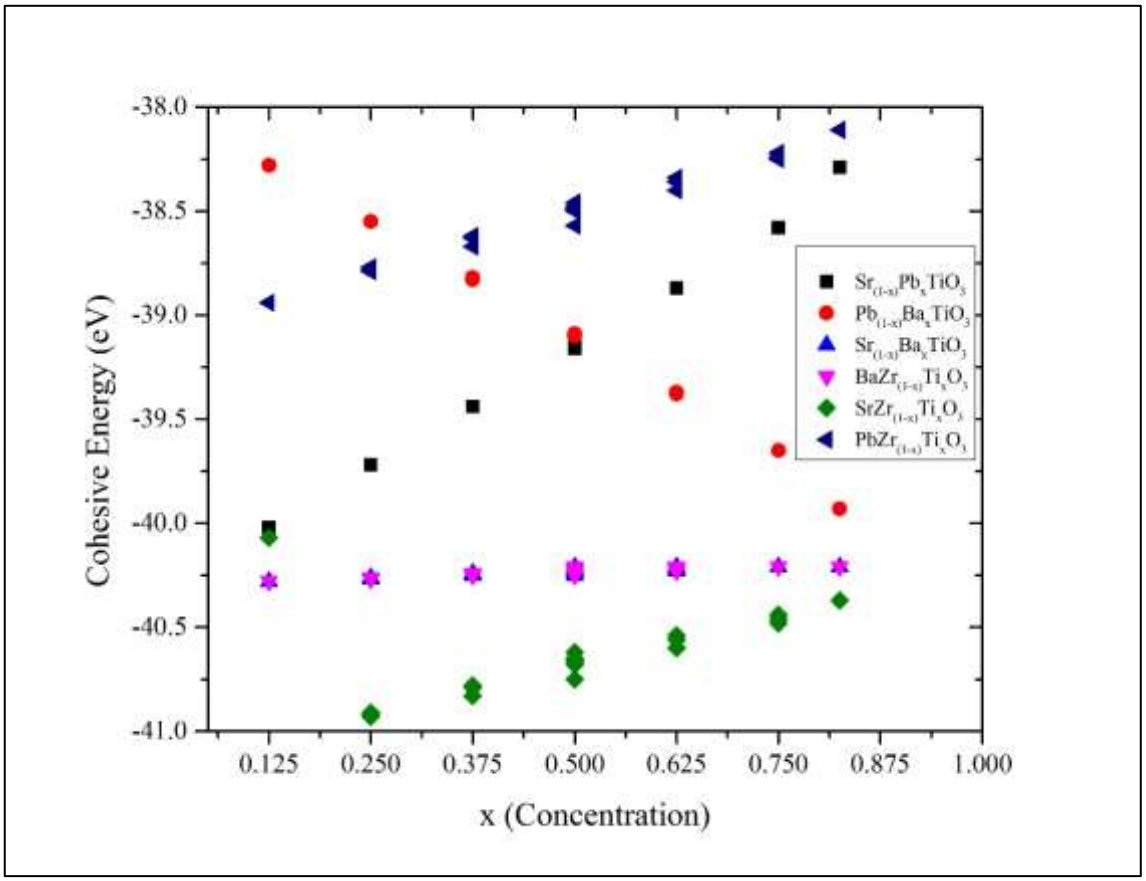


Figure 3.6 Cohesive energies as a function of concentration in SPT, PBT, SBT,PZT, BZT and SZT

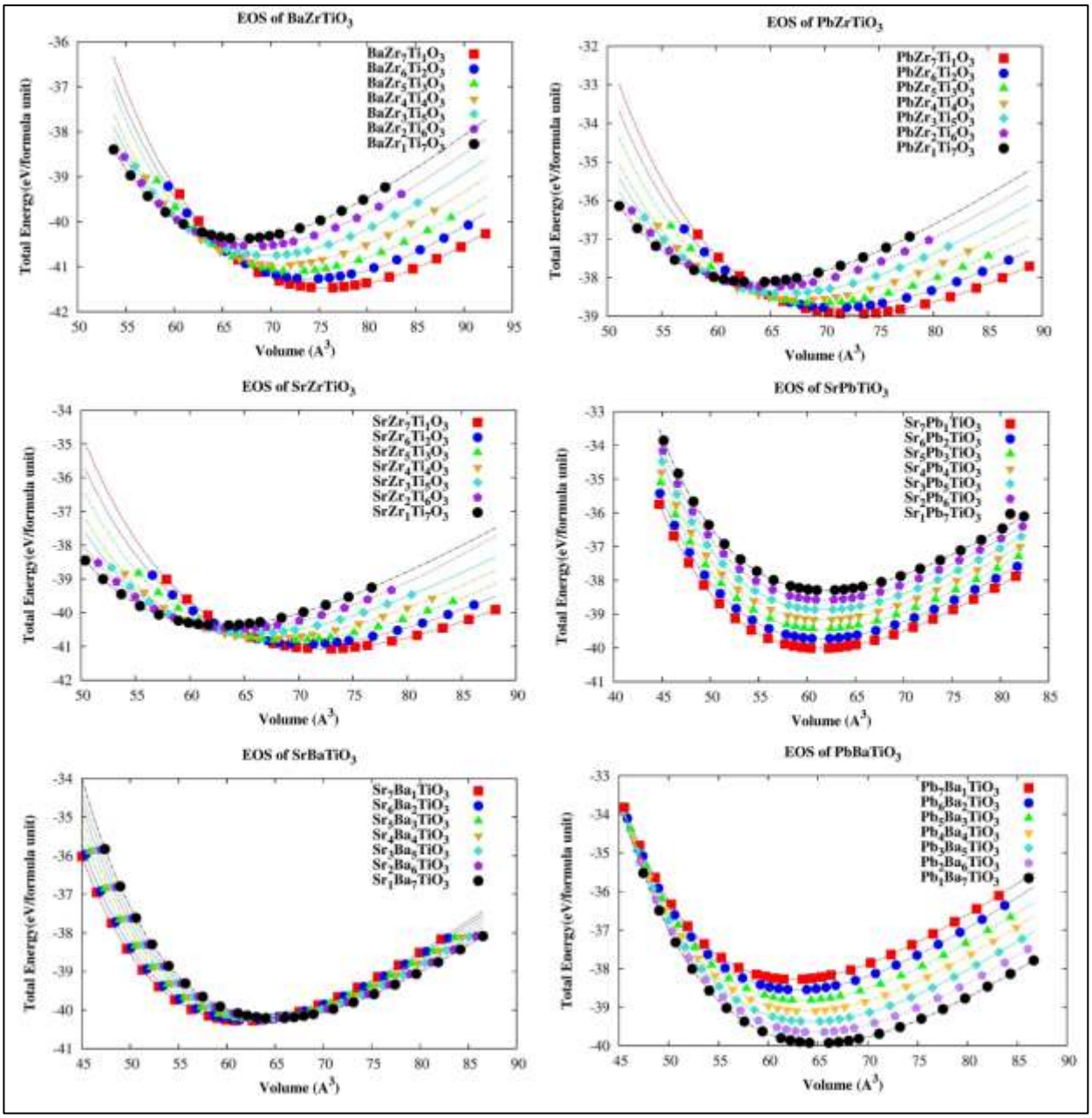


Figure 3.7 Total energies as a function of primitive cell volume for 2x2x2 cubic structures

The elasticity of the cubic crystal is completely described by the three independent constants C_{11}, C_{12}, and C_{44} in GPa, and they are obtained by the three strains (C1, C2, C3) given in Table 3.6.

Table 3.6 The calculated elastic constants for pure perovskites

	C_{11}	C_{12}	C_{44}	Methods
$BaTiO_3$	281.67	103.75	119.78	Stress- Strain
	281.38	104.23	119.68	Energy-Strain
	255	82	108	[95] Exp.
	305	106	128	[48] Theory
$PbTiO_3$	288.21	122.52	96.64	Stress- Strain
	287.67	119.05	96.94	Energy-Strain
	229	100	100	[53] Exp.
	324	155	109	[50] Theory
$SrTiO_3$	316.69	103.79	111.93	Stress- Strain
	316.47	99.33	108.44	Energy-Strain
	319	97	113	[50] Theory
$BaZrO_3$	293.18	76.08	84.44	Stress- Strain
	293.18	77.61	82.06	Energy-Strain
	322	79	70	[51] Theory
$SrZrO_3$	317.18	70.52	71.92	Stress- Strain
	315.37	71.57	70.37	Energy-Strain
	338	71	77	[51] Theory
$PbZrO_3$	301.27	84.91	58.94	Stress- Strain
	303.12	85.13	61.48	Energy-Strain

The elastic constants are calculated by two different approaches. They are the energy-strain and stress-strain relationship in Table 3.6. They obey the following mechanical stability conditions in the cubic structure, which are given as:

$$C_{11} - C_{12} > 0, \quad C_{44} > 0, \quad (C_{11} + 2C_{12}) > 0 \tag{3.3}$$

More relevant to the purpose of this thesis, the elastic constants tensor has been calculated for all alloys, all concentrations, and all unique symmetry configurations corresponding to these concentrations. In Table 3.7, the resulting elastic constants for cubic and non-cubic cases are present (due to emergence of a small tetragonal structure in some structures where 6 independent elastic constants arise) for PZT. The results for the

complete set of alloys with unique symmetry configurations for all concentration are given in the Supplementary Material/Appendix as tables.

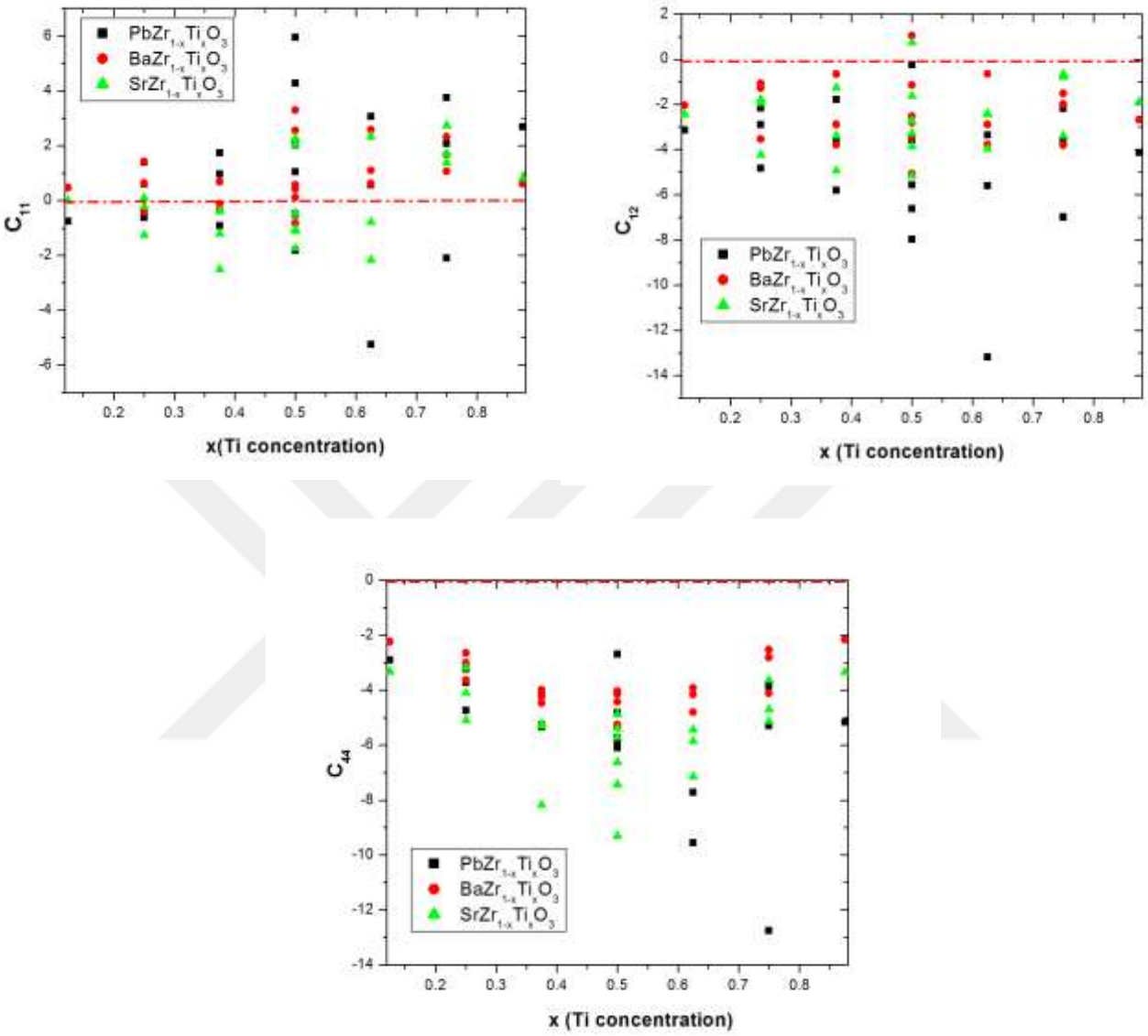


Figure 3.8 The variation of elastic constants as a function of concentration in PZT, BZT and SZT

It is important to point out that the behavior of the elastic constants as a function concentration and different symmetry unique configuration is to apply Vegard's rule for the property and calculate the deviation from this value and then to note if the property increased or decreased as a result of the mixing. The variation of elastic constants as a function of concentration and dependence on symmetry inequivalent configurations at each concentration in PZT, BZT, and SZT are displayed in the deviation from the values that are obtained via the application of Vegard's rule of combination, as shown in Figure 3.8. In C_{44} for all compounds, all configurations show a negative deviation. Therefore the

alloys PZT, BZT, and SZT all weakens for the pure shear response of the resulting material, which in many cases, this represents a weakening of ca. 10%. The variation of the C_{12} values display a similar behavior in almost all concentrations as a decrease with respect to Vegard's Rule resulting in ranges from 2% - 6%, except in the 50-50 case where it shows roughly a 1% increase in only one configuration in both BZT and SZT. However, the C_{11} values for the different concentrations and corresponding unique configurations show both negative and positive deviations, and the distribution tending to be heavily positive. In these calculations in the slightly tetragonal supercells, the systems were assumed to be pseudo cubic, and the largest c/a ratio being 1.015, which is a reasonable assumption.

Table 3.7 The calculated elastic constants (Cij in GPa) for PZT

	C_{11}	C_{12}	C_{44}	C_{13}	C_{33}	C_{66}
$Pb_8Zr_7Ti_1O_{24}$	300.44	86.23	63.01	-	-	-
$Pb_8Zr_6Ti_2O_{24}$ [a]	300.65	88.79	65.61	88.94	297.69	65.73
$Pb_8Zr_6Ti_2O_{24}$ [b]	299.86	91.45	66.62	-	-	-
$Pb_8Zr_6Ti_2O_{24}$ [c]	298.64	90.71	67.11	90.22	300.51	65.92
$Pb_8Zr_5Ti_3O_{24}$ [a]	296.42	92.04	69.44	91.38	300.55	68.46
$Pb_8Zr_5Ti_3O_{24}$ [b]	299.06	94.27	69.51	95.48	296.39	70.09
$Pb_8Zr_5Ti_3O_{24}$ [c]	298.29	96.07	70.65	-	-	-
$Pb_8Zr_4Ti_4O_{24}$ [a]	293.59	94.13	73.23	93.32	302.50	72.99
$Pb_8Zr_4Ti_4O_{24}$ [b]	301.35	98.51	73.45	102.76	291.01	76.03
$Pb_8Zr_4Ti_4O_{24}$ [c]	296.44	101.84	76.53	-	-	-
$Pb_8Zr_4Ti_4O_{24}$ [d]	294.90	95.47	73.47	94.18	295.73	70.84
$Pb_8Zr_4Ti_4O_{24}$ [e]	299.67	98.68	74.39	97.80	294.77	74.10
$Pb_8Zr_4Ti_4O_{24}$ [f]	297.43	96.52	73.11	-	-	-
$Pb_8Zr_3Ti_5O_{24}$ [a]	288.23	93.15	74.09	92.97	291.74	50.61
$Pb_8Zr_3Ti_5O_{24}$ [b]	296.53	100.72	75.93	103.12	290.09	73.66
$Pb_8Zr_3Ti_5O_{24}$ [c]	294.03	102.97	51.56	-	-	-
$Pb_8Zr_2Ti_6O_{24}$ [a]	289.44	103.58	82.78	104.30	295.47	69.69
$Pb_8Zr_2Ti_6O_{24}$ [b]	295.29	108.40	84.23	-	-	-
$Pb_8Zr_2Ti_6O_{24}$ [c]	293.62	106.91	75.32	105.62	292.01	69.30
$Pb_8Zr_1Ti_7O_{24}$	292.29	110.67	87.34	-	-	-

In order to understand the influence of the structural configurations at equilibrium, the structural parameters are computed for different values of concentration x of $A_xA'_{(1-x)}BO_3$ alloys given in Table 3.7. It is shown that E_0 does not change with respect to the symmetry equivalent positions. The symmetry non-equivalent positions generated very small changes in the total energy. Due to the atom size difference in alloy-compounds, the structures deviate from the cubic form to tetragonal form, hence the potential for development of permanent dipole moments/polarization through alloying in ABO_3 systems. Therefore one can modify the alloy content/specific alloy-compound structure to improve on the polar properties, i.e. increasing electromechanical response in these materials. The elastic constants of the different types of alloys are given in Appendix B.

3.3.5 Mixing Energies and Mechanical Stability of Alloying

The quantum mechanical DFT calculations are analyzed to capture the mixing energies between oxides using energies of optimized structures at each concentration and configuration and for the base compounds. The mechanical calculation of the mixed alloying in different supercell geometries is used to identify the most stable ground state computation. DFT calculations are analyzed to capture the mixing energies between the oxides. In this section, all pure phases in a unit cell have been employed while the solid solutions of alloy have the concentrations of 0.875, 0.75, 0.625, 0.50, 0.375, 0.25, and 0.125 in a $2x2x2$ supercell. The modeled structures are treated to be pseudocubic and enough to be quantitatively comparable. Internal cell parameters are allowed to relax, and the cell volume is fixed at different values. The estimated energies are fitted to the Birch – Murnaghan equation, and the minimum energies are used for further analysis [59]. The energies of the pure phases are used for calculating the mixing energy according to E_{mix}:

$$E_{mix} = E_{alloy} - (1 - x)E_A - xE_B \tag{3.4}$$

where E_{alloy}, E_A and E_B are the total energy of the mixed structure, the total energy of the A-type perovskite alloy, and the total energy of the B-type perovskite alloy, respectively. The calculated mixing energies versus the different atom concentrations for the given structure are presented in Figure 3.9 and Figure 3.10.

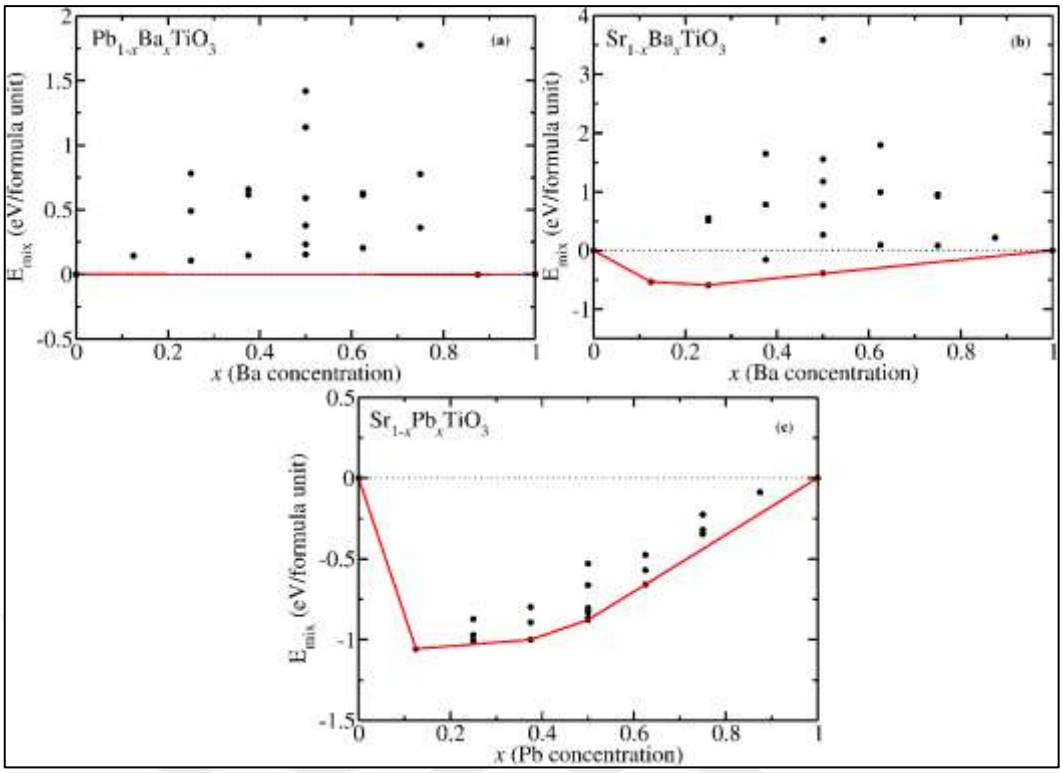


Figure 3.9 Convex hull diagram for A-type perovskite cubic alloy (a) $Pb_{(1-x)}Ba_xTiO_3$ (b) $Sr_{(1-x)}Ba_xTiO_3$ (c) $Sr_{(1-x)}Pb_xTiO_3$

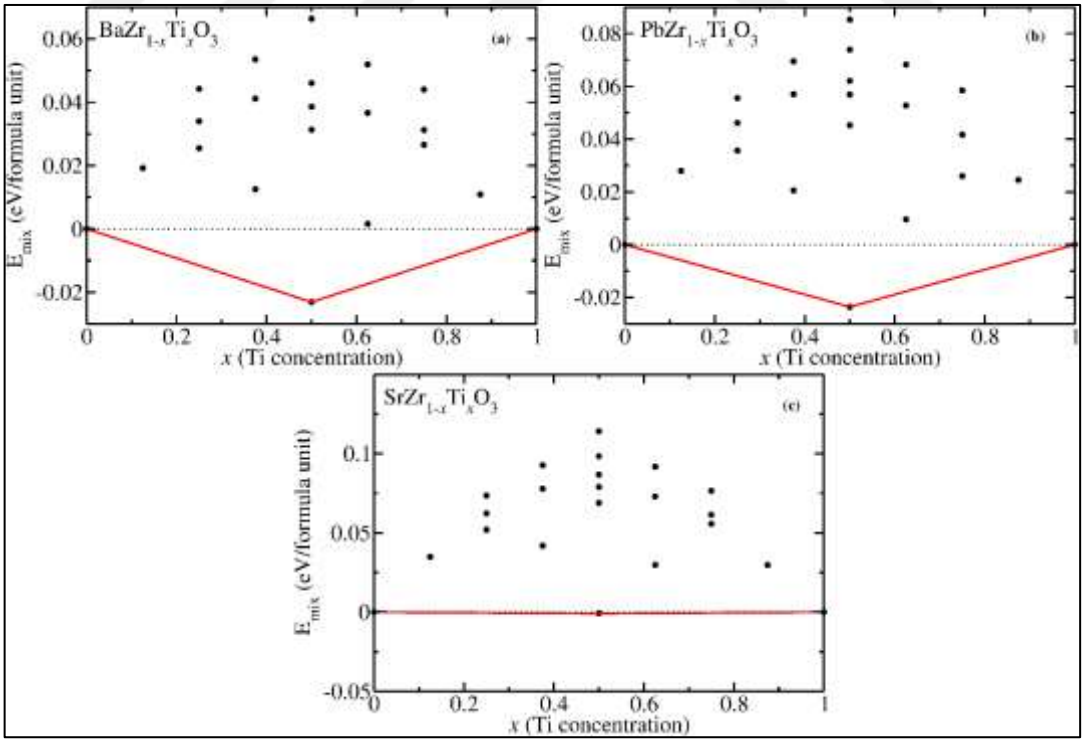


Figure 3.10 Convex hull diagram for B-type perovskite cubic alloy (a) $BaZr_{(1-x)}Ti_xO_3$ (b) $PbZr_{(1-x)}Ti_xO_3$ (c) $SrZr_{(1-x)}Ti_xO_3$

For simplicity, the supercell that contains the same number of formula units has been drawn for all alloy figures (Figure 3.9 and Figure 3.10). As seen in Figure 3.9, $Sr_{1-x}Pb_xTiO_3$alloy with negative mixing energies are obtained. The mixing energies of $SrZr_{1-x}Ti_xO_3$ are all positive except $SrZr_{0.5}Ti_{0.5}O_3$. This phase is barely stable since it has a negative mixing energy.

The mixed alloys were observed to be mechanically stable, and the thermodynamic stability of these systems was examined in order to pursue more favorable piezoelectric materials. It is noted that cubic perovskite structures exist at high temperatures. The Gibbs free energy plays an important role due to the entropy in the processes of chemical thermodynamics, and whose relation is given by the equation of $G(p,T) = U + pV - TS$ rather than the energy contributions due to ordering and phase decomposition. The total internal energy (U) defines the value of the Gibbs free energy at absolute zero. The calculations were carried out with the help of the DFT as implemented in the VASP software at $0K$. The minimum value of the energy is expected to be lower than its standard value. Since the configuration entropy is equal to $k\,In\Omega$, there will be an increase in entropy throughout the mixing process even at $0K$. Besides, the value of ΔF will not change since each element of mixing will have the same energy loss and the same entropy increase even though they were mixed at high temperatures. The most stable types of compounds were investigated during mixing and created a database for configuration entropy. Researches have revealed that the alloys have the tendency of mixing even at room temperature $k_BT \cong 23meV$. Consequently, it has been shown that these alloys could easily constitute mixing at room temperature.

It is shown that the differences of B-sites in mixing energies for cation arrangements is essential with regard to the size differences and related stresses in the oxygen octahedral.

3.4 Conclusion

We have obtained the ground structural properties and elastic properties of ABO_3 type perovskite structures and their alloy forms from first-principle calculations. We have also showed thermodynamic properties by convex hull diagram. The results of the A/B-site complex perovskite calculation show that the alloy perovskites can be mixed both mechanically and thermodynamically. The c/a ratio have also been calculated for the cubic form of alloy perovskite structures.

CHAPTER 4

PIEZOELECTRIC PROPERTIES OF ABO_3 PEROVSKITE AND THEIR ALLOYS

4.1 Introduction

Piezoelectric materials can be used an alternative renewable energy resources. The main goal is tis thesis is to explore piezoelectric effect on perovskite structures and their alloy forms. To be more specific and the question how the piezoelectric effect is has reached the maximum. Together with the piezoelectric material can not generate much energy, all studies are focused on increase of the piezoelectric effect.

Piezoelectric materials can be natural or man-made. Man-made piezoelectric materials are obtained in many different ways that are altering the electrode pattern, changing the poling and stress direction. All developments has focused on improve the efficiency of energy harvesting by altering the configuration of piezoelectric materials.

When an electric field is applied on a material, the material gives a response that is identify its electrical properties. If the electric current is flow freely in the material, it is called conductors. Secondly, the electric current is flow under specific conditions, it is called semiconductors. Finally, the electric current cannot any conditions, it is called insulators or dielectrics. Even though the dielectrics do not electric current, they can polarize due to their geometry. Dipole moments or also known as electric dipole is created. The polarization of material defines a certain volume element in the material that carries a dipole moment.

4.2 Methodology

As we mention before, the cubic phase of ABO_3 type perovskite structures do not show any piezoelectric coefficients since they have inversion symmetry. A small magnitude of piezoelectric coefficients was just found in the previous chapter. In this chapter of the thesis, the only concern is the piezoelectric properties of the tetragonal form of perovskite structures. The targeted physical properties, which are second-order optical susceptibilities as well as piezoelectric coefficients, were calculated within the framework of the modern theory of polarization and DFPT as implemented in VASP. In order to better describe what is we meant by optical susceptibilities, consider the dipole moment per unit volume. Calculation of the elastic stiffness coefficients, the clamped-ion, and relaxed-ion coefficients were obtained by verifying whether or not the ionic positions were allowed to relax after applying strain. The relaxed-ion d_{11} coefficients were calculated from their respective clamped-ion e_{11} coefficients and elastic stiffness coefficients.

The effect of the structural size of piezoelectric materials has been a subject of limited study. Due to that fact that only a unit cell of ABO_3 type crystal structure is not enough to simulate its alloy properties, a supercell of several unit cells can be modeled. Even though the larger of system requires more computational resources, the simulation load was kept to a minimum. Basically, the piezoelectricity of ABO_3 type perovskite structure streams from structural displacements and can lift the inversion symmetry of the unit cell. The two most widely used mechanisms can give rise to polar displacement in the crystal. The first one comprises of the second-order Jahn-Teller distortion in which charge transfer between different electronic states break the inversion symmetry [78-83]. The second responsible for breaking the symmetry is driven by electrostatic ion-size mismatch factors. Due to chemical constraints, the small number of A and B-site atoms that produce these effects, limit the number of oxide perovskite compositions that can result in the non-centrosymmetric structures.

4.3 Results and Discussion

4.3.1 Ground State Properties

Because $BaTiO_3$ and $PbTiO_3$ tetragonal phases have a specific space group, alloying was used as a start for this system. In order to find the natural alloy's atomic position, a total

of 26 configurations were tested. In order to identify the ground-state structure, full atomic relaxations were performed. The equilibrium volume of the $Pb_xBa_{(1-x)}TiO_3$ was initially determined in eight different concentrations of tetragonal phase by calculating the total energy per primitive cell as a function of the volume. Structural and mechanical parameters of the $A_xA'_{(1-x)}B_yB'_{(1-y)}O_3$ type alloy are determined from the total energy as a function of volume by a least-squares fit of the third-order Birch-Murnaghan equation, which is given as Equation 4.2.

Figure 4.1 shows the total energy per formula unit (eV) versus volume ($Å^3$) for eight different stoichiometric ratios with different configurations of the doping atom which was lead (Pb) on barium titanate ($BaTiO_3$) in a $2x2x2$ supercell. The black spheres represent Pb atoms (A-site), the green spheres represent Ba atoms (A′-site), the blue spheres represent Ti atoms (B′-site) and the red spheres represent O atoms. The crystal structure of alloys is visualized using the program VESTA. The total calculated equilibrium energies (E0 in eV), the lattice parameters (a in Å), the bulk modulus (B in GPa), and the pressure derivative of the bulk modulus (B′) values for $Pb_xBa_{(1-x)}TiO_3$ are displayed in Table 4.1.

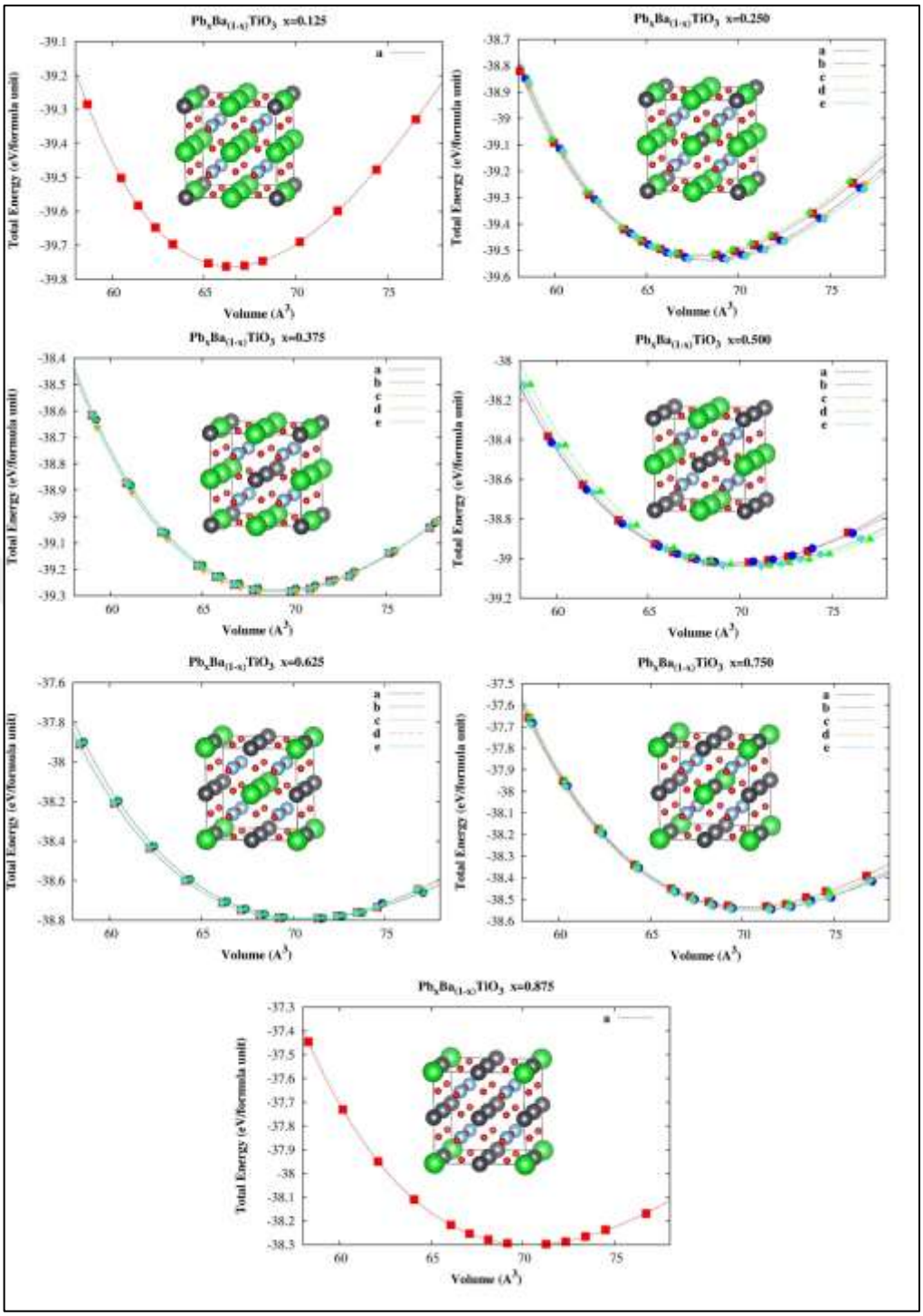


Figure 4.1 Total energy per formula unit versus volume for eight different stoichiometric ratio doping atom that is Pb on $BaTiO_3$

Table 4.1 The calculated structural properties for $Pb_xBa_{(1-x)}TiO_3$

	E_o(eV)	V_0 (Å³)	B	B′
$BaTiO_3$	-40.04	67.67	123.37	5.35
$Pb_{0.125}Ba_{0.875}TiO_3$	-39.76	66.47	126.09	5.86
$Pb_{0.25}Ba_{0.75}TiO_3$ [a]	-39.52	67.90	112.63	5.64
$Pb_{0.25}Ba_{0.75}TiO_3$ [b]	-39.53	68.27	111.35	5.32
$Pb_{0.25}Ba_{0.75}TiO_3$ [c]	-39.51	67.76	113.27	5.73
$Pb_{0.25}Ba_{0.75}TiO_3$ [d]	-39.54	68.30	110.71	5.47
$Pb_{0.25}Ba_{0.75}TiO_3$ [e]	-39.54	68.48	108.63	5.51
$Pb_{0.375}Ba_{0.625}TiO_3$ [a]	-39.29	69.15	107.02	4.84
$Pb_{0.375}Ba_{0.625}TiO_3$ [b]	-39.28	69.26	106.99	4.74
$Pb_{0.375}Ba_{0.625}TiO_3$ [c]	-39.28	69.24	106.13	4.87
$Pb_{0.375}Ba_{0.625}TiO_3$ [d]	-39.28	69.08	104.62	5.27
$Pb_{0.375}Ba_{0.625}TiO_3$ [e]	-39.28	69.11	104.78	5.22
$Pb_{0.5}Ba_{0.5}TiO_3$ [a]	-39.02	69.73	99.81	5.23
$Pb_{0.5}Ba_{0.5}TiO_3$ [b]	-39.02	69.73	100.62	5.06
$Pb_{0.5}Ba_{0.5}TiO_3$ [c]	-39.05	70.93	98.21	4.37
$Pb_{0.5}Ba_{0.5}TiO_3$ [d]	-39.04	70.19	97.89	5.24
$Pb_{0.5}Ba_{0.5}TiO_3$ [e]	-39.04	70.24	98.69	4.99
$Pb_{0.625}Ba_{0.375}TiO_3$ [a]	-38.79	70.36	96.77	4.78
$Pb_{0.625}Ba_{0.375}TiO_3$ [b]	-38.80	70.85	100.45	3.91
$Pb_{0.625}Ba_{0.375}TiO_3$ [c]	-38.79	70.72	101.74	4.03
$Pb_{0.625}Ba_{0.375}TiO_3$ [d]	-38.79	70.38	96.29	4.83
$Pb_{0.625}Ba_{0.375}TiO_3$ [e]	-38.79	70.28	97.89	4.47
$Pb_{0.75}Ba_{0.25}TiO_3$[a]	-38.53	70.27	97.73	4.47
$Pb_{0.75}Ba_{0.25}TiO_3$[b]	-38.55	70.77	94.53	4.41
$Pb_{0.75}Ba_{0.25}TiO_3$[c]	-38.54	70.52	91.32	5.51
$Pb_{0.75}Ba_{0.25}TiO_3$[d]	-38.55	70.54	91.00	5.24
$Pb_{0.75}Ba_{0.25}TiO_3$[e]	-38.55	70.56	89.40	5.34
$Pb_{0.875}Ba_{0.125}TiO_3$	-38.31	70.59	98.53	3.52
$PbTiO_3$	-38.08	70.25	83.31	5.80

We have also carried out the theoretical analysis of the applicability of the Vegard's linear law. As seen from Figure 4.2 and Figure 4.3, the variation of lattice constants is linear and displays a close agreement with Vegard's law.

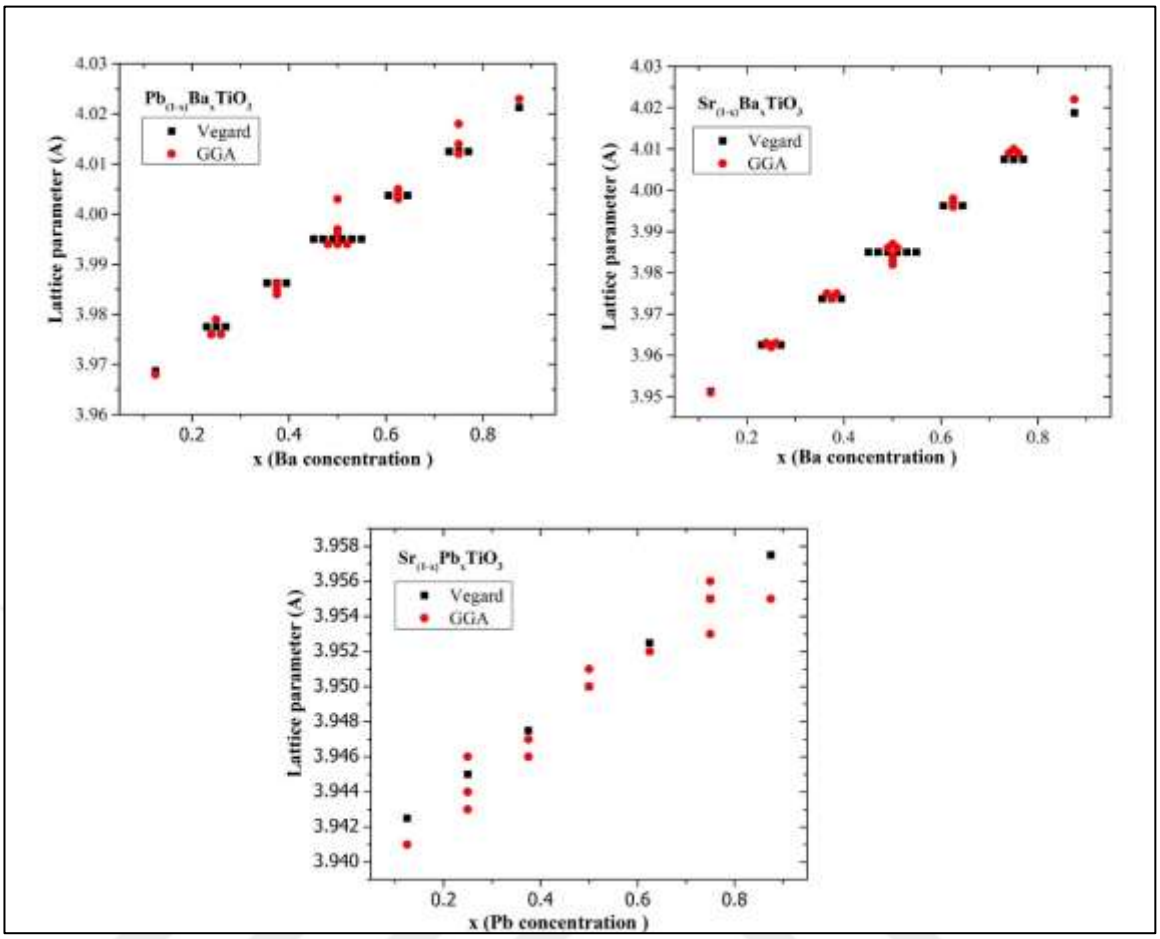


Figure 4.2 The variation of lattice constants as function of concentration and dependence on symmetry inequivalent configurations in PBT, SBT and SPT

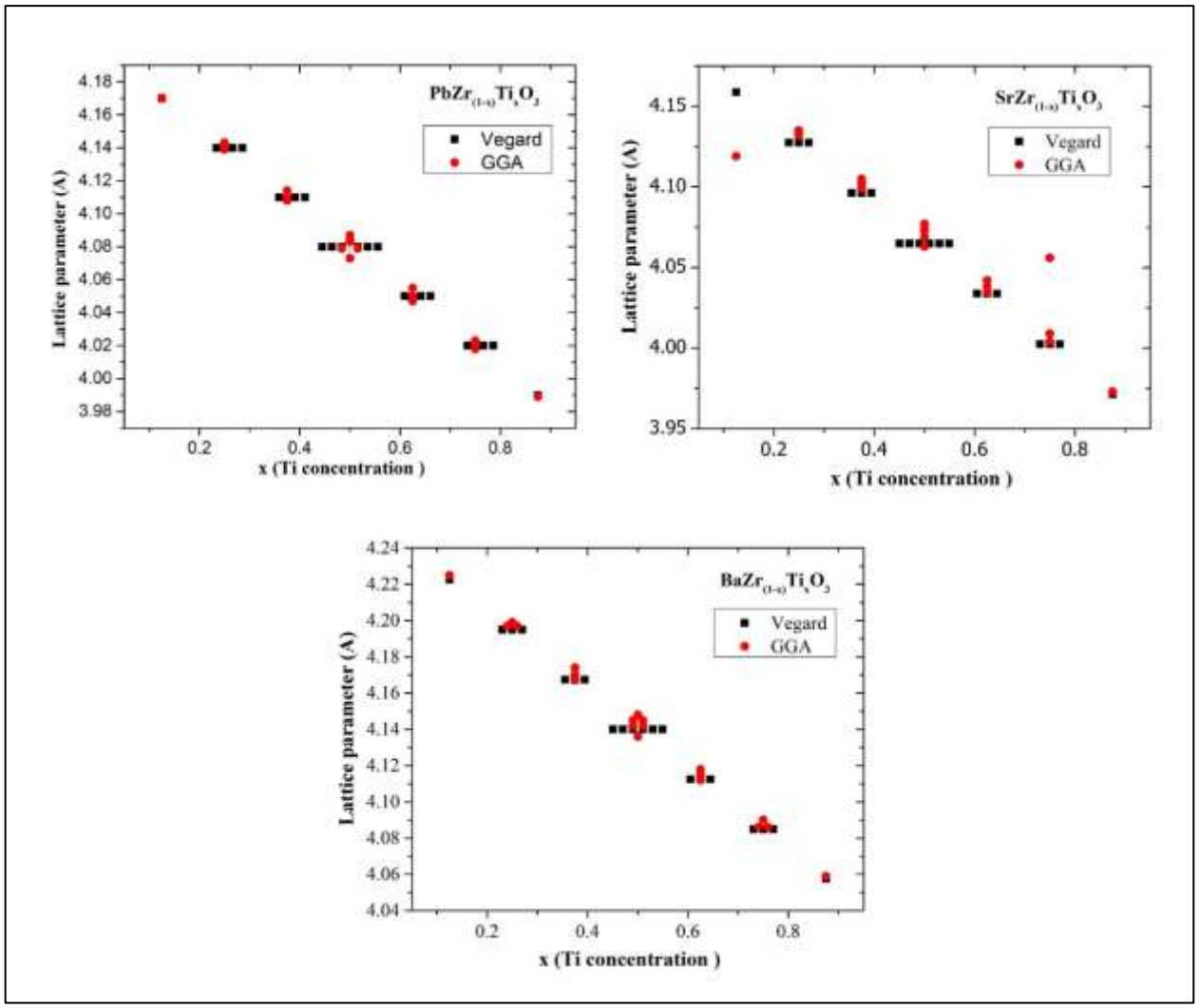


Figure 4.3 The variation of lattice constants as function of concentration and dependence on symmetry inequivalent configurations in PZT, SZT and BZT

4.3.2 Electrical Polarization

Before the calculation of the piezoelectric coefficients, the electrical polarization will be emphasized. Basically, electric polarization is identified as an electric dipole moment of the volume of the finite crystal [84]. If charge density is represented by $\rho(r)$ and the finite crystal is neutral as a whole, it can write as

$$\int \rho(r) d^3r = 0 \tag{4.1}$$

The polarization description in the finite crystal as

$$P = \frac{1}{V} \int_{V_{first}}^{V_{last}} \rho(r) r d^3r \tag{4.2}$$

where V is the volume of the crystal. Because of charge neutrality this definition does not depend on the origin. It means that if the crystal is not uniform just one needs to identify

polarization as a function of position r. Even in the absence of the external electric field, some crystal have finite polarization is called spontaneous polarization. When the fact comes from temperature, it is called pyroelectric or the fact comes from electric polarization which induced by applying stress, it is called piezoelectric.

4.3.3 Calculation of Piezoelectric Coefficients

Piezoelectric properties are ground-state properties associated with polarization. Direct and converse piezoelectric constants describe the polarization P induced by strain ε and the strain σ induced by an external electric field E, respectively:

Direct piezoelectric constants at a constant field

$$P = e\varepsilon \tag{4.3}$$

Converse piezoelectric constants at a constant stress

$$\varepsilon = dE \tag{4.4}$$

Piezoelectric constants are computed using the DFPT based on the use of LEPSILON=T and IBRION=8 which is what is implemented in the VASP. d_{33} has been calculated for the converse piezoelectric constants of $Pb_xBa_{(1-x)}TiO_3$ (a), $Sr_xBa_{(1-x)}TiO_3$ (b), and $Sr_xPb_{(1-x)}TiO_3$ (c) with the tetragonal $P4mm$ structure and presented in Figure 4.4. When LEPSILON is set to true, it means that it is allowed to determine the static-ion clamped dielectric matrix with or without local field effects.

The Hessian matrix (matrix of the second derivatives of the energy with respect to atomic positions) is the vibrational frequencies of a system. Only the symmetry inequivalent displacements are taken into consideration. ISIF=3 allows to change the cell shape and cell volume and its fully relax ions in the solid.

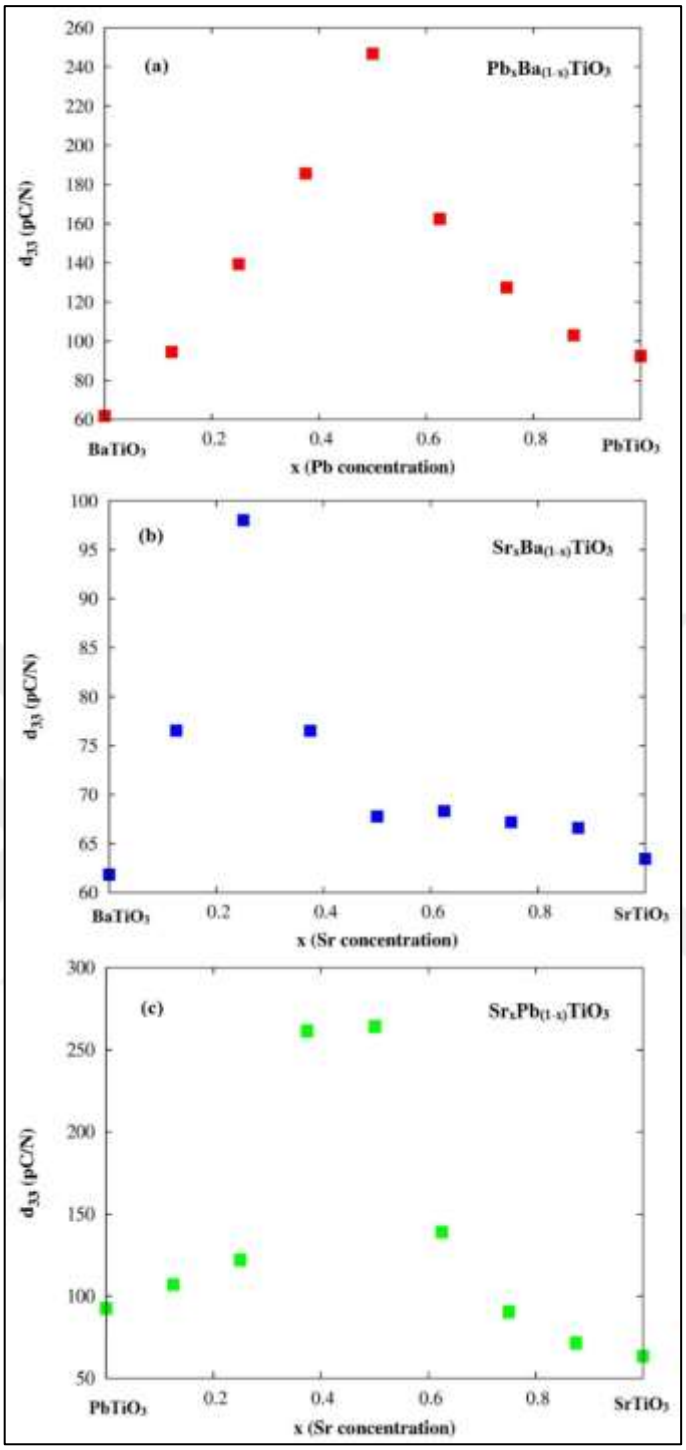


Figure 4.4 d_{33} direct piezoelectric constants for $Pb_xBa_{(1-x)}TiO_3$ (a) , $Sr_xBa_{(1-x)}TiO_3$ (b) and $Sr_xPb_{(1-x)}TiO_3$ (c) with the tetragonal P4mm structure

Two different kinds of pure $Pb_xBa_{(1-x)}TiO_3$ was found 1.96 eV. The large values of e_{11} and d_{11} piezoelectric coefficients were calculated for $Pb_xBa_{(1-x)}TiO_3$: $e_{11} = 3.833\ \mathrm{C}/m^2$ at $Pb_{0.25}Ba_{0.75}TiO_3$ concentration and $d_{11} = 267.569\ \mathrm{C}/N$ at $Pb_{0.625}Ba_{0.375}TiO_3$ concentration for tetragonal ground-state structures. They are significantly higher than their pure form and for other configurations as well. The lowest

energy configuration is selected in the previous chapter. This study therefore indicates that large piezoelectric coefficients can be obtained with constructing alloy systems.

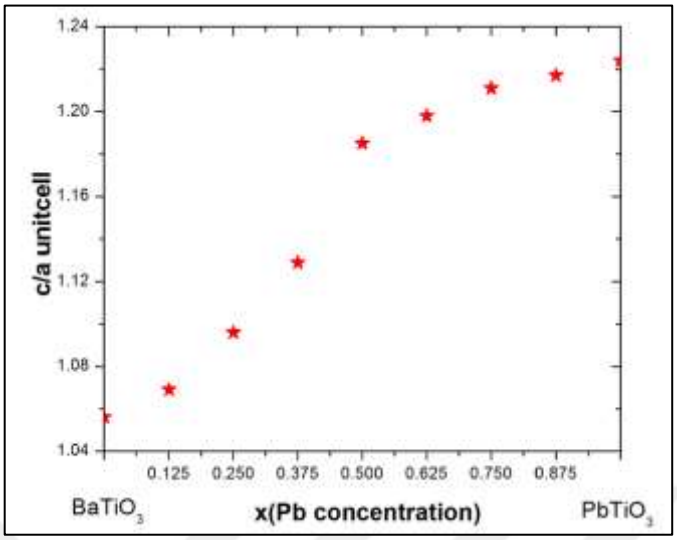


Figure 4.5 c/a ratio for different concentration of tetragonal phase $Pb_xBa_{(1-x)}TiO_3$

The large size of the c/a ratio on the perovskite structure related to a large polarization and an enhanced electromechanical response. Higher tetragonality was observed in samples with higher piezoelectric responses. The understanding of the c/a ratio of the ferroelectric perovskite provides guidance for the design of new materials with enhanced performances [92-93]. In other words, tetragonality is proportional to the c/a ratio. Figure 4.5 is a plot of the c/a ratio for different concentrations of the tetragonal phase of $Pb_xBa_{(1-x)}TiO_3$. The c/a values increase with the doping Pb concentration to $BaTiO_3$. The result shows that the c/a ratio immediately jumps to a higher c/a ratio at 0.5:0.5. Related to the c/a ratio, piezoelectric constants values are getting higher in magnitude as well.

The tetragonal type perovskite crystals with the c/a=1.011 ratio exhibit superior piezoelectric properties, d_{33} ~230 pC/N. The main idea behind piezoelectricity is defined as the motion of the cation atom of B-sites along the c-axis.

In this work, enhanced piezoelectric coefficients were found at the alloy forms of $BaTiO_3$, $SrTiO_3$ and $PbTiO_3$. The tetragonal form of $BaTiO_3$ and $PbTiO_3$ are of the same crystal structure ($P4mm$), and their piezoelectricity is produced by Ti atoms moving along the c-axis. Because $SrTiO_3$ has different space groups of the tetragonal form ($I4/mcm$), it can be shown that piezoelectricity is possible by BO_6 octahedral distortions. The $SrTiO_3$ primitive unit cell of a body-centered tetragonal lattice consists of 10 atoms (the unit cell is doubled). $SrTiO_3$ shows $BaTiO_3$'s piezoelectricty in all calculations.

To understand the meaning of piezoelectric coefficients components, subscripts of the piezoelectric coefficients will be the main focus. Simply, the piezoelectric charge constant d_{ij} is the polarization generated per unit of mechanical stress, which is the second-rank tensor. The first subscript of d_{ij} shows the direction of polarization generated in the material when the electric field E is zero. The second subscript of d_{ij} indicates the direction of the applied stress or the induced strain. The lack of inversion symmetry determines the number of piezoelectric coefficients. For the tetragonal structure, there are three independent piezoelectric coefficients. With d_{33}, the induced polarization (strain) is parallel to the applied stress (electric field), whereas with d_{31} and d_{15}, the induced polarization (strains) are perpendicular to the applied stress (electric field) [85-86].

The meaning of subscripts will heavily be focused for the piezoelectric coefficients. The first subscript of d indicates the direction of polarization generated in the material when the electric field E is zero or alternatively, is the direction of the applied field strength. The second subscript is the direction of the applied stress or the induced strain.

d_{33} : induced polarization in direction 3 (parallel to the direction in which the ceramic element is polarized) per unit stress applied in direction 3 or induced strain in direction 3 per unit electric field applied in direction 3.

d_{31} : induced polarization in direction 3 (parallel to the direction in which the ceramic element is polarized) per unit stress applied in direction 1 (perpendicular to the direction in which the ceramic element is polarized) or induced strain in direction 1 per unit electric field applied in direction 3.

d_{15} : induced polarization in direction 1 (perpendicular to the direction in which the ceramic element is polarized) per unit shear stress applied in direction 2 (perpendicular to the direction in which the ceramic element is polarized) or induced shear strain in direction 2 per unit electric field applied in direction 1.

The direction, in which d_{33} is the maximum function of piezoelectric d_{ij} coefficients, is referred to as the crystallographic coordinate system.

If the sign of the piezoelectric coefficient is negative, it means the crystal is negatively charged.

4.3.4 Calculation of Born Effective Charges

There are many investigations concerning of atomic charges in solid-state physics for quite some time. The atomic charge first appears as a static concept. Static charge usually depends on contributions from the ground state electron density. One of atomic charges is the Born effective charges (BEC, Z^*) and was introduced by Born in 1933 [90]. In order to obtain BEC, also known as transverse or dynamical charges, it is a fundamental quantity that induces coupling between lattice displacements and electrostatic fields. BEC is indeed a macroscopic concept involving the polarization of valence electrons. Using the ab-initio techniques BEC can be theoretically derived. The corresponding linear response computations were performed. The technical details of the computation for the responses to the atomic displacements, homogeneous electric fields, and strains are based on DFPT. BEC tensors measure the coupling of a macroscopic field with relative sublattice displacements in the crystal structure. They relate the macroscopic polarization to the atomic scale displacements by the following equation

$$P_{\propto} = \frac{e}{\Omega} \sum Z^{*}_{i\alpha\beta}\, \delta u_{i\beta} \qquad (4.5)$$

where i denotes the i^{th} atom, and α and β are the direction of the polarization component and atomic displacement, respectively. In strongly ferroelectric materials, the BECs are significantly different from the anticipated nominal electric charge on the ion. At the same time, the dipole moment enables us to define a static charge $Z(u) = \frac{P(u)}{u}$ and a dynamic charge $Z^*(u) = \frac{\partial P(u)}{u}$ also equal to $Z(u) + u\frac{\partial P(u)}{\partial u}$. U is defined as the interatomic displacement.

The investigation of the BECs emphasize why some charges are larger than nominal charges and is also an indicator of long-range Coulomb interactions that help to clarify the origin of polarization in the material. The BECs are sometimes twice as high as their nominal ionic charge.

Therefore, many studies on the BEC of ABO_3 type perovskite structures help to deeply understand the reason of some of these physical properties. Ghosez et al. [87] had calculated the BEC of $BaTiO_3$, and the charges are +2.77 for Ba, +7.25 for Ti, -5.71 for $O_{\parallel}$ and -2.15 for $O_{\perp}$, respectively. For the cubic structure, A and B cations are located at the center of the cubic symmetry, and their effective charge tensors are isotropic. The oxygen atoms are located at the face centers, and therefore they have two inequivalent directions being perpendicular and parallel, which define $O_{\parallel}$ and $O_{\perp}$ for the displacement

of O in the Ti and Ba direction. They use the bond by bond decomdecomposition of Z^* as a useful tool to investigate the role of covalency and ionicity without any preliminary hypothesis on the orbital in which they interact. The BEC values are relatively unresponsive to the isotropic volume change since they are strongly dependent on the change of atom position associated with the phase transitions.

Resta et al. [89] have suggested that strong variations of the BECs relative to nominal ionic values are due to the large inequivalence of the O ions. It was also reported that BECs calculated from first-principles method, are affected by optical phonon modes and arise from Nb atoms having 4d states and O atoms having 2p hybridized covalent bonding between metal and oxygen atoms, respectively [44,45].

Table 4.2 Comparative Born effective charges for different ABO_3 perovskites.

Perovskites	Z_A^*	Z_B^*	$Z_{O,\parallel}^*$	$Z_{O,\perp}^*$
$BaTiO_3$	2.745	7.488	-5.943	-2.144
$PbTiO_3$	3.852	7.338	-6.076	-2.555
$SrTiO_3$	2.545	7.448	-5.928	-2.033
$BaZrO_3$	2.741	6.213	-4.905	-2.024
$PbZrO_3$	3.913	6.045	-4.957	-2.499
$SrZrO_3$	2.577	6.107	-4.935	-1.874

In the present calculations of the BECs, values for all pure perovskites are given in Table 4.2. It is seen that the BECs of these materials are significantly larger than formal charges as expected [46]. It can be concluded that there is a noteworthy amount of covalent character present in the structure. The maximum effective charges of the $BaTiO_3$ structure are found at 2.74 for Ba, 7.44 for Ti and -5.94 for O showing +37%, +86% and -197% change from their static charge, respectively. The BEC results of $BaTiO_3$ are in agreement with those obtained by Ghosez [87]. The high Z^* values indicate that relative displacement of neighboring highly polarizable O 2p electrons. Hybridization between O 2p and unoccupied metal d orbitals is already well known from previous works [91]. The hybridization of $BaTiO_3$, $SrTiO_3$, and $PbTiO_3$ that have a Ti atom with 3d states is higher than $BaZrO_3$, $SrZrO_3$, and $PbZrO_3$ that have a Zr atom with 4d states. Despite all perovskites having the same type of hybridization, the difference streams from the interaction of the 2p oxygen atoms. According to the results of the BEC for different ABO_3 perovskite structures, it shows that $PbZrO_3$ has the maximum covalent character among these six perovskites.

For the prototype of the cubic perovskite structure, the metal atoms A or B sit at the center of the cubic symmetry that result in the isotropic effective charges along the diagonal of

the charge tensor. Oxygen atoms that are positioned at the face centers have two independent components of effective charge, which arise from the displacement of the oxygen ion in B-O direction or perpendicular to it. It is well understood that the large value of the B charges (Ti and Zr) result from the effect of covalent bonding with O atoms.

The calculated BEC deviates only slightly from the formal charges, revealing weak covalent interactions between the transition metal and oxygen atoms in this material. The acoustic sum rule of Born effective charges is well satisfied in the following calculations.

$$\sum_i Z_i^* = Z_A^* + Z_B^* + Z_{O_\parallel}^* + 2Z_{O_\perp}^* \quad (4.6)$$

It is important that it is persevered by Norn effective charges.

4.3.5 Calculation of Dielectric and Piezoelectric Constants

The dielectric properties of the alloys for various concentrations are determined using the linear response theory as implemented in VASP. It computes the components on the diagonal of the ion- clamped static dielectric tensor from the change in the electronic dipole moment due to electric field.

$$\varepsilon_{ij} = \delta_{ij} + \frac{4\pi}{\varepsilon_0}\frac{\partial P_i}{\partial E_j} \ (i,j = x,y,z) \quad (4.7)$$

For some concentrations where the structure slightly deforms into a tetragonal form exhibit this character in dielectric constants, deviation from cubic symmetry $e_{11}=e_{22}=e_{33}$ is lower than 1%, which are compatible with the deviations in lattice parameters. As seen from Figure 4.6, the variation of dielectric constants are linear (using the fact that the values in slightly tetragonal phases are very close, a pseudo cubic assumption was made and plotted only one/average of one nonzero component of dielectric tensor value) and display quite a close agreement with Vegard's law ($\varepsilon_{alloy} = x\varepsilon_A + (1\text{-}x)\varepsilon_B$) for all concentrations. The variation of the dielectric constants for the other alloys is given in the Supplementary Material/Appendix, and they also exhibit a close agreement with Vegard's law as well.

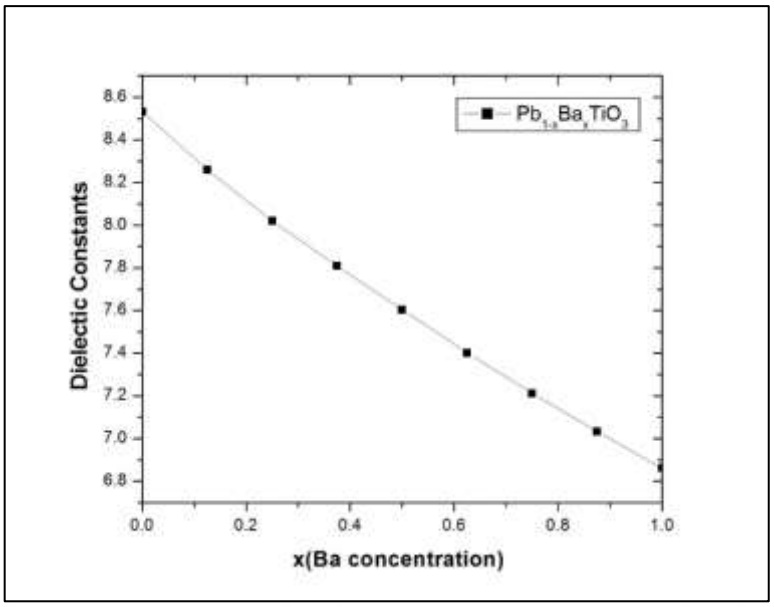


Figure 4.6 Dielectric constants of $Pb_{(1-x)}Ba_xTiO_3$ according to Ba concentration

Dielectric constants can have a polarization contribution due to the electrons, ions, and molecular dipole contribution. Each of these polarization contributions results in piezoelectricity. In this study, the dielectric constants were measured under stable stress at 0K.

Piezoelectric properties of mixing alloying were also investigated in different ratios within DFPT. Piezoelectricity is basically a linear interaction between the conversion of mechanical and electrical energy in the non-centro symmetric crystals or similar structures. Basically, piezoelectric effecst streams from the change of polarization upon a deformation. This is the reason why polarization exhibits an alteration between the positively and negatively charged ion positions in the lattice.

ABO_3 type perovskite structures adopt a cubic perovskite structure. Through this study, cubic ABO_3 type perovskite structures crystallize into cubic unit cells with five atoms, which the A-atom is at the corner of the cube, the B-atom is at the center and oxygen is located at the center of faces. Usually, the cation displacement away from the oxygen cage center causes the deviation from the cubic symmetry that relates to the properties of the A and B substituted atoms.

Piezoelectric constant tensors have been calculated for all alloys, all concentrations, and all unique symmetry configurations and corresponding concentrations. The results of piezoelectric coefficient are presented for the $BaZr_{(1-x)}Ti_xO_3$ cubic form of perovskite structures in Table 4.3. According to previous statements, crystals have at most 18

independent d_{ij} for an arbitrary form. The d_{ij} notations are of a $3x6$ matrix. The cubic form of perovskite structures does not show any piezoelectric effects because of high symmetry reason. However, in this scenario, owing to the crystallographic site being occupied by different types of atoms, the inversion symmetry breaks down and the structures develop small tetragonality characteristic. This result registers that these alloys have a piezoelectric coefficient of a magnitude $10^{-15}C/N$ magnitude. The chemical/configuration induced piezoelectricity exists in the pseudo cubic structures as well. Their magnitudes are smaller than the feasible ranges for actual application needs, but it can be improved for the use in future works.

Table 4.3 Calculated piezoelectric coefficients for $BaZr_{(1-x)}Ti_xO_3$ cubic form

	d_{11}	d_{12}	d_{13}	d_{21}	d_{22}	d_{23}	d_{31}	d_{32}	d_{33}
$Ba_8Zr_7Ti_1O_{24}$	-0.157	0.176	0.176	0.201	-0.210	0.201	0.180	0.107	-0.164
$Ba_8Zr_6Ti_2O_{24}$[a]	0.080	0.554	0.330	0.119	-0.200	0.119	0.326	0.546	0.083
$Ba_8Zr_6Ti_2O_{24}$[b]	-0.173	-0.037	-0.037	-0.018	-0.110	-0.018	-0.021	-0.021	-0.158
$Ba_8Zr_6Ti_2O_{24}$[c]	-0.171	0.127	0.158	0.136	-0.171	0.151	0.327	0.327	-0.280
$Ba_8Zr_5Ti_3O_{24}$[a]	-0.144	0.186	0.175	0.170	-0.132	0.152	0.155	0.155	-0.043
$Ba_8Zr_5Ti_3O_{24}$[b]	-0.131	0.167	0.086	0.167	-0.181	0.167	0.095	0.164	-0.151
$Ba_8Zr_5Ti_3O_{24}$[c]	-0.469	0.294	0.294	0.298	-0.472	0.298	0.293	0.293	-0.466
$Ba_8Zr_4Ti_4O_{24}$[a]	-0.228	0.199	0.109	0.189	-0.213	0.098	0.049	0.049	-0.218
$Ba_8Zr_4Ti_4O_{24}$[b]	-0.503	-0.409	-0.561	0.150	-0.215	0.150	-0.560	-0.394	-0.492
$Ba_8Zr_4Ti_4O_{24}$[c]	-0.571	0.256	0.256	0.250	-0.524	0.250	0.266	0.266	-0.569
$Ba_8Zr_4Ti_4O_{24}$[d]	-0.226	0.358	0.038	0.090	-0.460	0.090	0.036	0.348	-0.204
$Ba_8Zr_4Ti_4O_{24}$[e]	-0.370	0.124	0.124	0.111	-0.195	0.115	0.116	0.091	-0.181
$Ba_8Zr_4Ti_4O_{24}$[f]	-0.278	0.237	0.237	0.225	-0.262	0.225	0.228	0.228	-0.282
$Ba_8Zr_3Ti_5O_{24}$[a]	-0.479	0.3844	0.147	0.4232	-0.451	0.197	0.094	0.094	-0.249
$Ba_8Zr_3Ti_5O_{24}$[b]	-0.163	0.267	0.382	0.101	-0.269	0.101	0.378	0.274	-0.139
$Ba_8Zr_3Ti_5O_{24}$[c]	-0.196	0.124	0.124	0.110	-0.210	0.110	0.125	0.125	-0.232
$Ba_8Zr_2Ti_6O_{24}$[a]	0.509	0.252	0.365	0.204	-0.276	0.204	0.387	0.233	-0.518
$Pb_8Zr_2Ti_6O_{24}$[b]	-0.552	-0.158	-0.158	0.106	-0.289	0.106	-0.149	-0.149	-0.541
$Pb_8Zr_2Ti_6O_{24}$[c]	-0.323	0.210	0.176	0.222	-0.323	0.164	0.073	0.073	-0.261
Ba_8 $Zr_1Ti_8O_{24}$	-0.451	0.266	0.266	0.269	-0.443	0.269	0.252	0.252	-0.495

4.4 Conclusion

In decade, demand of materials is increased for serve tachonological applications. In this thesis, computational studies of perovskite structures and their alloy forms are obtained using by computational and theoretical tools.

One of our studies is about obtain the highest piezoelectric constants under an external strain field. More importantly, we discovered the potential for development of permanent dipol moment in cubic form of alloy ABO_3 type perovskite structures. This result highlights the influence of symmetry onstructural configuration. Due to the atom size difference in alloy form of ABO_3 type perovskite structures, the structures change frım cubic form to tetragonal form. The effect of different type of A-cation and B-cation ordering, lattice strain are investigated. A significant contribute is added to literature for

understanding the relationship between microscopic and macroscopic properties as a piece to big picture. The c/a universal scaling in piezoelectric materials is arised with the displacement of cation B-site using first-pinciple calculations. The last conclusion of this chapter, many unsolves problems still exists. Lead-free perovskite alloy structures would be interesting topic for future directions. Composition- structure- property relations should put in the literature.

CHAPTER 5

CONCLUSION AND FUTURE WORKS

The major conclusions of the present work have been covered to follow outlines recently concerning the first-principles modeling of ABO_3 type perovskite structures. Throughout this thesis, structural, mechanical, dielectric, piezoelectric and thermodynamic properties of some pure ABO_3 perovskites and their alloy forms using first principle DFT calculations were studied. The elastic constants were obtained using the energy-strain and stress-strain relations.

The first main topic of this thesis presents the prediction of elastic and thermodynamic properties of some pure cubic ABO_3 perovskites and their alloy forms at $0\ K$ temperature. The cubic phase of eight perovskite crystals were selected and compared to the calculated lattice parameters and bulk modulus with the available experimental data. Then, it was shown that the calculated results agree well with experimental values. More relevant to the purpose of this work, the elastic constants tensor for all alloy forms were calculated, and the concentrations and all unique symmetry configurations corresponding to these concentrations were determined. The results of the elastic constants for cubic and non-cubic cases were briefly presented (due to the emergence of a small tetragonal structure in some structures where 6 independent elastic constants arise) for a complete set of alloy forms.

The most noteworthy result of the study was showing the piezoelectric coefficient as pure cubic perovskites structures. The reason for the rise of piezoelectricity is from the breaking down of the cubic symmetry when the alloy structures were constructed. The breaking down of the cubic symmetry comes about when one of the atoms shifts in a certain direction in the unit cell. Polarization occurs along the z-axis. This leads to the structure looking somewhat tetragonal; however, it is not exactly tetragonal, but the angle

between a and b cell vectors changes slightly by 90°. This is neutral. Using the values ISIF & IBRION that were previously used for optimization, a slight tetragonal shape is what is expected. Since the deviation of the angles is so small, it is pseudo-tetragonal.

Due to the atom size difference in alloy-compounds, the structures deviate from cubic form to tetragonal form, hence the potential for development of permanent dipole moments/polarization through alloying in ABO_3 systems. Therefore one can modify the alloy content/specific alloy-compound structure to improve on polar properties, i.e. increasing electromechanical response in these materials.

The theoretical predictions on the considered properties of some perovskites and their alloys would serve as a reliable reference for the future. The results of the prototype alloy structures indicate the potential for improvement on the piezoelectric response through alloying as it manifests itself as changes in the structural and energetic forms in the preliminary results.

The calculations show that the tetragonal forms of alloys are strong candidates for future piezoelectric applications. They have much better piezoelectric properties than compared to their pure ABO_3 for.

The second main topic of this thesis presented a detailed investigation of the elastic and piezoelectric properties of ABO_3 type tetragonal perovskites using first-principle DFT computations with the GGA of PBE. Six independent ion-relaxed elastic constants and clamped-ion elastic constants are found to calculate ion-relaxed piezoelectric constants and clamped-ion piezoelectric constants. To compute properties based on the elastic constants indicate that ABO_3 type perovskites have satisfied the mechanical stability. It is essential to discuss the effect of the A-site and B-site configuration effect of ABO_3 type perovskites on piezoelectric properties. Some of the configurations have much better piezoelectric properties than the well-known conventional bulk piezoelectric materials for $Pb_xBa_{(1-x)}TiO_3$. If significant breakthroughs have been reported, many questions still remain. At the same time, the rest of the tetragonal form of ABO_3 perovskite structures and their geometries are unexplored. This may be investigated in future works. The calculated results show a factor one to two orders of magnitude larger than other configurations. The huge piezoelectric properties of these materials are expected to provide new platforms for electronic and piezotronic devices.

REFERENCES

[1] Curie, J. and Curie, P., (1880). “D´eveloppement, par pression, de l’´electricit´e polaire dans les cristaux h´emi`edres a faces inclin´ees, Compt. Rend. 91:294-295.

[2] Lippmann, G., (1881). “Principe de la conversation de l’´electricit´e”, Ann. de Chim. et de Phys. 24:145-178.

[3] Nye, J., (1985). Physical properties of crystals, Clarendon press.

[4] Ye, A.G., (2008). Handbook of Dielectric, Piezoelectric and Ferroelectric Materials, Woodhead Publishing, Cambridge.

[5] Uchino, K., (2015). “Glory of piezoelectric perovskites”, Sci. Technol. Adv. Mater., 16(046001).

[6] Voigt, W., (1910). Lerbuch der Kristallphysik, Teubner, Leipzig-Berlin.

[7] Innovative Research and Products (2010). Inc, ET112: Piezoelectric Actuators and Motors – Types, Applications, new developments, Industry Structure and Global Markets.

[8] Ye, Z.G., (2008). Handbook of dielectric, piezoelectric and ferroelectric materials, Woodheal Publishing, England.

[9] Gomez, E.S., (2010). Piezoelectric Ceramics, Sciyo Publishing, Rijeka, Cratio.

[10] Tichy, J., Erhart, J., Kittinger, E., and Privratska, J., (2010). Fundamentals of piezoelectric sensorics, Springer- Verlag Berlin Heidelberg.

[11] Yang, J., (2005). An introduction to the theory of piezoelectricity, Springer Science + Business Media, Boston.

[12] Hewat, A.W., (1974). Ferroelectrics 6:215.

[13] Guyton Candy, W., (1946). Piezoelectricty, New York, McGraw-Hill Book Company, 117-159.

[14] Lines, M.E., and Glass, A.M., (1977). Principle and Applications of Ferroelectrics and Related Materials, Clarendon, Oxford.

[15] Scott, J.F., (2000). Ferroelectric Memories, Springer-Verlag, Berlin.

[16] Rohrer, G.S., and Affatigato, M., (2012). “Challenges in Ceramic Science: A report from the workshop on emerging research areas in ceramic science” J. Ame. Ceram. Soc., 95:3699-3712.

[17] Ok, K.M., Chi, E.O. and Halasyamani, P.S., (2006). “Bulk characterization methods for non-centrosymmetric materials: second-harmonic generation, piezoelectrcity, pyroelectricty, and ferroelectricity”, Chem. Soc. Rev., 35:710-717.

[18] Gupta, P., and Srivastava, R.K., (2010). “New Trends in Technologies: Devices, Computer and Industrial Systems, Overview of multi functional materials”, INTECH open access publisher.

[19] Freitag, R. and Conradie, J., (2013). “Understanding the Jahn–Teller Effect in Octahedral Transition-Metal Complexes: A Molecular Orbital View of the Mn(β-diketonato)$_3$ Complex”, J. Chem. Educ., 90:1692-1696.

[20] Fu, D., and Itoh, M., (2011). "Ferroelectricity in Silver Perovskite Oxides", arXiv, 1108-5819.

[21] Tidrow, S.C., (2014). "Mapping comparison of Goldschmidt’s tolerance factor with perovskite structural conditions", Ferroelectrics, 470(1):13-27.

[22] Johnsson, M., and Lemmens, P., (2005). "Crystallography and chemistry of perovskites",arXiv:cond-mat/0506606.

[23] Zimmerman, D., (2002). " Paul Langevin and the discovery of active sonar or asdic" North. Mariner 12:39–52.

[24] Cohen, R.E., and Krakauer, H., (1992). "Electronic structure studies of the differences in ferroelectric behavior of $BaTiO_3$ and $PbTiO_3$",Ferroelectrics, 136:65-83.

[25] Smith, R.D., and Vanderbilt, D., (1994). "First-principles investigation of ferroelectricity in perovskite compounds”, Phys.Rev. B 49:5828.

[26] Cora, R.F., and Catlow, C.R.A., (1999). Faraday Discuss, 144-421.

[27] Gonzalez-Garcia, A., Lopez-Perez, W., Palacio-Mozo, R., and Gonzalez-Hernandez, R., (2014). J. Comp. Mat. Sci. 91:279-284.

[28] Xie, M.Y., Tasnadi, F., Abrikosov, I.A., Hultman, L., and Darakchieva, V., (2012). Phys. Rev. B 86:155310.

[29] Qi, T., Grinberg, I., and Rappe, AM., (2010). “Correlations between tetragonality, polaization, and ionic displacement in $PbTiO_3$ – derived ferroelectric perovskite solid solutions ”, Phys. Rev. B, 82:134113.

[30] Bennett, J., Grinberg, I., Davies, P., and Rappe, A.M., (2011). “Pb-free ferroelectrics investigated with density functional theory: SnAl1/2Nb1/2O3 perovskites”, Phys. Rev. B 83(144112):1-6.

[31] Halilov, S.V., Fornari, M., and Singh, D.J., (2002) “Lattice instabilities in (Pb,Cd)TiO_3 alloys” Applied Phys. Let. 81(18):3443-3445.

[32] Erba, A., El-Kelany, K.E., Ferrero, M., Baraille, and I., Rerat, M., (2013). “Piezoelectricity of SrTiO3: An ab initio description”, Phys. Rev. B., 88:035102.

[33] Jong, M., Chen, W., Geerlings, H., Asta, M., and Persson, K.K, (2015). “A database to enable discovery and design of piezoelectric materials”, Scientific Data 2:150053.

[34] Reed, E.J., (2015). “Piezoelectricity: Now in two dimensions”, Natur. Nanotec. 10:106-107.

[35] Shi, J., Grinberg, I., Wang, X., Rappe, A.M., (2014). "Atomic sublattice decomposition of piezoelectric response in tetragonal $PbTiO_3$, $BaTiO_3$, and $KNbO_3$", Phys. Rev. B., 89(094105).

[36] Mahmoud, A., Erba, A., El-Kelany, Kh. E., Rerat, M., and Orlando, R., (2014). "Low-Temperature Phase of BaTiO3: Piezoelectricity, Dielectric, Elastic, and Photoelastic Properties from ab Initio Simulations", Phys. Rev. B., 89(045103).

[37] Kim S.M., Lee, W., Cho, Y.H., Shim, and M., Kim, S., (2013). "Piezoelectricity in PbZrxTi1-xO3 Studied by Density-Functional Perturbation Theory Supercell Calculations", Phys. Rev. B., 89(045103).

[38] Kresse, G., Marsman, M., and Furtmuller, J., (2015). "Vienna Ab-initio Simulation Package", Proceedings of the TMS Middle East, Wien, Austria.

[39] Yao, H., Quyang, L., and Ching, W.Y., (2007). "Ab iitio calculation of elastic constants of ceramic crystals", Ame. Ceram. Soc. 90:3194-3204.

[40] Jain, A., Ong, S.P., Hautier, G., Chen, W., Richards, W.D., Dacek, S., Cholia, S., Gunter, D., Skinner D., Ceder, G., and Persson, K.A., (2013). "The Materials Project: A materials genome approach to accelerating materials innovation", APL Materials, 1(011002).

[41] Geerlings, P., Proft, F., Hautier, and Langenaeker, W., (2003). "Conceptual Density Functional Theory", Chem. Rev., 103:1793-1874.

[42] Ghosezs, P., and Junquera, J., (2006). First-principle modeling of ferroelectric oxides nanostructures, Amer. Sci. Publisher, Stevenson Rach, CA, USA.

[43] Eschrig, H., and Junquera, J., (2003). The fundamentals of Density Functional Theory, Amer. Sci. Publisher, Stevenson Rach, CA, USA.

[44] Stein, D.M., (2011). Structure and properties of Bi-containing mixed A-site perovskites, Ph.D. thesis, University of Pennsylvania.

[45] Chatterjee, A., (2010). Structure property correlations for nanoporous materials, CRC Press, USA.

[46] Tholander, C., (2014). "A theoretical study in piezoelectricty, phase stability and surface diffusion in disordered multcompnent nitrides", Linkoping Studies in Science and Techonology Ph.D Thesis No: 1675.

[47] Neese, B.P., (2009). Investigations of structure-property relationship to enhance the multifunctional properties of PVDF- based polymers, Pennsylvania State University Ph.D Thesis.

[48] Bousquet, E., (2009). First –principle study of ferroelectric oxide nanostructures, Universite de Liege, Ph.D Thesis.

[49] Hayn, S., (2013). First principles calculations on the structural and thermodynamic stability of $(Na_{0,5}Bi_{0.5},Ba)TiO_3$ and $Pb(Zr,Ti)O_3$, Technische Universitat Darmstadt, Ph.D Thesis.

[50] Sun Y, Thompson, S., and Nishida, T., (2010). Strain Effect in Semiconductors: Theory and Device Applications, Springer.

[51] Uludogan, M., Guarin, P.D., Gomez, Z.E., Cagin, T., and Goddard, W.A., (2008). "DFT Studies on Ferroelectric Ceramics and Their Alloys: $BaTiO_3$,

$PbTiO_3$, $SrTiO_3$, $AgNbO_3$, $AgTaO_3$, $Pb_xBa_{(1-x)}TiO_3$ and $Sr_xBa_{(1-x)}TiO_3$", CMES-Compt Modeling in Engineering & Sciences, 24(215):38.

[52] Wang, J.J., Meng, F.Y., Ma, X.Q., Xu, X., and Chen, L.Q., (2010). "Lattice, Elastic, Polarization and Electrostrictive Properties of $BaTiO_3$ from First-Principles", J. Appl. Phys., 108(3):034107.

[53] Rohrer, G., Affatigato, M., Backhaus, M., Bordia, R., and Scott Weil K., (2012). J. Am. Ceram. Soc., 95:3699-3712.

[54] Piskonov, S., Heifets, E., Eglitis, R.I., and Bornstel, G., (2004). "Bulk-Temperature and Electronic Structure of $SrTiO_3$, $BaTiO_3$, $PbTiO_3$ Perovskites an ab Initio HF/DFT Study", J. Comp. Mat. Sci. 29(2):165-178.

[55] Terki, R., Feraoun, H., Bertrand, G., and Aourag, H., (2005). "Full Potential Calculation of Structural, Elastic and Electronic Properties of $BaZrO_3$ and $SrZrO_3$, Physica Status Solidi B", 242(5):1054-1062.

[56] Sciau, Ph., Kania, A., Dkhil, B., Suard, E., and Ratuzna, A., (2004). "Structural Investigation of Ag NbO3 Phases Using X-Ray and Neutron Diffraction", J. of Physics: Condensed Matter, 16(16):2795.

[57] Li, Z., Grimsditch, M., Foster, C.M., and Chan, S.K., (1996). "Dielectric and Elastic Properties of Ferroelectric Materials at Elevated Temperature", J. Phys. Chem. of Solids, 57(10):1433-1438.

[58] Ravindran, P., Fast, L., Korzhavyi, P.A., Johansson, B., Wills, J., and Eriksson, O., (1998). "Density Functional Theory for Calculation of Elastic Properties of Orthorhombic Crystals: Application to $TiSi_2$", J. Appl. Phys., 84(9):4891-4904.

[59] Bellaiche, L., Padilla, J., and Vanderbilt, D., (1998). "Heterovalent and A-atom effects in $A(B'B)O_3$ Perovskite Alloys", Phys. Rev. B. 59.

[60] Bell, R.O., and Rupprecht, G., (1963). "Elastic Constants of Strontium Titanate", Phys. Rev., 129(90).

[61] Cao, L., Sozontov, E., and Zegenhagen, J., (2000)."Cubic to Tetragonal Phase Transition of SrTiO3 under Epitaxial Stress: An X-Ray Backscattering Study, Physica status solidi" 181(2):387-404.

[62] Duan, Y., Tang, G., Chen, C., Li, T., and Wu, Z., (2012). "First-Principles Investigations of Ferroelectricity and piezoelectricity in BaTiO3/PbTiO3 Superlattices", Phys. Rev. B 85:054108.

[63] Kalay, M., Kart, H.H., Ozdemir Kart, S., and Cagin, T., (2009). "Elastic Properties and Pressure Induced Transitions of ZnO Polymorphs from First-Principle Calculations", J. Alloys Comp. 484:431-438.

[64] Anton, S.R., and Sodano H., (2007). "A review of power harvesting using piezoelectric as smart materials", Smart. Mater. Struct. 16:1- 21.

[65] Alyoruk, M.M., Airken, Y., Cakir, D., Peeters, F.M., and Sevik C., (2015). "Promising Piezoelectric Performance of Single Layer Transition-Metal Dichalcogenides and Dioxides", J. Phys. Chem. C. 119:23231-23237.

[66] Bennett, J., Grinberg, I., Davies, P., and Rappe, A.M., (2011). "Pb-free ferroelectrics investigated with density functional theory: SnAl1/2Nb1/2O3 perovskites", Phys. Rev. B 83, 144112:1-6.

[67] Calle- Vallejo, F., Martinez, J.I., Garcia – Lastra, J. M., Mogensen, M., and Rossmeisl, J., (2010). "Density Functional Studies of Functionalized Graphitic Materials with Late Transition Metals for Oxygen Reduction Reactions", Angew. Chem. Int. Ed., 49:1-4.

[68] Chervin, J.C., Itie, J.P., Gourdain, D., and Pruzan, Ph., (1999). "Energy Dispersive X-Ray Diffraction Study of KnBO3 up to 19 GPa at Room Temperature", Solid State Communications 110:247-251.

[69] Duerloo, K-A.N., Ong, M.T., and Reed, E., (2012). "Intrinsic Piezoelectricity in Two-Dimensional Materials", J. Phys. Chem. Lett., 3:2871-2876.

[70] Damjanovic, D., (2001). "Piezoelectric properties of perovskite ferroelectrics: unsolved problems and future research", Ann. Chim. Sci. Mat., 99-106.

[71] Erdem I., Kart H.H., and Cagin T., (2014). "High Pressure Phase Transitions in SnO2 Polymorphs by First Calculations", J. Alloys Comp., 587:638-645.

[72] Erba, A., El-Kelany, K.E., Ferrero, M., Baraille, I., and Rerat, M., (2013). "Piezoelectricity of SrTiO3: An ab initio description", Phys. Rev. B., 88:035102.

[73] Fontana, M.D., Metrat, G., Servoin, J.L., and Gervais, F., (1984). "Infrared Spectroscopy in KNbO3 though the Successive Ferroelectric Phase Transitions", J. Phys. C: Solid State Phys., 17:483.

[74] Fei, R., Li, W., Li, J., and Yang, L., (2015). "Giant Piezoelectricity of Monolayer Group IV Monochalcogenides; SnSe, SnS, GeSe and GeS", Appl. Phys. Lett., 107:173104.

[75] Guo, R., Cross, L.E., Park, S-E., Noheda, B., Cox, D.E., and Shirane, (2000). "Origin of the High Piezoelectricity Response in PbZr1-xTixO3, G"., Phys. Rev. Lett., 84:5423.

[76] Majdoub, M.S., Sharma, P., and Cagin, T., (2008). "Dramatic Enhancement in Energy Harvesting for a Narrow Range of Dimensions in Piezoelectric Nanostructures", Phys. Rev. B., 78:121407.

[77] Wu, W., Wang, L., Li, Y., Zhang, F., Lin, L., Niu, S., Chenet, D., Zhang, X., Hao, Y., Heinz, T.F., Hone, J., and Wang, Z.L., (2014). "Piezoelectricity of Single-Atomic Layer MoS2 for Energy Conversion and Piezotronics", Nature 514:470-474.

[78] Kholkin, A., Pertsev, N.A., and Goltsev, A.V., (2008). "Piezoelectric and Acoustic Materials for Transducer Application".

[79] Li, W., and Li, J., (2015). "Piezoelectricity in Two Dimensional Group III Monochalcogenides", Nano Research., 8(12):3796-3802.

[80] Yamanaka, S., Fujikane, H., Hamaguchi, T., Muta, H., Oyama, T., Matsuda, T., Kobayashi, S., and Kurosaki, K., (2003), J. Alloys and Compd. 359(109).

[81] Zhu, H., Wang, Y., Xiao, J., Liu, M., Xiang, S., Wang, Z.J., Ye, Z., Ye, Y., Yin, X., and Zhang, X., (2015). "Observation of Piezoelectricity in Free-Standing Monolayer MoS2", Nature Nanotech. 10:151-155.

[82] Waser, R., (2003). "Nanoelectronics and Information Technology, Advanced Electronic Materials and Novel Devices", Wiley- VCH, Weinhaim.

[83] Lebedev, A.I., (2009). “Ab Initio Calculations of Phonon Spectra in ATiO3 Perovskite Crystals (A=Ca, Sr, Ba, Ra, Cd, Zn, Mg, Ge, Sn, Pb)”, Phys. of Solid State, 51:362-372.

[84] Wu, X., Vanderbilt, D., and Hamaann, D.R., (2005). “Systematic treatment of displacements, strains, and electric fields in density-functional perturbation theory”, Phys. Rev. B., 72(035105).

[85] Ghosez, P., Gonze, X., and Michenaud, J.P., (1999). “Lattice dynamics of BaTiO3, PbTiO3, and PbZrO3: A comparative first-principles study”, Phys. Rev. B., 60: 836-843.

[86] Landolt, H., and Bornstein, R., (1996). Numerical Data and Functional Relationship in Science and Technology, Springer, Berlin.

[87] Zhong, W., King-Smith, R.D., and Vanderbilt, D., (1993). “Giant LO-TO Splittings in Perovskite Ferroelectrics”, Phy. Rev. Letters, 72(22).

[88] R-Marcos, F., Marchet, P., M-Mejean, T., and Fernandez, J.F., (2008). “Importance of the crystalline symmetry in the piezoelectric properties of lead-free ceramics, arXiv:0808.0115.

[89] Sawaguchi, E., (1953). “Ferroelectricity Versus Anti- Ferroelectricity in the Solid Solutions of $PbZrO_3$ and $PbTiO_3$”, J.Phys.Soc., Japan, 8:615-629.

[90] Kennedy, B J., Howard, C.J., and Chakooumakos, B.C., (1999). “High-Temperature Phase Transitions in $SrZrO_3$”, Phys. Rev. B., 59(6):4023.

[91] Ghosez, Ph., Gonze, X., Lambin, Ph., and Michenaud, J.P., (1994). “Born effective charges of barium titanate: Band by ban decomposition ans sensitivity to structural features”, Phys. Rev. B, 51(10).

[92] Roy, A., Prasad, R., Auluck, S. and Garg, A. (2010). “First –principle calculation of Born effective charges and spontaneous polarization of ferroelectric bismuth”, Jour. of Pyhs. Conden. Mat. 22(16):165902.

[93] Posternak, M., Resta, R. and Baldereschi, A., (1994). “Role of covalent bonding in the polarization of perovskite oxides: The case of $KNbO_3$ ”, Phys. Rev. B 50(8911).

[94] Born, M., and Goopert-Mayer, M., (1933). Handbuch Physik 24(623).

[95] Nemoshkalenko, V.V., and Timoshevski, A.N., (1985). “The peculiarities of the electronic structure of $BaTiO_3$ in the $ATiO_3$ (A=Ca, Sr,Ba) series”, Phys. Stat. Sol. B, 127-163.

[96] Qi, T., Grinberg, I., and Rappe, AM., (2010). “Correlations between tetragonality, polaization, and ionic displacement in $PbTiO_3$-derived ferroelectric perovskite solid solutions ”, Phys. Rev. B, 82:134113.

[97] Li, H., Yao, P., Ong, K.P., Wu, P., and Wang, J., (2012). “Origin of a tetragonal $BiFeO_3$ phase with a giant c/a ratio on $SrTiO_3$ substrates”, Adv. Funct. Mater. 22:937-942.

[98] Lee, J.G., (2012). Computational Material Science An Introduction, CRC Press, Taylor&Francis Group, Boca Raton, FL, USA.

[99] Berlincourt, D., and Jaffe, H., (1958), “Elastic and Piezoelectric coefficients of single-crsytal Barium Titanate”, Phys. Rev. 111-143.

[100] Bell, RO. and Rupprecht, G., (1963), “Elastic Constants of Strontium Titanate”, Phys. Rev. 129(90).

[101] Herter, P., (2008), “Lecture on Theoretical Physics”, Dielectric Waveguides 16-19.

[102] Kanaun, S., (2011). “An Efficient Numerical Method for Calculation of Elastic and Thermo-Elastic Fields in a Homogeneous Medium with Several Heterogeneous Inclusions”, World Jour. of Mech. 1:31-43.

[103] Momma, K., and Izumi, F., (2011). “VESTA 3 for three-dimensional visualization of crsytal, volumetric and morphology data”, J. Appl. Cryst, 44:1271-1276.

[104] Hinchliffe, A., (2008). Molecular Modelling for Beginners, Wiley and Sons Publication.

APPENDIX-A

SUPPLEMENTARY MATERIALS

a. Full Elastic Constants of ABO_3 Alloys

Table A.1 The calculated elastic constants of SPT

	C_{11}	C_{12}	C_{44}	C_{13}	C_{33}	C_{66}
$Sr_8Ti_8O_{24}$	316.47	99.33	108.44	-	-	-
$Sr_7Pb_1Ti_8O_{24}$	311.43	103.70	105.54	-	-	-
$Sr_6Pb_2Ti_8O_{24}$ [a]	309.45	105.51	104.20	109.62	312.05	103.07
$Sr_6Pb_2Ti_8O_{24}$ [b]	303.94	109.59	104.93	-	-	-
$Sr_6Pb_2Ti_8O_{24}$ [c]	309.06	111.89	104.46	105.37	304.57	102.70
$Sr_5Pb_3Ti_8O_{24}$ [a]	307.70	111.50	102.13	109.31	302.12	100.30
$Sr_5Pb_3Ti_8O_{24}$ [b]	300.79	108.06	101.51	117.54	290.38	103.20
$Sr_5Pb_3Ti_8O_{24}$ [c]	305.26	109.49	100.42	-	-	-
$Sr_4Pb_4Ti_8O_{24}$ [a]	306.41	112.62	101.72	111.21	300.68	77.98
$Sr_4Pb_4Ti_8O_{24}$ [b]	274.06	108.43	100.73	136.49	300.22	102.42
$Sr_4Pb_4Ti_8O_{24}$ [c]	302.49	111.99	100.55	-	-	-
$Sr_4Pb_4Ti_8O_{24}$ [d]	293.36	110.60	100.66	121.89	289.98	101.01
$Sr_4Pb_4Ti_8O_{24}$ [e]	299.99	115.65	99.79	108.93	300.64	100.23
$Sr_4Pb_4Ti_8O_{24}$ [f]	303.55	111.12	95.98	-	-	-
$Sr_3Pb_5Ti_8O_{24}$ [a]	257.85	152.61	99.15	116.22	292.63	96.96
$Sr_3Pb_5Ti_8O_{24}$ [b]	278.43	109.91	99.44	134.13	290.00	98.70
$Sr_3Pb_5Ti_8O_{24}$ [c]	297.21	116.65	99.38	-	-	-
$Sr_2Pb_6Ti_8O_{24}$ [a]	288.48	116.07	98.69	124.29	298.21	97.11
$Sr_2Pb_6Ti_8O_{24}$ [b]	292.27	118.30	100.07	-	-	-
$Sr_2Pb_6Ti_8O_{24}$ [c]	295.90	115.16	97.67	115.10	295.23	97.51
$Sr_1Pb_7Ti_8O_{24}$	289.91	125.09	96.53	-	-	-
$Pb_8Ti_8O_{24}$	287.67	119.05	96.94	-	-	-

Table A.2 The calculated elastic constants of PBT

	C_{11}	C_{12}	C_{44}	C_{13}	C_{33}	C_{66}
$Pb_8Ti_8O_{24}$	287.67	119.05	96.94	-	-	-
$Pb_7Ba_1Ti_8O_{24}$	287.45	120.02	91.71	-	-	-
$Pb_6Ba_2Ti_8O_{24}$ [a]	285.18	120.61	102.28	118.87	294.48	101.17
$Pb_6Ba_2Ti_8O_{24}$ [b]	289.51	123.01	102.12	-	-	-
$Pb_6Ba_2Ti_8O_{24}$ [c]	287.78	120.24	103.01	118.16	291.18	101.42
$Pb_5Ba_3Ti_8O_{24}$ [a]	284.18	116.95	105.37	116.15	288.19	104.84
$Pb_5Ba_3Ti_8O_{24}$ [b]	280.44	115.31	104.91	119.98	280.44	105.68
$Pb_5Ba_3Ti_8O_{24}$ [c]	285.54	117.17	105.43	-	-	-
$Pb_4Ba_4Ti_8O_{24}$ [a]	287.67	122.20	108.32	114.52	285.61	106.74
$Pb_4Ba_4Ti_8O_{24}$ [b]	275.79	111.80	107.78	119.26	275.79	109.29
$Pb_4Ba_4Ti_8O_{24}$ [c]	281.88	115.39	107.79	-	-	-
$Pb_4Ba_4Ti_8O_{24}$ [d]	295.49	119.08	107.82	123.21	278.59	107.26
$Pb_4Ba_4Ti_8O_{24}$ [e]	296.26	121.65	107.97	114.68	284.15	108.20
$Pb_4Ba_4Ti_8O_{24}$ [f]	296.63	124.38	108.00	-	-	-
$Pb_3Ba_5Ti_8O_{24}$ [a]	294.52	123.77	111.30	120.63	292.82	110.20
$Pb_3Ba_5Ti_8O_{24}$ [b]	292.05	116.43	110.62	126.06	285.01	111.40
$Pb_3Ba_5Ti_8O_{24}$ [c]	290.40	119.43	111.01	-	-	-
$Pb_2Ba_6Ti_8O_{24}$ [a]	287.09	114.31	114.86	114.21	290.26	113.62
$Pb_2Ba_6Ti_8O_{24}$ [b]	280.11	111.58	112.89	-	-	-
$Pb_2Ba_6Ti_8O_{24}$ [c]	285.01	114.34	114.31	114.26	291.97	113.69
$Pb_1Ba_7Ti_8O_{24}$	284.76	109.84	116.68	-	-	-
$Pb_8Ti_8O_{24}$	287.67	119.05	96.94	-	-	-

Table A.3 The calculated elastic constants of SBT

	C_{11}	C_{12}	C_{44}	C_{13}	C_{33}	C_{66}
$Sr_8Ti_8O_{24}$	316.47	99.33	108.44	-	-	-
$Sr_7Ba_1Ti_8O_{24}$	312.95	102.48	105.97	-	-	-
$Sr_6Ba_2Ti_8O_{24}$ [a]	310.35	104.72	111.28	107.12	309.73	109.79
$Sr_6Ba_2Ti_8O_{24}$ [b]	307.77	103.81	110.35	-	-	-
$Sr_6Ba_2Ti_8O_{24}$ [c]	307.19	105.05	111.18	102.75	308.41	110.33
$Sr_5Ba_3Ti_8O_{24}$ [a]	304.01	105.46	112.88	103.26	302.85	111.89
$Sr_5Ba_3Ti_8O_{24}$ [b]	300.75	102.34	111.83	105.46	300.75	112.29
$Sr_5Ba_3Ti_8O_{24}$ [c]	305.64	105.47	112.80	-	-	-
$Sr_4Ba_4Ti_8O_{24}$ [a]	300.14	108.16	115.38	103.54	299.76	113.59
$Sr_4Ba_4Ti_8O_{24}$ [b]	298.96	103.00	114.09	108.41	298.96	114.86
$Sr_4Ba_4Ti_8O_{24}$ [c]	306.42	106.49	115.85	-	-	-
$Sr_4Ba_4Ti_8O_{24}$ [d]	298.17	104.09	113.51	103.40	294.91	113.30
$Sr_4Ba_4Ti_8O_{24}$ [e]	301.57	105.63	113.43	105.63	295.51	113.43
$Sr_4Ba_4Ti_8O_{24}$ [f]	301.14	106.02	113.94	-	-	-
$Sr_3Ba_5Ti_8O_{24}$ [a]	294.50	106.94	115.94	105.64	295.32	115.26
$Sr_3Ba_5Ti_8O_{24}$ [b]	294.98	104.36	115.45	108.42	294.98	115.57
$Sr_3Ba_5Ti_8O_{24}$ [c]	296.71	106.71	115.62	-	-	-
$Sr_2Ba_6Ti_8O_{24}$ [a]	290.33	105.15	117.81	105.86	290.71	116.01
$Sr_2Ba_6Ti_8O_{24}$ [b]	290.34	105.90	116.38	-	-	-
$Sr_2Ba_6Ti_8O_{24}$ [c]	291.14	107.64	117.27	103.67	288.18	116.64
$Sr_1Ba_7Ti_8O_{24}$	286.74	105.69	119.04	-	-	-
$Ba_8Ti_8O_{24}$	281.67	104.23	119.63	-	-	-

Table A.4 The calculated elastic constants of PZT

	C_{11}	C_{12}	C_{44}	C_{13}	C_{33}	C_{66}
$Pb_8Zr_8O_{24}$	303.12	85.13	61.48	-	-	-
$Pb_8Zr_7Ti_1O_{24}$	300.44	86.23	63.01	-	-	-
$Pb_8Zr_6Ti_2O_{24}$ [a]	300.65	88.79	65.61	88.94	297.69	65.73
$Pb_8Zr_6Ti_2O_{24}$ [b]	299.86	91.45	66.62	-	-	-
$Pb_8Zr_6Ti_2O_{24}$ [c]	298.64	90.71	67.11	90.22	300.51	65.92
$Pb_8Zr_5Ti_3O_{24}$ [a]	296.42	92.04	69.44	91.38	300.55	68.46
$Pb_8Zr_5Ti_3O_{24}$ [b]	299.06	94.27	69.51	95.48	296.39	70.09
$Pb_8Zr_5Ti_3O_{24}$ [c]	298.29	96.07	70.65	-	-	-
$Pb_8Zr_4Ti_4O_{24}$ [a]	293.59	94.13	73.23	93.32	302.50	72.99
$Pb_8Zr_4Ti_4O_{24}$ [b]	301.35	98.51	73.45	102.76	291.01	76.03
$Pb_8Zr_4Ti_4O_{24}$ [c]	296.44	101.84	76.53	-	-	-
$Pb_8Zr_4Ti_4O_{24}$ [d]	294.90	95.47	73.47	94.18	295.73	70.84
$Pb_8Zr_4Ti_4O_{24}$ [e]	299.67	98.68	74.39	97.80	294.77	74.10
$Pb_8Zr_4Ti_4O_{24}$ [f]	297.43	96.52	73.11	-	-	-
$Pb_8Zr_3Ti_5O_{24}$ [a]	288.23	93.15	74.09	92.97	291.74	50.61
$Pb_8Zr_3Ti_5O_{24}$ [b]	296.53	100.72	75.93	103.12	290.09	73.66
$Pb_8Zr_3Ti_5O_{24}$ [c]	294.03	102.97	51.56	-	-	-
$Pb_8Zr_2Ti_6O_{24}$ [a]	289.44	103.58	82.78	104.30	295.47	69.69
$Pb_8Zr_2Ti_6O_{24}$ [b]	295.29	108.40	84.23	-	-	-
$Pb_8Zr_2Ti_6O_{24}$ [c]	293.62	106.91	75.32	105.62	292.01	69.30
$Pb_8Zr_1Ti_7O_{24}$	292.29	110.67	87.34	-	-	-
$Pb_8Ti_8O_{24}$	287.67	119.05	96.94	-	-	-

Table A.5 The calculated elastic constants of BZT

	C_{11}	C_{12}	C_{44}	C_{13}	C_{33}	C_{66}
$Ba_8Zr_8O_{24}$	293.18	77.61	82.06	-	-	-
$Ba_8Zr_7Ti_1O_{24}$	292.21	78.90	84.52	-	-	-
$Ba_8Zr_6Ti_2O_{24}$ [a]	291.73	80.73	87.82	81.46	290.36	87.65
$Ba_8Zr_6Ti_2O_{24}$ [b]	290.94	82.99	88.81	-	-	-
$Ba_8Zr_6Ti_2O_{24}$ [c]	289.91	83.19	88.45	82.32	291.42	87.65
$Ba_8Zr_5Ti_3O_{24}$ [a]	288.75	83.80	91.68	83.81	291.15	91.13
$Ba_8Zr_5Ti_3O_{24}$ [b]	289.54	84.71	92.16	86.46	289.54	92.69
$Ba_8Zr_5Ti_3O_{24}$ [c]	288.51	86.94	91.93	-	-	-
$Ba_8Zr_4Ti_4O_{24}$ [a]	287.84	85.85	95.59	86.72	292.30	95.08
$Ba_8Zr_4Ti_4O_{24}$ [b]	290.72	88.39	96.81	92.43	284.89	98.87
$Ba_8Zr_4Ti_4O_{24}$ [c]	286.61	91.97	96.70	-	-	-
$Ba_8Zr_4Ti_4O_{24}$ [d]	287.54	88.11	96.42	87.01	289.17	95.43
$Ba_8Zr_4Ti_4O_{24}$ [e]	289.98	89.78	96.78	88.69	287.17	96.37
$Ba_8Zr_4Ti_4O_{24}$ [f]	288.00	87.50	95.49	-	-	-
$Ba_8Zr_3Ti_5O_{24}$ [a]	287.08	90.48	100.74	90.82	287.38	100.44
$Ba_8Zr_3Ti_5O_{24}$ [b]	288.57	91.36	101.38	93.78	283.63	102.40
$Ba_8Zr_3Ti_5O_{24}$ [c]	286.61	93.60	101.62	-	-	-
$Ba_8Zr_2Ti_6O_{24}$ [a]	286.88	93.77	106.12	94.95	284.92	106.63
$Ba_8Zr_2Ti_6O_{24}$ [b]	285.61	95.59	107.71	-	-	-
$Ba_8Zr_2Ti_6O_{24}$ [c]	286.23	96.06	107.43	94.92	282.21	106.60
$Ba_8Zr_1Ti_7O_{24}$	283.71	98.23	112.78	-	-	-
$Ba_8Ti_8O_{24}$	281.67	104.23	119.63	-	-	-

Table A.6 The calculated elastic constants of SZT

	C_{11}	C_{12}	C_{44}	C_{13}	C_{33}	C_{66}
$Sr_8Zr_8O_{24}$	315.37	71.57	70.37	-	-	-
$Sr_8Zr_7Ti_1O_{24}$	315.49	72.60	71.81	-	-	-
$Sr_8Zr_6Ti_2O_{24}$ [a]	315.74	74.29	75.79	74.57	314.02	75.35
$Sr_8Zr_6Ti_2O_{24}$ [b]	315.43	76.74	76.71	-	-	-
$Sr_8Zr_6Ti_2O_{24}$ [c]	314.40	76.58	74.79	75.76	315.81	73.71
$Sr_8Zr_5Ti_3O_{24}$ [a]	313.29	77.05	79.36	76.62	316.26	78.51
$Sr_8Zr_5Ti_3O_{24}$ [b]	315.41	78.60	79.43	79.91	313.45	78.81
$Sr_8Zr_5Ti_3O_{24}$ [c]	314.59	80.73	76.48	-	-	-
$Sr_8Zr_4Ti_4O_{24}$ [a]	314.19	80.28	83.69	80.33	320.26	81.89
$Sr_8Zr_4Ti_4O_{24}$ [b]	318.19	82.72	84.53	85.67	310.88	85.97
$Sr_8Zr_4Ti_4O_{24}$ [c]	314.89	86.20	80.11	-	-	-
$Sr_8Zr_4Ti_4O_{24}$ [d]	314.83	82.18	84.01	81.06	316.54	83.06
$Sr_8Zr_4Ti_4O_{24}$ [e]	317.97	83.83	82.79	83.83	314.33	83.01
$Sr_8Zr_4Ti_4O_{24}$ [f]	315.46	81.60	81.98	-	-	-
$Sr_8Zr_3Ti_5O_{24}$ [a]	315.29	84.96	88.31	85.06	317.43	87.40
$Sr_8Zr_3Ti_5O_{24}$ [b]	318.39	86.53	88.73	88.68	312.38	89.22
$Sr_8Zr_3Ti_5O_{24}$ [c]	313.91	86.49	87.02	-	-	-
$Sr_8Zr_2Ti_6O_{24}$ [a]	318.94	89.00	93.79	90.67	314.16	93.59
$Sr_8Zr_2Ti_6O_{24}$ [b]	317.91	91.62	95.30	-	-	-
$Sr_8Zr_2Ti_6O_{24}$ [c]	317.58	91.75	94.23	90.44	314.17	93.38
$Sr_8Zr_1Ti_7O_{24}$	317.15	93.99	100.34	-	-	-
$Sr_8Ti_8O_{24}$	316.47	99.33	108.44	-	-	-

b. Equation of State Parameters of ABO_3 compounds

Table A.7 The calculated structural properties of SPT

		V_0 (Å^3)	B(GPa)	B_0'	Lattice parameter(Å)	c/a
SPT	$Sr_7Pb_1Ti_8O_{24}$	61.33	172.26	4.45	3.941	1.0000
	$Sr_6Pb_2Ti_8O_{24}$ [a]	61.45	171.91	4.43	a=c=3.945, b=3.942	1.0009
	$Sr_6Pb_2Ti_8O_{24}$ [b]	61.45	171.91	4.43	3.943	1.0000
	$Sr_6Pb_2Ti_8O_{24}$ [c]	61.45	171.91	4.43	a=b=3.943, c=3.951	1.0022
	$Sr_5Pb_3Ti_8O_{24}$ [a]	61.55	172.55	4.44	a=b=3.945, c=3.950	1.0013
	$Sr_5Pb_3Ti_8O_{24}$ [b]	61.56	172.55	4.44	a=c=3.947, b=3.949	1.0006
	$Sr_5Pb_3Ti_8O_{24}$ [c]	61.56	172.71	4.44	3.947	1.0000
	$Sr_4Pb_4Ti_8O_{24}$ [a]	61.55	173.19	4.45	a=b=3.949, c=3.954	1.0012
	$Sr_4Pb_4Ti_8O_{24}$ [b]	61.66	173.19	4.45	a=c=3.950, b=3.952	1.0005
	$Sr_4Pb_4Ti_8O_{24}$ [c]	61.66	173.35	4.45	3.950	1.0000
	$Sr_4Pb_4Ti_8O_{24}$ [d]	61.66	173.19	4.45	a=c=3.951, b=3.950	1.0001
	$Sr_4Pb_4Ti_8O_{24}$ [e]	61.67	173.03	4.41	b=c=3.949, a=3.953	1.0010
	$Sr_4Pb_4Ti_8O_{24}$ [f]	61.66	173.19	4.45	3.951	1.0000
	$Sr_3Pb_5Ti_8O_{24}$ [a]	61.76	173.96	4.46	a=b=3.952, c=3.953	1.0002
	$Sr_3Pb_5Ti_8O_{24}$ [b]	61.76	173.99	4.46	a=c=3.951, b=3.954	1.0006
	$Sr_3Pb_5Ti_8O_{24}$ [c]	61.76	173.99	4.46	3.952	1.0000
	$Sr_2Pb_6Ti_8O_{24}$ [a]	61.86	174.64	4.47	a=c=3.954, b=3.952	1.0005
	$Sr_2Pb_6Ti_8O_{24}$ [b]	61.87	174.64	4.47	3.955	1.0000
	$Sr_2Pb_6Ti_8O_{24}$ [c]	61.86	174.64	4.47	a=b=3.955, c=3.959	1.0010
	$Sr_1Pb_7Ti_8O_{24}$	61.96	175.27	4.48	3.955	1.000

Table A.8 The calculated structural properties of PBT

		V_0 (Å^3)	B	B_0'	a(Å)	c/a
PBT	$Pb_7Ba_1Ti_8O_{24}$	62.49	173.65	4.54	3.968	1.0000
	$Pb_6Ba_2Ti_8O_{24}$ [a]	62.93	171.48	4.57	a=c=3.976, b=3.979	1.0003
	$Pb_6Ba_2Ti_8O_{24}$[b]	62.93	172.57	4.51	3.976	1.0000
	$Pb_6Ba_2Ti_8O_{24}$[c]	62.94	171.96	4.54	a=b=3.976, c=3.975	1.0003
	$Pb_5Ba_3Ti_8O_{24}$[a]	63.37	169.66	4.58	a=b=3.987, c=3.981	1.0013
	$Pb_5Ba_3Ti_8O_{24}$[b]	63.37	170.35	4.54	a=c=3.985, b=3.984	1.0004
	$Pb_5Ba_3Ti_8O_{24}$[c]	63.39	170.32	4.55	3.986	1.0000
	$Pb_4Ba_4Ti_8O_{24}$[a]	63.83	167.87	4.57	a=b=4.002, c=3.988	1.0034
	$Pb_4Ba_4Ti_8O_{24}$[b]	63.81	169.25	4.51	a=c=3.996, b=3.998	1.0004
	$Pb_4Ba_4Ti_8O_{24}$[c]	63.84	169.26	4.51	4.003	1.0000
	$Pb_4Ba_4Ti_8O_{24}$[d]	63.81	168.36	4.56	a=c=3.992, b=3.998	1.0015
	$Pb_4Ba_4Ti_8O_{24}$[e]	63.82	168.78	4.54	b=c=3.995, a=3.991	1.0008
	$Pb_4Ba_4Ti_8O_{24}$[f]	63.83	167.84	4.57	3.994	1.0000
	$Pb_3Ba_5Ti_8O_{24}$[a]	64.26	166.68	4.57	a=b=4.005, c=4.001	1.0009
	$Pb_3Ba_5Ti_8O_{24}$[b]	64.25	167.24	4.54	a=c=4.004, b=4.002	1.0003
	$Pb_3Ba_5Ti_8O_{24}$[c]	64.27	167.25	4.54	4.005	1.0000
	$Pb_2Ba_6Ti_8O_{24}$[a]	64.69	165.43	4.56	a=c=4.010, b=4.016	1.0014
	$Pb_2Ba_6Ti_8O_{24}$[b]	64.69	166.06	4.52	4.018	1.0000
	$Pb_2Ba_6Ti_8O_{24}$[c]	64.70	165.77	4.54	a=b=4.016, c=4.011	1.0010
	$Pb_1Ba_7Ti_8O_{24}$	65.14	164.31	4.54	4.023	1.0000

Table A.9 The calculated structural properties of SBT

		V_0 (Å^3)	B(GPa)	B_0'	Lattice parameter(Å)	c/a
SBT	$Sr_7Ba_1Ti_8O_{24}$	61.78	169.55	4.43	3.951	1.0000
	$Sr_6Ba_2Ti_8O_{24}$ [a]	62.31	168.23	4.45	a=c=3.963, b=3.959	1.0009
	$Sr_6Ba_2Ti_8O_{24}$[b]	62.32	168.63	4.44	3.963	1.0000
	$Sr_6Ba_2Ti_8O_{24}$[c]	62.34	168.38	4.45	a=b=3.965, c=3.960	1.0011
	$Sr_5Ba_3Ti_8O_{24}$[a]	62.87	167.10	4.45	a=b=3.975, c=3.971	1.0012
	$Sr_5Ba_3Ti_8O_{24}$[b]	62.87	167.26	4.46	a=c=3.977, b=3.971	1.0015
	$Sr_5Ba_3Ti_8O_{24}$[c]	62.91	167.43	4.47	3.975	1.0000
	$Sr_4Ba_4Ti_8O_{24}$[a]	63.42	165.66	4.48	a=b=3.987, c=3.979	1.0018
	$Sr_4Ba_4Ti_8O_{24}$[b]	63.41	166.46	4.46	a=c=3.985, b=3.980	1.0010
	$Sr_4Ba_4Ti_8O_{24}$[c]	63.48	166.78	4.47	3.982	1.0000
	$Sr_4Ba_4Ti_8O_{24}$[d]	63.40	165.98	4.49	a=c=3.984, b=3.990	1.0016
	$Sr_4Ba_4Ti_8O_{24}$[e]	63.43	166.30	4.48	b=c=3.986, a=3.987	1.0003
	$Sr_4Ba_4Ti_8O_{24}$[f]	63.40	165.40	4.48	3.987	1.0000
	$Sr_3Ba_5Ti_8O_{24}$[a]	63.95	164.86	4.51	a=b=3.998, c=3.996	1.0004
	$Sr_3Ba_5Ti_8O_{24}$[b]	63.95	165.34	4.49	a=c=3.998, b=3.993	1.0013
	$Sr_3Ba_5Ti_8O_{24}$[c]	63.99	165.50	4.50	3.998	1.0000
	$Sr_2Ba_6Ti_8O_{24}$[a]	64.50	164.45	4.50	a=c=4.009, b=4.008	1.0002
	$Sr_2Ba_6Ti_8O_{24}$[b]	64.50	164.70	4.51	4.009	1.0000
	$Sr_2Ba_6Ti_8O_{24}$[c]	64.51	164.38	4.51	a=b=4.010, c=4.009	1.0002
	$Sr_1Ba_7Ti_8O_{24}$	65.04	163.58	4.54	4.022	1.0000

Table A.10 The calculated structural properties of BZT

		V_0 (Å^3)	B(GPa)	B_0'	Lattice parameter(Å)	c/a
BZT	$Ba_8Zr_7Ti_1O_{24}$	75.52	150.28	4.49	4.225	1.0000
	$Ba_8Zr_7Ti_1O_{24}$[a]	74.19	151.08	4.51	a=c=4.194, b=4.211	1.0041
	$Ba_8Zr_6Ti_2O_{24}$[b]	74.02	152.04	4.50	4.197	1.0000
	$Ba_8Zr_6Ti_2O_{24}$[c]	74.03	151.08	4.56	a=b=4.198, c=4.197	1.0002
	$Ba_8Zr_5Ti_3O_{24}$[a]	72.79	151.24	4.63	a=b=4.180, c=4.161	1.0045
	$Ba_8Zr_5Ti_3O_{24}$[b]	72.61	151.56	4.69	a=c=4.164, b=4.183	1.0046
	$Ba_8Zr_5Ti_3O_{24}$[c]	72.48	153.65	4.52	4.167	1.0000
	$Ba_8Zr_4Ti_4O_{24}$[a]	71.58	153.16	4.37	a=b=4.162, c=4.121	1.0100
	$Ba_8Zr_4Ti_4O_{24}$[b]	71.13	155.57	4.52	a=c=4.128, b=4.170	1.0103
	$Ba_8Zr_4Ti_4O_{24}$[c]	70.86	156.37	4.53	4.136	1.0000
	$Ba_8Zr_4Ti_4O_{24}$[d]	71.32	151.24	4.79	a=c=4.146, b=4.145	1.0002
	$Ba_8Zr_4Ti_4O_{24}$[e]	71.15	155.09	4.53	b=c=4.149, a=4.128	1.0052
	$Ba_8Zr_4Ti_4O_{24}$[f]	71.32	153.96	4.57	4.145	1.0000
	$Ba_8Zr_3Ti_5O_{24}$[a]	69.95	153.64	4.74	a=b=4.126, c=4.104	1.0053
	$Ba_8Zr_3Ti_5O_{24}$[b]	69.75	153.48	4.85	a=c=4.107, b=4.131	1.0058
	$Ba_8Zr_3Ti_5O_{24}$[c]	69.62	157.33	4.54	4.112	1.0000
	$Ba_8Zr_2Ti_6O_{24}$[a]	68.50	157.01	4.57	a=c=4.082, b=4.106	1.0059
	$Ba_8Zr_2Ti_6O_{24}$[b]	68.30	159.25	4.54	4.086	1.0000
	$Ba_8Zr_2Ti_6O_{24}$[c]	68.32	155.57	4.86	a=b=4.086, c=4.088	1.0005
	$Ba_8Zr_1Ti_7O_{24}$	66.97	160.85	4.57	4.059	1.0000

Table A.11 The calculated structural properties of SZT

		V_0 (Å^3)	B(GPa)	B_0'	Lattice parameter(Å)	c/a
SZT	$Sr_8Zr_7Ti_1O_{24}$	72.27	153.48	4.42	4.119	1.0000
	$Sr_8Zr_6Ti_2O_{24}$[a]	70.83	154.76	4.40	a=c=4.129, b=4.148	1.0005
	$Sr_8Zr_6Ti_2O_{24}$[b]	70.64	156.21	4.38	4.132	1.0000
	$Sr_8Zr_6Ti_2O_{24}$[c]	70.67	155.41	4.41	a=b=4.133, c=4.132	1.0003
	$Sr_8Zr_5Ti_3O_{24}$[a]	69.31	155.89	4.45	a=b=4.112, c=4.092	1.0048
	$Sr_8Zr_5Ti_3O_{24}$[b]	69.11	157.01	4.45	a=c=4.095, b=4.115	1.0048
	$Sr_8Zr_5Ti_3O_{24}$[c]	68.96	158.45	4.40	4.099	1.0000
	$Sr_8Zr_4Ti_4O_{24}$[a]	67.71	154.76	4.92	a=b=4.091, c=4.050	1.0102
	$Sr_8Zr_4Ti_4O_{24}$[b]	67.47	160.53	4.39	a=c=4.055, b=4.098	1.0106
	$Sr_8Zr_4Ti_4O_{24}$[c]	67.17	161.49	4.40	4.063	1.0000
	$Sr_8Zr_4Ti_4O_{24}$[d]	67.68	157.65	4.51	a=c=4.074, b=4.073	1.0002
	$Sr_8Zr_4Ti_4O_{24}$[e]	67.50	159.89	4.41	b=c=4.077, a=4.055	1.0054
	$Sr_8Zr_4Ti_4O_{24}$[f]	67.70	158.29	4.44	4.073	1.0000
	$Sr_8Zr_3Ti_5O_{24}$[a]	66.16	160.21	4.47	a=b=4.050 c=4.028	1.0055
	$Sr_8Zr_3Ti_5O_{24}$[b]	65.95	161.34	4.50	a=c=4.031, b=4.054	1.0057
	$Sr_8Zr_3Ti_5O_{24}$[c]	65.79	162.94	4.42	4.035	1.0000
	$Sr_8Zr_2Ti_6O_{24}$[a]	64.53	163.74	4.44	a=c=4.001 b=4.025	1.0059
	$Sr_8Zr_2Ti_6O_{24}$[b]	64.31	165.66	4.41	4.004	1.0000
	$Sr_8Zr_2Ti_6O_{24}$[c]	64.35	164.22	4.49	a=b=4.050 c=4.070	1.0049
	$Sr_8Zr_1Ti_7O_{24}$	62.82	167.74	4.43	3.973	1.0000

b. Dielectric Constants Parameters of ABO_3 compounds

Table A.12 The calculated dielectric constants of SPT

	ε_{11}	ε_{22}	ε_{33}
$Sr_8Ti_8O_{24}$	6.3989	6.3989	6.3989
$Sr_7Pb_1Ti_8O_{24}$	6.6348	6.6348	6.6348
$Sr_6Pb_2Ti_8O_{24}$ [a]	6.8476	6.8712	6.8476
$Sr_6Pb_2Ti_8O_{24}$ [b]	6.8616	6.8616	6.8616
$Sr_6Pb_2Ti_8O_{24}$ [c]	6.9156	6.9156	6.8385
$Sr_5Pb_3Ti_8O_{24}$ [a]	7.1321	7.1321	7.0495
$Sr_5Pb_3Ti_8O_{24}$ [b]	7.1311	7.0823	7.1311
$Sr_5Pb_3Ti_8O_{24}$ [c]	7.1699	7.1699	7.1699
$Sr_4Pb_4Ti_8O_{24}$ [a]	7.4027	7.4027	7.2409
$Sr_4Pb_4Ti_8O_{24}$ [b]	7.4021	7.3025	7.4021
$Sr_4Pb_4Ti_8O_{24}$ [c]	7.4706	7.4706	7.4706
$Sr_4Pb_4Ti_8O_{24}$ [d]	7.3491	7.3841	7.3491
$Sr_4Pb_4Ti_8O_{24}$ [e]	7.3863	7.3956	7.3956
$Sr_4Pb_4Ti_8O_{24}$ [f]	7.3858	7.3858	7.3858
$Sr_3Pb_5Ti_8O_{24}$ [a]	7.6561	7.6561	7.5808
$Sr_3Pb_5Ti_8O_{24}$ [b]	7.6577	7.6046	7.6577
$Sr_3Pb_5Ti_8O_{24}$ [c]	7.6902	7.6902	7.6902
$Sr_2Pb_6Ti_8O_{24}$ [a]	7.9053	7.9148	7.9053
$Sr_2Pb_6Ti_8O_{24}$ [b]	7.9256	7.9256	7.9256
$Sr_2Pb_6Ti_8O_{24}$ [c]	7.9695	7.9695	7.8963
$Sr_1Pb_7Ti_8O_{24}$	8.2209	8.2209	8.2209
$Pb_8Ti_8O_{24}$	8.5323	8.5323	8.5323

Table A.13 The calculated dielectric constants of SPT

	ε_{11}	ε_{22}	ε_{33}
$Pb_8Ti_8O_{24}$	8.5323	8.5323	8.5323
$Pb_7Ba_1Ti_8O_{24}$	8.2602	8.2602	8.2602
$Pb_6Ba_2Ti_8O_{24}$ [a]	7.9824	7.9905	7.9824
$Pb_6Ba_2Ti_8O_{24}$ [b]	8.0340	8.0340	8.0340
$Pb_6Ba_2Ti_8O_{24}$ [c]	8.0545	8.0545	8.0237
$Pb_5Ba_3Ti_8O_{24}$ [a]	7.7708	7.7708	7.7418
$Pb_5Ba_3Ti_8O_{24}$ [b]	7.8049	7.7936	7.8049
$Pb_5Ba_3Ti_8O_{24}$ [c]	7.8651	7.8651	7.8651
$Pb_4Ba_4Ti_8O_{24}$ [a]	7.5549	7.5549	7.5035
$Pb_4Ba_4Ti_8O_{24}$ [b]	7.6195	7.5872	7.6195
$Pb_4Ba_4Ti_8O_{24}$ [c]	7.7251	7.7251	7.7251
$Pb_4Ba_4Ti_8O_{24}$ [d]	7.5604	7.5771	7.5604
$Pb_4Ba_4Ti_8O_{24}$ [e]	7.5938	7.6145	7.6145
$Pb_4Ba_4Ti_8O_{24}$ [f]	7.5750	7.5750	7.5750
$Pb_3Ba_5Ti_8O_{24}$ [a]	7.3789	7.3789	7.3488
$Pb_3Ba_5Ti_8O_{24}$ [b]	7.3986	7.3908	7.3986
$Pb_3Ba_5Ti_8O_{24}$ [c]	7.4398	7.4398	7.4398
$Pb_2Ba_6Ti_8O_{24}$ [a]	7.1862	7.1901	7.1862
$Pb_2Ba_6Ti_8O_{24}$ [b]	7.2272	7.2272	7.2272
$Pb_2Ba_6Ti_8O_{24}$ [c]	7.2274	7.2274	7.2103
$Pb_1Ba_7Ti_8O_{24}$	7.0335	7.0335	7.0335
$Ba_8Ti_8O_{24}$	6.8605	6.8605	6.8605

Table A.14 The calculated dielectric constants of SBT

	ε_{11}	ε_{22}	ε_{33}
$Sr_8Ti_8O_{24}$	6.3989	6.3989	6.3989
$Sr_7Ba_1Ti_8O_{24}$	6.4678	6.4678	6.4678
$Sr_6Ba_2Ti_8O_{24}$ [a]	6.5256	6.5247	6.5256
$Sr_6Ba_2Ti_8O_{24}$ [b]	6.5323	6.5323	6.5323
$Sr_6Ba_2Ti_8O_{24}$ [c]	6.5236	6.5236	6.5321
$Sr_5Ba_3Ti_8O_{24}$ [a]	6.5775	6.5775	6.5904
$Sr_5Ba_3Ti_8O_{24}$ [b]	6.5842	6.5913	6.5842
$Sr_5Ba_3Ti_8O_{24}$ [c]	6.5807	6.5807	6.5807
$Sr_4Ba_4Ti_8O_{24}$ [a]	6.6293	6.6293	6.6507
$Sr_4Ba_4Ti_8O_{24}$ [b]	6.6392	6.6417	6.6392
$Sr_4Ba_4Ti_8O_{24}$ [c]	6.6272	6.6272	6.6272
$Sr_4Ba_4Ti_8O_{24}$ [d]	6.6456	6.6358	6.6456
$Sr_4Ba_4Ti_8O_{24}$ [e]	6.6434	6.6426	6.6426
$Sr_4Ba_4Ti_8O_{24}$ [f]	6.6397	6.6397	6.6397
$Sr_3Ba_5Ti_8O_{24}$ [a]	6.6938	6.6938	6.7018
$Sr_3Ba_5Ti_8O_{24}$ [b]	6.6961	6.7009	6.6961
$Sr_3Ba_5Ti_8O_{24}$ [c]	6.6955	6.6955	6.6955
$Sr_2Ba_6Ti_8O_{24}$ [a]	6.7527	6.7504	6.7527
$Sr_2Ba_6Ti_8O_{24}$ [b]	6.7568	6.7568	6.7568
$Sr_2Ba_6Ti_8O_{24}$ [c]	6.7516	6.7516	6.7549
$Sr_1Ba_7Ti_8O_{24}$	6.8104	6.8104	6.8104
$Ba_8Ti_8O_{24}$	6.8605	6.8605	6.8605

Table A.15 The calculated dielectric constants of BZT

	ε_{11}	ε_{22}	ε_{33}
$Ba_8Zr_8O_{24}$	4.9333	4.9333	4.9333
$Ba_8Zr_7Ti_1O_{24}$	5.1184	5.1184	5.1184
$Ba_8Zr_6Ti_2O_{24}$ [a]	5.2977	5.3454	5.2977
$Ba_8Zr_6Ti_2O_{24}$ [b]	5.3216	5.3216	5.3216
$Ba_8Zr_6Ti_2O_{24}$ [c]	5.3098	5.3098	5.3096
$Ba_8Zr_5Ti_3O_{24}$ [a]	5.5346	5.5346	5.4825
$Ba_8Zr_5Ti_3O_{24}$ [b]	5.5123	5.5584	5.5123
$Ba_8Zr_5Ti_3O_{24}$ [c]	5.5133	5.5133	5.5133
$Ba_8Zr_4Ti_4O_{24}$ [a]	5.7768	5.7768	5.6637
$Ba_8Zr_4Ti_4O_{24}$ [b]	5.7309	5.8261	5.7309
$Ba_8Zr_4Ti_4O_{24}$ [c]	5.7262	5.7262	5.7262
$Ba_8Zr_4Ti_4O_{24}$ [d]	5.7399	5.7500	5.7399
$Ba_8Zr_4Ti_4O_{24}$ [e]	5.7140	5.7651	5.7651
$Ba_8Zr_4Ti_4O_{24}$ [f]	5.7326	5.7326	5.7326
$Ba_8Zr_3Ti_5O_{24}$ [a]	6.0026	6.0026	5.9371
$Ba_8Zr_3Ti_5O_{24}$ [b]	5.9811	6.0237	5.9811
$Ba_8Zr_3Ti_5O_{24}$ [c]	5.9768	5.9768	5.9768
$Ba_8Zr_2Ti_6O_{24}$ [a]	6.2320	6.2902	6.2320
$Ba_8Zr_2Ti_6O_{24}$ [b]	6.2711	6.2711	6.2711
$Ba_8Zr_2Ti_6O_{24}$ [c]	6.2503	6.2503	6.2317
$Ba_8Zr_1Ti_7O_{24}$	6.5411	6.5411	6.5411
$Ba_8Ti_8O_{24}$	6.8605	6.8605	6.8605

Table A.16 The calculated dielectric constants of SZT

	ε_{11}	ε_{22}	ε_{33}
$Sr_8Zr_8O_{24}$	4.6485	4.6485	4.6485
$Sr_8Zr_7Ti_1O_{24}$	4.8211	4.8211	4.8211
$Sr_8Zr_6Ti_2O_{24}$[a]	4.9930	5.0194	4.9930
$Sr_8Zr_6Ti_2O_{24}$[b]	5.0085	5.0085	5.0085
$Sr_8Zr_6Ti_2O_{24}$[c]	4.9967	4.9967	5.0044
$Sr_8Zr_5Ti_3O_{24}$[a]	5.1968	5.1968	5.1743
$Sr_8Zr_5Ti_3O_{24}$[b]	5.1878	5.2203	5.1878
$Sr_8Zr_5Ti_3O_{24}$[c]	5.1879	5.1879	5.1879
$Sr_8Zr_4Ti_4O_{24}$[a]	5.4105	5.4105	5.3546
$Sr_8Zr_4Ti_4O_{24}$[b]	5.3924	5.4559	5.3924
$Sr_8Zr_4Ti_4O_{24}$[c]	5.3842	5.3842	5.3842
$Sr_8Zr_4Ti_4O_{24}$[d]	5.3971	5.3986	5.3971
$Sr_8Zr_4Ti_4O_{24}$[e]	5.3828	5.4108	5.4108
$Sr_8Zr_4Ti_4O_{24}$[f]	5.3882	5.3882	5.3882
$Sr_8Zr_3Ti_5O_{24}$[a]	5.6255	5.6255	5.5918
$Sr_8Zr_3Ti_5O_{24}$[b]	5.6192	5.6458	5.6192
$Sr_8Zr_3Ti_5O_{24}$[c]	5.6116	5.6116	5.6116
$Sr_8Zr_2Ti_6O_{24}$[a]	5.8494	5.8805	5.8494
$Sr_8Zr_2Ti_6O_{24}$[b]	5.8778	5.8778	5.8778
$Sr_8Zr_2Ti_6O_{24}$[c]	5.8585	5.8585	5.8484
$Sr_8Zr_1Ti_7O_{24}$	6.1235	6.1235	6.1235
$Sr_8Ti_8O_{24}$	6.3989	6.3989	6.3989

Table A.17 The calculated dielectric constants of PZT

	ε_{11}	ε_{22}	ε_{33}
$Pb_8Zr_8O_{24}$	6.8675	6.8675	6.8675
$Pb_8Zr_7Ti_1O_{24}$	7.0351	7.0351	7.0351
$Pb_8Zr_6Ti_2O_{24}$[a]	7.1919	7.1677	7.1919
$Pb_8Zr_6Ti_2O_{24}$[b]	7.2216	7.2216	7.2216
$Pb_8Zr_6Ti_2O_{24}$[c]	7.1843	7.1843	7.2087
$Pb_8Zr_5Ti_3O_{24}$[a]	7.3247	7.3247	7.3669
$Pb_8Zr_5Ti_3O_{24}$[b]	7.3846	7.3793	7.3846
$Pb_8Zr_5Ti_3O_{24}$[c]	7.3675	7.3675	7.3675
$Pb_8Zr_4Ti_4O_{24}$[a]	7.4735	7.4735	7.5470
$Pb_8Zr_4Ti_4O_{24}$[b]	7.6038	7.5843	7.6038
$Pb_8Zr_4Ti_4O_{24}$[c]	7.5570	7.5570	7.5570
$Pb_8Zr_4Ti_4O_{24}$[d]	7.5402	7.5294	7.5402
$Pb_8Zr_4Ti_4O_{24}$[e]	7.5801	7.5538	7.5538
$Pb_8Zr_4Ti_4O_{24}$[f]	7.5094	7.5094	7.5094
$Pb_8Zr_3Ti_5O_{24}$[a]	7.7069	7.7069	7.4130
$Pb_8Zr_3Ti_5O_{24}$[b]	7.7816	7.7618	7.7816
$Pb_8Zr_3Ti_5O_{24}$[c]	7.7661	7.7661	7.7661
$Pb_8Zr_2Ti_6O_{24}$[a]	7.9692	7.9356	7.9692
$Pb_8Zr_2Ti_6O_{24}$[b]	8.0281	8.0281	8.0281
$Pb_8Zr_2Ti_6O_{24}$[c]	7.9737	7.9737	7.9744
$Pb_8Zr_1Ti_7O_{24}$	8.2324	8.2324	8.2324
$Pb_8Ti_8O_{24}$	8.5323	8.5323	8.5323

Table A.18 The calculated direct piezoelectric constants of PBT

	Direct piezoelectric constants (C/m^2)					
	Relaxed – ion			Clamped – ion		
	e_{31}	e_{33}	e_{15}	e_{31}	e_{33}	e_{15}
$BaTiO_3$	0.255	3.603	0.078	0.415	-0.118	0.200
$Pb_{0.125}Ba_{0.875}TiO_3$	0.453	3.684	0.146	0.427	-0.192	0.214
$Pb_{0.25}Ba_{0.75}TiO_3$ [a]	0.639	3.819	10.398	0.427	-0.259	0.226
$Pb_{0.25}Ba_{0.75}TiO_3$ [b]	0.723	3.833	14.670	0.434	-0.269	0.224
$Pb_{0.25}Ba_{0.75}TiO_3$ [c]	0.635	3.989	8.021	0.428	-0.256	0.222
$Pb_{0.25}Ba_{0.75}TiO_3$ [d]	0.691	3.742	9.582	0.438	-0.284	0.228
$Pb_{0.25}Ba_{0.75}TiO_3$ [e]	0.638	3.659	8.351	0.440	-0.281	0.231
$Pb_{0.375}Ba_{0.625}TiO_3$ [a]	0.732	3.525	4.379	0.461	-0.384	0.243
$Pb_{0.375}Ba_{0.625}TiO_3$ [b]	0.670	3.517	4.915	0.446	-0.385	0.253
$Pb_{0.375}Ba_{0.625}TiO_3$ [c]	0.673	3.523	5.051	0.446	-0.385	0.253
$Pb_{0.375}Ba_{0.625}TiO_3$ [d]	0.738	3.557	4.007	0.445	-0.387	0.252
$Pb_{0.375}Ba_{0.625}TiO_3$ [e]	0.748	3.578	4.361	0.462	-0.384	0.244
$Pb_{0.5}Ba_{0.5}TiO_3$ [a]	0.844	3.566	3.839	0.455	-0.487	0.264
$Pb_{0.5}Ba_{0.5}TiO_3$ [b]	0.841	3.557	3.661	0.454	-0.488	0.269
$Pb_{0.5}Ba_{0.5}TiO_3$ [c]	0.767	3.351	3.672	0.457	-0.528	0.279
$Pb_{0.5}Ba_{0.5}TiO_3$ [d]	0.839	3.427	2.943	0.457	-0.513	0.266
$Pb_{0.5}Ba_{0.5}TiO_3$ [e]	0.853	3.436	3.175	0.474	-0.513	0.264
$Pb_{0.625}Ba_{0.375}TiO_3$ [a]	1.008	3.456	2.741	0.489	-0.589	0.252
$Pb_{0.625}Ba_{0.375}TiO_3$ [b]	0.882	3.315	2.998	0.472	-0.605	0.269
$Pb_{0.625}Ba_{0.375}TiO_3$ [c]	0.879	3.308	2.990	0.472	-0.606	0.269
$Pb_{0.625}Ba_{0.375}TiO_3$ [d]	0.959	3.458	2.491	0.470	-0.589	0.265
$Pb_{0.625}Ba_{0.375}TiO_3$ [e]	0.996	3.445	2.754	0.489	-0.588	0.252
$Pb_{0.75}Ba_{0.25}TiO_3$ [a]	0.967	3.359	2.518	0.483	-0.660	0.261
$Pb_{0.75}Ba_{0.25}TiO_3$ [b]	1.0227	3.358	2.675	0.492	-0.681	0.255
$Pb_{0.75}Ba_{0.25}TiO_3$ [c]	0.867	3.240	2.845	0.486	-0.678	0.261
$Pb_{0.75}Ba_{0.25}TiO_3$ [d]	1.008	3.352	2.426	0.489	-0.683	0.253
$Pb_{0.75}Ba_{0.25}TiO_3$ [e]	1.032	3.392	2.627	0.495	-0.673	0.250
$Pb_{0.875}Ba_{0.125}TiO_3$	1.027	3.278	2.576	0.508	-0.747	0.240
$PbTiO_3$	1.084	3.283	2.600	0.533	-0.825	0.229

Table A.19 The calculated converse piezoelectric constants of PBT

	Converse piezoelectric constants (pC/N)					
	Relaxed – ion			Clamped – ion		
	d_{31}	d_{33}	d_{15}	d_{31}	d_{33}	d_{15}
$BaTiO_3$	-12.285	61.834	0.747	1.496	-1.526	1.949
$Pb_{0.125}Ba_{0.875}TiO_3$	-16.963	94.536	-0.985	1.678	-2.237	2.793
$Pb_{0.25}Ba_{0.75}TiO_3$ [a]	-24.417	137.022	146.336	1.785	-2.416	2.501
$Pb_{0.25}Ba_{0.75}TiO_3$ [b]	-24.698	142.780	510.416	1.842	-2.484	2.505
$Pb_{0.25}Ba_{0.75}TiO_3$ [c]	-24.703	138.744	124.516	1.804	-2.438	2.438
$Pb_{0.25}Ba_{0.75}TiO_3$ [d]	-25.158	145.435	238.318	1.863	-2.574	2.530
$Pb_{0.25}Ba_{0.75}TiO_3$ [e]	-24.371	139.256	176.784	1.876	-2.547	2.630
$Pb_{0.375}Ba_{0.625}TiO_3$ [a]	-31.025	185.546	82.015	2.179	-3.205	3.015
$Pb_{0.375}Ba_{0.625}TiO_3$ [b]	-46.391	265.858	106.840	2.113	-3.249	3.140
$Pb_{0.375}Ba_{0.625}TiO_3$ [c]	-43.782	249.505	109.198	2.111	-3.246	3.135
$Pb_{0.375}Ba_{0.625}TiO_3$ [d]	-34.373	195.011	73.770	2.064	-3.229	3.114
$Pb_{0.375}Ba_{0.625}TiO_3$ [e]	-32.115	192.174	81.268	2.178	-3.204	3.017
$Pb_{0.5}Ba_{0.5}TiO_3$ [a]	-42.594	251.106	83.051	2.371	-3.934	3.537
$Pb_{0.5}Ba_{0.5}TiO_3$ [b]	-47.902	275.498	79.626	2.366	-3.944	3.628
$Pb_{0.5}Ba_{0.5}TiO_3$ [c]	-43.751	246.675	98.946	2.465	-4.179	3.921
$Pb_{0.5}Ba_{0.5}TiO_3$ [d]	-43.191	242.023	63.463	2.384	-4.085	3.660
$Pb_{0.5}Ba_{0.5}TiO_3$ [e]	-40.891	254.105	71.535	2.504	-4.082	3.605
$Pb_{0.625}Ba_{0.375}TiO_3$ [a]	-25.803	185.044	63.081	2.724	-4.541	3.688
$Pb_{0.625}Ba_{0.375}TiO_3$ [b]	-27.285	162.423	77.509	2.681	-4.656	3.956
$Pb_{0.625}Ba_{0.375}TiO_3$ [c]	-27.833	267.569	77.935	2.684	-4.664	3.973
$Pb_{0.625}Ba_{0.375}TiO_3$ [d]	-33.321	191.011	54.856	2.577	-4.543	3.844
$Pb_{0.625}Ba_{0.375}TiO_3$ [e]	-24.692	177.573	62.958	2.716	-4.529	3.674
$Pb_{0.75}Ba_{0.25}TiO_3$ [a]	-26.858	161.089	62.218	2.831	-5.037	3.986
$Pb_{0.75}Ba_{0.25}TiO_3$ [b]	-19.713	127.758	71.698	2.915	-5.127	3.925
$Pb_{0.75}Ba_{0.25}TiO_3$ [c]	-22.443	131.971	79.071	2.912	-5.146	4.016
$Pb_{0.75}Ba_{0.25}TiO_3$ [d]	-20.591	127.403	62.376	2.871	-5.123	3.895
$Pb_{0.75}Ba_{0.25}TiO_3$ [e]	-19.247	123.066	68.576	2.888	-5.035	3.811
$Pb_{0.875}Ba_{0.125}TiO_3$	-15.746	103.056	71.667	3.118	-5.526	3.825
$PbTiO_3$	-13.320	92.419	100.956	3.363	-6.001	3.789

Table A.20 The calculated direct piezoelectric constants of SBT

	Direct piezoelectric constants (C/m^2)					
	Relaxed – ion			Clamped – ion		
	e_{31}	e_{33}	e_{15}	e_{31}	e_{33}	e_{15}
$BaTiO_3$	0.255	3.603	0.078	0.415	-0.118	0.200
$Sr_{0.125}Ba_{0.875}TiO_3$	0.303	3.900	0.063	0.409	-0.119	0.203
$Sr_{0.25}Ba_{0.75}TiO_3$	0.352	4.307	0.040	0.403	-0.119	0.203
$Sr_{0.375}Ba_{0.625}TiO_3$	0.424	4.807	-0.019	0.382	-0.106	0.179
$Sr_{0.5}Ba_{0.5}TiO_3$	0.503	5.466	-0.051	0.354	-0.095	0.157
$Sr_{0.625}Ba_{0.375}TiO_3$	0.473	5.808	-0.064	0.343	-0.098	0.159
$Sr_{0.75}Ba_{0.25}TiO_3$	0.466	6.323	-0.081	0.329	-0.103	0.157
$Sr_{0.875}Ba_{0.125}TiO_3$	0.405	6.919	-0.155	0.312	-0.104	0.152
$SrTiO_3$	0.465	7.722	-0.096	0.287	-0.110	0.141

Table A.21 The calculated converse piezoelectric constants of SBT

	Converse piezoelectric constants (pC/N)					
	Relaxed – ion			Clamped – ion		
	d_{31}	d_{33}	d_{15}	d_{31}	d_{33}	d_{15}
$BaTiO_3$	-12.285	61.834	0.747	1.496	-1.526	1.949
$Sr_{0.125}Ba_{0.875}TiO_3$	-14.599	76.538	0.647	1.491	-1.526	2.007
$Sr_{0.25}Ba_{0.75}TiO_3$	-18.662	98.006	0.408	1.445	-1.487	1.985
$Sr_{0.375}Ba_{0.625}TiO_3$	-14.239	76.499	-0.197	1.333	-1.323	1.731
$Sr_{0.5}Ba_{0.5}TiO_3$	-12.274	67.771	-0.501	1.205	-1.163	1.501
$Sr_{0.625}Ba_{0.375}TiO_3$	-12.683	68.321	-0.823	1.156	-1.121	1.522
$Sr_{0.75}Ba_{0.25}TiO_3$	-12.668	67.186	-0.081	1.098	-1.079	1.498
$Sr_{0.875}Ba_{0.125}TiO_3$	-12.948	66.607	-2.085	1.023	-1.012	1.458
$SrTiO_3$	-12.403	63.442	4.251	0.937	-0.947	1.429

Table A.22 The calculated direct piezoelectric constants of SPT

	Direct piezoelectric constants (C/m^2)					
	Relaxed – ion			Clamped – ion		
	e_{31}	e_{33}	e_{15}	e_{31}	e_{33}	e_{15}
$PbTiO_3$	1.084	3.283	2.600	0.533	-0.825	0.229
$Sr_{0.125}Pb_{0.875}TiO_3$	1.004	3.245	2.467	0.547	-0.682	0.257
$Sr_{0.25}Pb_{0.75}TiO_3$	0.884	3.165	2.182	0.513	-0.061	0.275
$Sr_{0.375}Pb_{0.625}TiO_3$	0.906	3.442	2.579	0.508	-0.547	0.315
$Sr_{0.5}Pb_{0.5}TiO_3$	1.115	5.191	6.581	0.453	-0.321	0.221
$Sr_{0.625}Pb_{0.375}TiO_3$	1.006	5.875	11.365	0.408	-0.237	0.189
$Sr_{0.75}Pb_{0.25}TiO_3$	1.005	6.294	14.784	0.377	-0.193	0.176
$Sr_{0.875}Pb_{0.125}TiO_3$	0.773	6.828	0.018	0.326	-0.119	0.152
$SrTiO_3$	0.465	7.722	-0.096	0.287	-0.110	0.141

Table A.23 The calculated converse piezoelectric constants of SPT

	Converse piezoelectric constants (pC/N)					
	Relaxed – ion			Clamped – ion		
	d_{31}	d_{33}	d_{15}	d_{31}	d_{33}	d_{15}
$PbTiO_3$	-13.320	92.419	100.956	3.363	-6.001	3.789
$Sr_{0.125}Pb_{0.875}TiO_3$	-16.312	106.895	68.233	3.112	-5.260	3.956
$Sr_{0.25}Pb_{0.75}TiO_3$	-19.817	121.841	54.557	2.830	-4.734	4.115
$Sr_{0.375}Pb_{0.625}TiO_3$	-44.401	261.375	64.102	2.719	-4.467	4.493
$Sr_{0.5}Pb_{0.5}TiO_3$	-47.183	264.112	165.759	1.912	-2.706	2.509
$Sr_{0.625}Pb_{0.375}TiO_3$	-23.229	138.957	242.533	1.567	-2.014	2.018
$Sr_{0.75}Pb_{0.25}TiO_3$	-14.669	90.216	325.543	1.361	-1.620	1.812
$Sr_{0.875}Pb_{0.125}TiO_3$	-12.147	71.257	-0.250	1.085	-1.119	1.676
$SrTiO_3$	-12.403	63.442	4.251	0.937	-0.947	1.429

Table A.24 The calculated direct piezoelectric constants of PZT

	Direct piezoelectric constants (C/m^2)					
	Relaxed – ion			Clamped – ion		
	e_{31}	e_{33}	e_{15}	e_{31}	e_{33}	e_{15}
$PbTiO_3$	1.084	3.283	2.600	0.533	-0.825	0.229
$PbZr_{0.125}Ti_{0.875}O_3$	1.014	3.293	2.769	0.536	-0.742	0.209
$PbZr_{0.25}Ti_{0.75}O_3$	0.753	3.222	3.082	0.482	-0.701	0.177
$PbZr_{0.375}Ti_{0.625}O_3$	0.739	3.452	3.837	0.426	-0.658	0.134
$PbZr_{0.5}Ti_{0.5}O_3$	0.661	3.631	4.799	0.361	-0.597	0.081
$PbZr_{0.625}Ti_{0.375}O_3$	0.545	3.675	7.945	0.301	-0.559	0.044
$PbZr_{0.75}Ti_{0.25}O_3$	0.269	3.637	51.175	0.235	-0.515	0.009
$PbZr_{0.875}Ti_{0.125}O_3$	0.271	3.723	3.857	0.186	-0.509	-0.295
$PbZrO_3$	0.235	3.722	-0.091	0.136	-0.499	-0.046

Table A.25 The calculated converse piezoelectric constants of PZT

	Converse piezoelectric constants (pC/N)					
	Relaxed – ion			Clamped – ion		
	d_{31}	d_{33}	d_{15}	d_{31}	d_{33}	d_{15}
$PbTiO_3$	-13.320	92.419	100.956	3.363	-6.001	3.789
$PbZr_{0.125}Ti_{0.875}O_3$	-20.099	118.200	104.834	3.264	-5.612	3.358
$PbZr_{0.25}Ti_{0.75}O_3$	-42.077	198.955	151.767	2.943	-5.237	2.845
$PbZr_{0.375}Ti_{0.625}O_3$	-45.503	207.130	188.166	2.629	-4.812	2.105
$PbZr_{0.5}Ti_{0.5}O_3$	-33.362	146.311	550.942	2.192	-4.146	1.231
$PbZr_{0.625}Ti_{0.375}O_3$	-30.267	123.657	-5289.445	1.875	-3.683	0.675
$PbZr_{0.75}Ti_{0.25}O_3$	-23.633	88.757	-746.083	1.437	-3.116	0.138
$PbZr_{0.875}Ti_{0.125}O_3$	-18.491	68.719	84.274	1.285	-2.889	1.623
$PbZrO_3$	-13.778	50.455	-1.591	1.061	-2.625	-0.727

Table A.26 The calculated direct piezoelectric constants of BZT

	Direct piezoelectric constants (C/m^2)					
	Relaxed – ion			Clamped – ion		
	e_{31}	e_{33}	e_{15}	e_{31}	e_{33}	e_{15}
$BaTiO_3$	0.255	3.603	0.078	0.415	-0.118	0.200
$BaZr_{0.125}Ti_{0.875}O_3$	0.195	4.328	0.138	0.336	-0.104	0.159
$BaZr_{0.25}Ti_{0.75}O_3$	0.191	5.203	0.298	0.255	-0.085	0.121
$BaZr_{0.375}Ti_{0.625}O_3$	0.069	3.847	0.754	0.242	-0.092	0.125
$BaZr_{0.5}Ti_{0.5}O_3$	-0.049	2.559	1.417	0.214	-0.082	0.117
$BaZr_{0.625}Ti_{0.375}O_3$	-0.218	3.385	4.071	0.153	-0.083	0.095
$BaZr_{0.75}Ti_{0.25}O_3$	-0.089	4.634	0.102	0.094	-0.094	0.067
$BaZr_{0.875}Ti_{0.125}O_3$	-0.029	3.047	0.129	0.045	-0.045	0.035
$BaZrO_3$	-0.006	0.153	0.024	-0.009	0.017	-0.005

Table A.27 The calculated converse piezoelectric constants of BZT

	Converse piezoelectric constants (pC/N)					
	Relaxed – ion			Clamped – ion		
	d_{31}	d_{33}	d_{15}	d_{31}	d_{33}	d_{15}
$BaTiO_3$	-12.285	61.834	0.747	1.496	-1.526	1.949
$BaZr_{0.125}Ti_{0.875}O_3$	-12.461	60.524	1.408	1.223	-1.237	1.581
$BaZr_{0.25}Ti_{0.75}O_3$	-10.921	50.886	3.063	0.914	-0.921	1.209
$BaZr_{0.375}Ti_{0.625}O_3$	-6.805	32.456	8.406	0.871	-0.901	1.336
$BaZr_{0.5}Ti_{0.5}O_3$	-3.743	17.106	17.036	0.761	-0.776	1.314
$BaZr_{0.625}Ti_{0.375}O_3$	-5.552	22.441	51.223	0.560	-0.633	1.084
$BaZr_{0.75}Ti_{0.25}O_3$	-6.445	28.185	1.185	0.376	-0.542	0.778
$BaZr_{0.875}Ti_{0.125}O_3$	-3.101	14.261	1.555	0.177	-0.253	0.423
$BaZrO_3$	-0.139	0.602	0.296	-0.041	0.079	-0.062

Table A.28 The calculated direct piezoelectric constants of SZT

	Direct piezoelectric constants (C/m^2)					
	Relaxed – ion			Clamped – ion		
	e_{31}	e_{33}	e_{15}	e_{31}	e_{33}	e_{15}
$SrTiO_3$	0.465	7.722	-0.096	0.287	-0.110	0.141
$SrZr_{0.125}Ti_{0.875}O_3$	0.039	6.368	1.142	0.273	-0.112	0.161
$SrZr_{0.25}Ti_{0.75}O_3$	0.082	6.292	0.333	0.231	-0.116	0.164
$SrZr_{0.375}Ti_{0.625}O_3$	0.028	5.289	1.122	0.239	-0.129	0.206
$SrZr_{0.5}Ti_{0.5}O_3$	0.179	4.826	2.526	0.222	-0.140	0.229
$SrZr_{0.625}Ti_{0.375}O_3$	0.104	4.896	3.279	0.187	-0.167	0.231
$SrZr_{0.75}Ti_{0.25}O_3$	0.056	5.114	4.857	0.118	-0.138	0.196
$SrZr_{0.875}Ti_{0.125}O_3$	-0.256	4.743	5.402	0.088	-0.151	0.115
$SrZrO_3$	-0.293	4.872	4.143	0.041	-0.133	0.174

Table A.29 The calculated converse piezoelectric constants of SZT

	Converse piezoelectric constants (pC/N)					
	Relaxed – ion			Clamped – ion		
	d_{31}	d_{33}	d_{15}	d_{31}	d_{33}	d_{15}
$SrTiO_3$	-12.403	63.442	4.251	0.937	-0.947	1.429
$SrZr_{0.125}Ti_{0.875}O_3$	-11.956	55.705	12.457	0.904	-0.924	1.654
$SrZr_{0.25}Ti_{0.75}O_3$	-10.774	49.846	3.816	0.776	-0.831	1.775
$SrZr_{0.375}Ti_{0.625}O_3$	-11.665	55.384	15.227	0.837	-0.955	2.413
$SrZr_{0.5}Ti_{0.5}O_3$	-9.777	50.129	46.932	0.811	-0.995	2.826
$SrZr_{0.625}Ti_{0.375}O_3$	-11.805	52.692	63.965	0.739	-1.042	2.911
$SrZr_{0.75}Ti_{0.25}O_3$	-12.973	55.421	136.118	0.493	-0.777	2.518
$SrZr_{0.875}Ti_{0.125}O_3$	-12.246	45.505	168.627	0.407	-0.766	1.536
$SrZrO_3$	-11.307	41.153	142.208	0.239	-0.599	2.389

CURRICULUM VITAE

PERSONAL INFORMATION

Name Surname : Berna AKGENÇ

Date of birth and place : 29.03.1987 Bakırköy

Foreign Languages : English

E-mail : berna_akgenc@hotmail.com

EDUCATION

Degree	Department	University	Date of Graduation
Master	Physics	Sakarya University	2010
Undergraduate	Physics	Kocaeli University	2008
High School	Fen	Bahçelievler Lisesi	2004

WORK EXPERIENCE

Year	Corporation/Institute	Enrollment
2010 - …	Kırklareli University	Research Assistant
2012 - 2014	Texas A&M University	Visiting Scholar
2009 - 2010	Augsburg Universitat	Visiting Scholar

PUBLISHMENTS

Conference Papers

1. Akgenc, B., Tasseven, C., and Cagin, T., (2016). "Piezoelectricity as smart materials", 2nd International Conference on Organic Electronic Material Technologies (OEMT), 5 - 8 September 2016, Bodrum, Mugla, TURKEY.

2. Akgenc, B., Tasseven, C., and Cagin, T., (2015). "Stability and mechanical properties of $\{A_xA_{(1-x)}'\ B_yB_{(1-y)}'\}O_3$ Ceramics", TMS Middle East – Mediterranean Materials Congress on Energy and Infrastructure Systems, 11-14 January 2015, Doha,Qatar.

3. Akgenc, B., Tasseven, C., and Cagin, T., (2015). "First principles investigations of structural, elastic, dielectric and piezoelectric properties of {Ba,Sr,Pb}TiO3 , {Ba,Sr,Pb}ZrO3 and {Ba,Sr,Pb}{Ti,Zr}O3 ceramics", APS Bulletin of American Physical Society, APS March Meeting, 2-6 March 2015, San Antonio, Texas, USA.

4. Akgenc, B., Tasseven, C., and Cagin, T., (2015). "Electro-Thermo-Mechanical and defect kinetics in AXA(1-x)ByB(1-y)O3AXA(1-x)ByB(1-y)O3", Canadian-American-Mexican (CAM) Graduate Student Physics Conference, 2-9 September 2015, Oaxaca, Mexico.

5. Akgenc, B., Tasseven, C., and Cagin, T., (2015). "Lattice, elastic and piezoelectric properties in tetragonal BaTiO3/PbTiO3 first principle calcuation", 2nd Texas A&M Energy Institute Research Workshop, 20 October 2015, College Station, Texas, USA.

6. Akgenc, B., Tasseven, C., and Cagin, T.,(2014). "DFT-based ab-initio studies of lattice, elastic and piezoelectric properties of Barium Titanate Polymorphs", International Institute for Multifunctional Materilas for Energy Conversion (IIMEC) Annual Meeting, Texas A&M University, 13-14 June 2014, College Station, Texas, USA.